ISOTOPE SEPARATION IN A ROTATING PLASMA

J. B. S. CAIRNS

This thesis is submitted in partial fulfilment of the requirements for the degree of Doctor of Philosophy in the University of Loughborough

December 1976

This thesis is dedicated to my
mother and father

I declare that no part of this Thesis has previously been submitted for a degree in this or any other University.

J.B.S. Cairns

Department of Physics,
Loughborough University
Leicestershire
ENGLAND

C O N T E N T S

CONTENTS
(continued)

CONTENTS
(continued)

Page

CHAPTER VII

CONCLUSIONS

APPENDICES

ACKNOWLEDGEMENTS

The investigation reported in this Thesis has been carried out at the UKAEA Culham Laboratory, Abingdon, Oxfordshire. This research has benefited from many people who have found the time to help me. Their guidance is warmly appreciated.

I wish to thank my University supervisor, Dr J. Sturgess for his help and encouragement, and also my external supervisor, Dr J.W.M. Paul for his invaluable guidance throughout all phases of the experimental work.

I wish to thank Dr F. Haas for his guidance with plasma theory. I also thank Mr L.S. Holmes, Mr P.R. Heldley, Dr P.T. Rumsby and Mr R. Scott for their assistance with the laboratory experiments.

Finally, special thanks to Ina for her kindness, patience and excellent typing.

ABSTRACT

Isotope separation is an important field of scientific research. Many methods have been used to separate elements and isotopes. The two main processes used at present are diffusion and centrifuging. In the second category, rotating plasmas may be of importance due to the high rotational velocities which can be obtained.

This thesis describes an experimental study of isotopic enrichment in a rotating neon plasma. Some of the theoretical considerations are also presented and a new theory of isotopic separation in rotating plasmas is formulated.

VORTEX II, the rotating plasma device used in the research to study neon enrichment, was redesigned from an earlier experiment built at Culham Laboratory. Essentially the machine consisted of two coaxial electrodes which formed an annular vacuum vessel. The interelectrode space was filled with neon at a pressure of 50 mtorr and a radial current pulse of 8 KA peak and 3.5 ms duration was passed through the gas in an axial magnetic field of typically $B_z \approx 0.1\,T$. This produced a net azimuthal motion in the plasma.

Electric probes, laser interferometry and a mechanical sampling valve were used to measure the spatial and time dependence of the plasma dynamics and the isotopic enrichment. Typical parameters found in the VORTEX II plasma were; electron density, $n_e = 10^{21}\,m^{-3}$, plasma flow velocity, $v_\theta = 10^4\,m\,s^{-1}$, electron temperature, $T_e \doteq 4\,eV$, stable flow time, $\tau_f = 3 \times 10^{-3}\,s$.

The spatial and temporal behaviour of the isotopic enrichment was determined using a fast acting, electromagnetically driven gas valve with a typical operating time of 400 μs connected to a mass spectrometer. Results obtained showed that enrichment of the heavy isotope, ^{22}Ne, increased with increasing radius, r, and flow velocity to a maximum value of 20% at the outer electrode wall. Two dimensional separation also occurred with ^{22}Ne depletion occurring at the inside plasma boundary, off the axis of the vertical mid plane.

Theory predicts only 4% enrichment and does not include two dimensional separation effects. Some mechanisms, similar to the counter-current flow in conventional centrifuges, are discussed which may explain the two-dimensional separation and the high enrichments obtained in VORTEX II.

CHAPTER I

ISOTOPE SEPARATION AND ROTATING PLASMAS

With the advent of nuclear power and the global depletion of fossil fuels, the enrichment of uranium in an efficient manner is essential to the present and future world economy. Consequently, the separation of isotopes is a very important field of scientific research and many methods of enrichment have, and are still being, investigated. These include aerodynamic nozzle processes, chemical exchange, laser separation, gas centrifuges, diffusion and electromagnetic methods, as well as the plasma centrifuge, the subject of this work.

1.1 AVAILABLE METHODS

Of these methods, the most important technique of separating isotopes to date has been the diffusion process. (Chemical exchange, and nozzle processes have had only limited success and will not be dealt with here.) This is the only method at present, which enriches the uranium isotopes on a large commercial scale. Briefly the process operates by passing uranium hexafluoride (UF_6) gas through a series of membranes using large compressors. The lightest isotope, ^{235}U, has a higher diffusion rate than ^{238}U and is therefore separated, since the diffusion rate of a gas of mass, M, is proportional to $(M)^{-\frac{1}{2}}$. The main disadvantages with this method are that firstly, the separation per stage is low, therefore cascades must be used; and secondly, the process requires a large power consumption.

At present the most serious contender to the diffusion process is the gas centrifuge. This essentially consists of a rotating cylinder which drives gas inside azimuthally by viscous shear. The theory of the centrifuge is based on the well-known fact that, in the steady state, the pressure gradient in a rotating gas, balances the outward centrifugal force.

For two gases of molecular weight, M_1 and M_2, the ratio of the pressure of the two gases at the rotor wall $(r = r_1)$ and at the axis $(r = r_o)$ is given by,

$$\left(\frac{P_1}{P_2}\right)_{(r_1)} = \left(\frac{P_1}{P_2}\right)_{(r_o)} \exp\left[\frac{(M_1 - M_2)(wr_1)^2}{2\,KT}\right] = \left(\frac{P_1}{P_2}\right)_{(r_o)} \alpha_o \qquad \ldots (1.1)$$

where w is the angular velocity of the rotor, and α_o, defined by equation (1.1), is the separation factor of the simple process. Equation (1.1) shows that the separation factor of the simple centrifugal process depends on the absolute mass difference, whereas for the diffusion process, we noted that it is proportional to $(M_2/M_1)^{\frac{1}{2}}$. For this basic reason, the centrifuge method should be particularly useful for the enrichment of heavy isotopes, such as uranium. The dependence of the separation factor on temperature should also be noted here. From equation (1.1) it can be seen that the lower the temperature the more efficient the centrifuge process becomes.

The figure of merit of a centrifuge is the separative power, δU. From the theory of gas centrifuges (LONDON (1961)) it can be shown that the maximum separative power of a centrifuge with a small separation factor is given by,

$$(\delta U)_{max} = \rho D \left[\frac{(M_1 - M_2)\,(w\,r_1)^2}{2\,KT}\right]^2 \frac{\pi Z}{2} \text{ kgms/s} \qquad \ldots (1.2)$$

where Z is the rotor length, ρ is the mass density, and D is the diffusion coefficient of the gas. The maximum separative power is therefore proportional to the fourth power of the peripheral velocity, to the rotor length and to the inverse square of the temperature. Ideally then, the separative power and the separation factor can be made very large simply by increasing the rotor speed; however, in mechanical devices the rotational velocity is limited by the mechanical strain of the moving parts and also by fluid dynamic turbulence which produces mixing. These limitations on the maximum peripheral velocity also mean that the separation factor per stage is low, so that cascades must be used to obtain the required enrichment, as with the diffusion process.

The laser separation method is a new and potentially important method of isotope separation. The process operates by irradiating uranium or UF_6 vapour with a highly monochromatic, tunable, dye laser, and selectively exciting the atoms (or molecules) of ^{235}U. These can then be separated from the remainder by selective photoionization by another laser, and subsequent removal by an electric field, by laser deflection of atomic beams or by photochemical methods. Large separation factors have been achieved in the laboratory using these techniques (BASOV et al, (1974); BERNHARDT (1974); LIU (1974); NEBENZAHL (1975); SNAVELY (1974)). As yet, however, there has not been a demonstration of a process capable of achieving bulk isotopic enrichment. An interesting comparison between the potential energy costs of laser separation with those of gaseous centrifuge separation, has recently been made by TAIT (1975). He estimates that ~ 75 keV per atom is required to enrich uranium by a few per cent, with the laser separation method, whereas ~ 200 KeV is required using conventional centrifuges to obtain the same enrichment.

Electromagnetic methods such as the calutron where an ion beam is deflected in a magnetic field, have been used for many years to separate out small amounts of pure isotope. The advantage of this method is that an isotope free from any impurities can be obtained. However, large scale isotope enrichment with this method is impossible due to space charge effects which limit the amount of ion current in the device. Calculations by SMITH et al (1947) give the maximum amount of pure isotope, M, which can be collected by this method, to be

$$M = 3.19 \times 10^{-4}\,\eta\left(\frac{A_2 - A_1}{A_1}\right) VB \ \text{mgs/hr} \qquad \ldots (1.3)$$

where η is the abundance ratio of the collected isotope, V is the accelerating voltage, and B the magnetic field strength. It is evident from equation (1.3) that the space charge effect imposes a drastic limitation on the amount of material collected, even for very high voltages and fields. In the so-called 'radial magnetic separator' (SMITH et al, 1947) and the 'ionic centrifuge' (SLEPIAN, 1958), unsuccessful attempts were made to neutralise the ion stream and thereby to reduce the space charge effect. Both were abandoned in favour of the caulutron.

1.2 A BRIEF HISTORY OF THE PLASMA CENTRIFUGE

From equation (1.1) and (1.2) it was seen that the azimuthal flow velocity plays a crucial role in the overall efficiency of the mechanical centrifuge. If similar scaling laws apply to the plasma centrifuge it is appropriate to ask whether plasma centrifuging to much higher velocities by MHD processes in a stationary cylinder might not offer an attractive alternative to the mechanical centrifuge. Other potential advantages of using such systems are that firstly, MHD driven rotation requires no moving parts and therefore there is no rotor wear, and secondly, the higher separations expected with plasma centrifuges compared with mechanical systems, may enable the number of stages in a cascade process to be reduced substantially, as pointed out by GEORGE and KANE (1972). One major disadvantage of the method, however, is that much higher temperatures occur in rotating plasmas compared with mechanical devices. Even for low degrees of ionization the gas temperature is of the order of $\sim 10^4$ °K.

It has been known for some time that by applying a current, $\underline{J}$, across a magnetic field, $\underline{B}$, the resulting $\underline{J} \times \underline{B}$ force can be used to make plasmas rotate. In rotating plasmas, unlike the calutron, the problem of charge separation does not occur to any appreciable extent, and large ion currents are therefore possible. In 1966 BONNEVIER proposed a simple model of isotope and element separation in rotating plasma devices, and obtained some theoretical estimates which compared favourably with mechanical centrifuges. Since then the theory has been extended to cover a wide range of possible operating conditions (LEHNERT, (1970, 1972); NATHRATH et al, (1971, 1975); GEORGE and KANE, (1972); BONNEVIER, (1971). A number of experiments have also been performed which have clearly demonstrated that element and isotope separation does occur in rotating plasmas. A summary of the results obtained in these experiments, together with the main experimental parameters is given in Table 1.1. A brief description of these experiments will now be given.

TABLE 1.1

MAIN EXPERIMENTAL PARAMETERS OF PLASMA CENTRIFUGES

Rotating Plasma Device	Operation	Gas	Filling Pressure (mtorr)	Magnetic Field (Tesla)	Discharge Current (Amps)	Temperature (°K)	Flow Velocity (ms^{-1})	Separation Factor α
FI Rotating plasma (Bonnevier, 1970)	Pulsed $\underline{J}\times\underline{B}$ rotation, 4ms flowtime	A/H_2	40	0.6	*	$\sim 10^5$	$\sim 10^5$	~ 50.0
		H_2/D_2	40	0.6	*	$\sim 10^5$	$\sim 10^5$	1.4
Supper III (James & Simpson, 1974, 1975)	Pulsed $\underline{J}\times\underline{B}$ rotation 0.7ms flowtime	N_e	10^3	1.5	2.5×10^3	4×10^3	$\leq2\times10^4$ ≠	1.1
Vortex II (Cairns, 1974, 1975)	Pulsed $\underline{J}\times\underline{B}$ rotation 3.5ms flowtime	N_e	50	0.05 – 0.20	8.0×10^3	5×10^4	10^4	1.18
Rotating Arc (Heller & Simon, 1974)	Steady state $\underline{J}\times\underline{B}$ rotation	N_e	11×10^3	0.74	100	*	$\leq2\times10^4$ ≠	1.1
Hollow Cathode discharge in axial magnetic field (Soeschoter, 1975)	Steady state rotation produced by diamagnetic and E/B drift	A	*	0.55	350	$>10^4$	10^4	1.28
		A in H_2 arc	*	0.55	350	$>10^4$	10^4	3.78

* no data given

≠ assessed from the critical velocity phenomenon (see section 2.2)

Although indirect evidence of mass separation in rotating plasma had previously been reported (MAY et al, (1965); ANGERTH et al, (1962)), the first qualitative evidence of mass separation in rotating plasmas was obtained by BONNEVIER (1971) in the FI device shown in Fig.1.1. The experiment has a complicated geometry with a poloidal magnetic field, the discharge taking place between the two anode rings and cathode plate which defines the plasma confinement region. Element separation was studied using a hydrogen/argon mixture and isotopic separation studied using a hydrogen/deuterium mixture and natural neon which consists of 90.9% ^{20}Ne 0.3% ^{21}Ne and 8.8% ^{22}Ne. The plasma flow was sampled at different positions in the discharge by a mechanical valve and analysed by a mass spectrometer. However, although large separations were reported (see Table 1.1), the results were unsatisfactory for a number of reasons. Firstly, the gas mixture did not return to its equilibrium value at the end of the experiment; secondly, there was no time resolution during the pulsed plasma flow; thirdly, no quantitative results of neon isotope separation were given, and finally, the discharge parameters were fixed so that the predicted dependence of the mass separation on plasma conditions was not investigated. For these reasons experimental work began on the Vortex II device in 1972, to investigate Bonnevier's claimed results.

Evidence of separation of the neon isotopes has been obtained by JAMES and SIMPSON (1974) in the Supper III device shown in Fig.1.2. Plasma is produced by discharging a capacitor bank between the concentric electrodes situated at the end of the vessel. The resulting radial current produces a $\underline{j} \times \underline{B}$ ionizing front which travels along the vessel, converting the neutral gas into a rotating plasma. In these experiments gas was collected from the discharge using a fast acting valve and time resolved measurements were obtained. The isotopic ratio was found to return to its equilibrium value, but the radial dependence of the separation factor was not investigated. Although these results were published first, similar results were obtained at approximately the same time by the author with the Vortex II device. Time resolved measurements of the radial dependence of the separation factor were first obtained by the author with the Vortex II experiment described in Chapter IV, (CAIRNS, (1974, 1975)). The phenomenon of two-dimensional separation effects in rotating plasmas was also investigated for the first time.

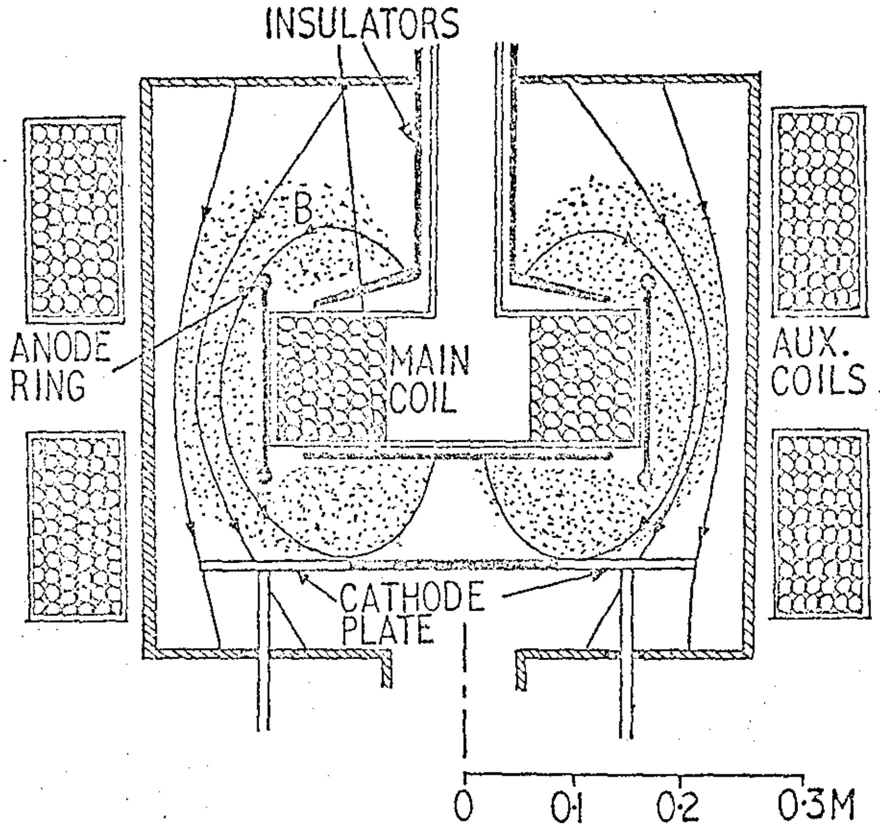

Fig.1.1
Schematic view of the FI rotating plasma device showing the discharge chamber and poloidal magnetic field configuration

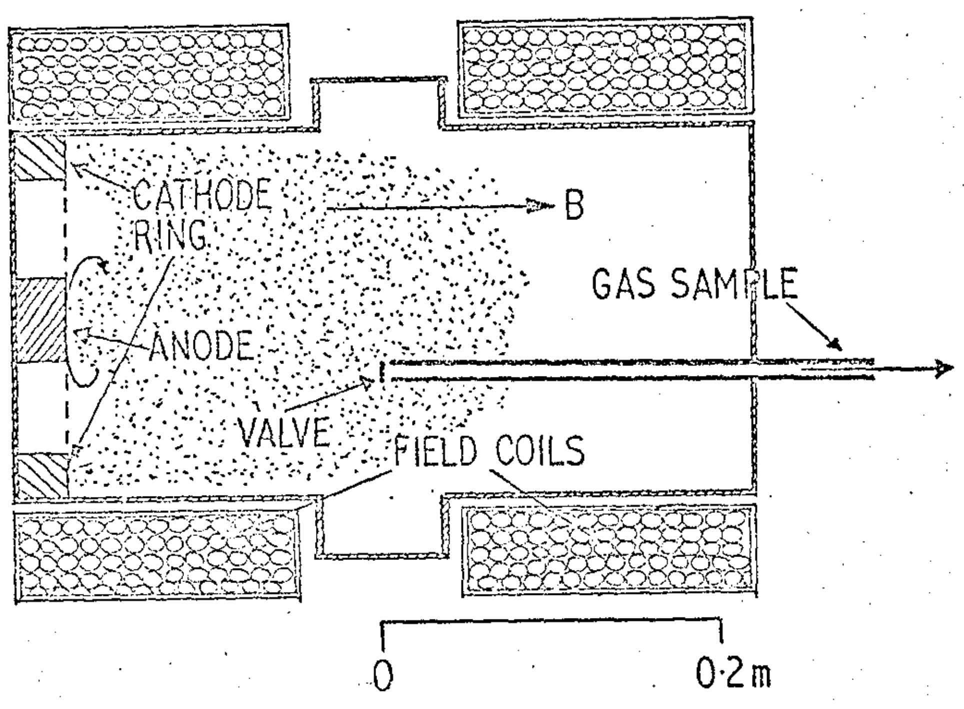

Fig.1.2
The Supper III rotating plasma showing the discharge chamber and the position of the sampling valve

HELLER and SIMON (1974) have recently obtained measurements of neon isotope separation using a steady state rotating plasma device. The discharge chamber is shown in Fig.1.3. Samples were collected at the axial mid-plane and at the outer wall, and analysed with a quadrupole mass spectrometer. Separation factors comparable with the other experiments described above were obtained. No experimental details of the spatial temperature, density and flow were given, and no theoretical comparisons made.

Steady state isotopic separation measurements have also been made by BOESCHOTEN (1975), using the argon isotopes in a hollow cathode discharge experiment which is shown in Fig.1.4. The two most abundant isotopes have mass numbers of 40 (comprising 99.6% of natural argon) and 36 (0.334%) giving a mass ratio of 10%, as with the neon isotopes. High separation factors were obtained using argon discharge, but the most important results were obtained using a hydrogen arc seeded with a small amount (less than 20%) of argon. Argon (40) separation factors of 2.75 were obtained, much larger than the pure argon case. The results were attributed to differences in the radial density distributions between the 'pure' and 'seeded' case. This explanation is tentative however; other mechanisms such as the higher thermal conductivity of hydrogen (therefore cooling the discharge), or faster plasma rotation (see section 2.2), may be responsible. Whatever the reason, this experiment has shown that gas seeding may have important applications in rotating plasma centrifuges.

Research on rotating plasmas is not confined to their possible use as centrifuges. Due to their interesting properties, work on them has been performed on a world-wide scale in many branches of plasma physics, incorporating basic fusion research (BOYER et al, (1958)), gas blanket studies of thermonuclear reactors (LEHNERT, (1970,1975); HELSTEN, et al, (1974a)). energy storage devices (ANDERSON et al. (1959)), injection systems (FORSEN

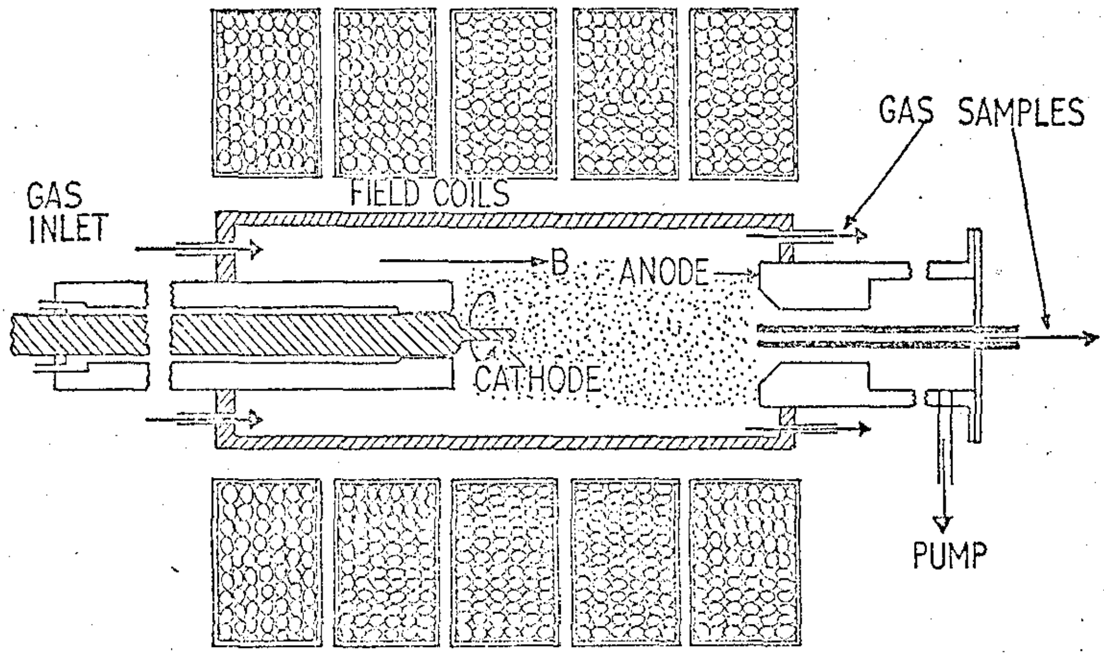

Fig.1.3
The continuously working rotating arc device of Heller et al. The arc is struck between the pin cathode and ring anode. The combination of an axial magnetic field with the radial component of the current causes a rotation of the plasma due to the Lorentz force

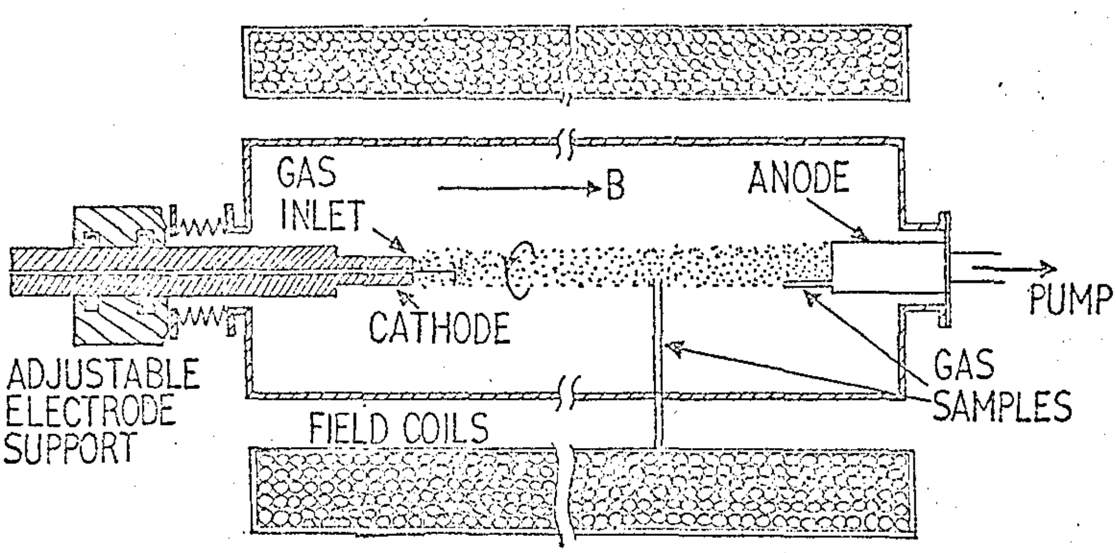

Fig.1.4
Schematic view of the continuously working rotating plasma used by Boeschoten. The arc is struck between the anode and a hollow cathode in an axial magnetic field

et al, (1966); HALBACK et al, (1964); STEINHAUS et al, (1967)), and cosmical physics studies (LEHNERT (1971); SRNKA (1973)). The details of these and many other experiments which can be found in the literature are too extensive to be given here. Largely as a result of the wealth of experimental data available, however, the theory of rotating plasmas has reached a stage where there is a good understanding of the main physical processes which occur in them, allowing realistic predictions to be made of their basic dynamics. The problem of isotopic separation however is still in its early stage and more theoretical and experimental work is required before their efficiency can be accurately compared with other separation techniques. The remaining part of this thesis will describe in detail, the basic theory of rotating plasmas, their possible application as centrifuges, and the Vortex II experiment – a device designed to study isotope separation in rotating plasmas.

CHAPTER II

INTRODUCTION TO THE THEORY OF ROTATING PLASMAS

It is well known that whenever an electric current, $\underline{j}$, is applied across a magnetic field, $\underline{B}$, the resulting Lorentz $\underline{j} \times \underline{B}$ force produces a net fluid motion in the plasma. This Lorentz force has been put to many uses in plasma physics research as mentioned in the preceding chapter. In particular, very high azimuthal velocities can be obtained using specially designed cylindrical geometries, and it may be possible that the resulting high centrifugal forces could be used to separate elements and isotopes efficiently.

The first part of this chapter deals with the basic theory of rotating plasmas and the remaining sections with the main physical effects which are commonly observed in rotating plasma devices. The theoretical aspects of isotope separation are discussed in Chapter III. A review of rotating plasmas has been recently published by LEHNERT (1971).

2.1 BASIC ROTATING PLASMA THEORY

For simplicity the analysis is restricted to the fully ionized region of a rotating plasma, which is sufficiently collisional on the scale of the discharge dimensions, to be analysed using the fluid equations. The plasma contains two types of ions of density $Z_k n_k$ and $Z_q n_q$, and electrons of density n_e. It is contained in the 'homopolar' type geometry shown in Fig.2.1. This is the simplest experimental geometry for producing rotating plasmas and was used by ANDERSON et al (1958) to investigate the basic physics of these devices. It essentially consists of two coaxial electrodes of radii r_1 and r_2, and axial length, h, immersed in a uniform axial magnetic field, B_z. Insulator surfaces are located at $\pm h/2$. Right-handed cylindrical coordinates are used, such that the unit vectors shown are in the positive sense.

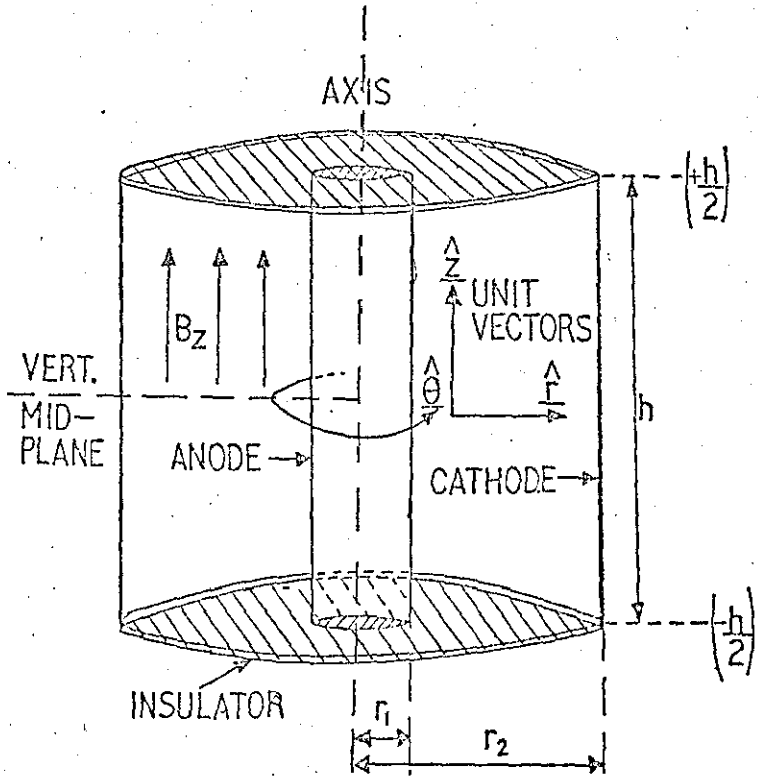

Fig.2.1
Schematic view of the coaxial electrode geometry of the homopolar device (Anderson et al, 1958). Application of a radial current between the anode and cathode in the axial magnetic field shown produces an azimuthal plasma flow

2.1.1 Basic Equations

We begin the theoretical treatment with the well known magneto-hydrodynamic equations which are obtained by taking velocity moments of the Boltzmann equation. The zero order moment determines the particle balance. For the k^{th} species, neglecting ionization and loss processes, this is,

$$\frac{\partial n_k}{\partial t} + \underline{\nabla} \cdot (n_k \underline{v}_k) = 0 \qquad \ldots (2.1)$$

where $\underline{v}_k$ is the velocity of the k^{th} species.

The first order moment gives the equation of motion,

$$n_k m_k \left(\frac{\partial \underline{v}_k}{\partial t} + (\underline{v}_k \cdot \underline{\nabla})\underline{v}_k\right) = n_k Z_k e(\underline{E} + \underline{v}_k \times \underline{B}) - \underline{\nabla} \cdot \underline{\underline{\Psi}}_k - n_k m_k \underline{\nabla} \varphi + \sum_{j \neq k} \underline{P}_{j,k} \qquad \ldots (2.2)$$

where φ is the gravitational potential,

$\underline{\underline{\Psi}}_k$ is the second order stress tensor, and

$\sum_{j \neq k} \underline{P}_{j,k}$ is the total momentum transferred to the k^{th} species per unit time and unit volume, by collisions with the other particle types.

An infinite series of higher moment equations may be obtained from the Boltzmann equation, by suitable substitutions of the velocity moment. However, each new equation contains terms which can only be found from the next equation in the series, and hence, any finite number of equations does not form a closed set. The system can only be terminated if the highest moment is neglected or simplified. In the present case this implies that simplifying assumptions must be made about the stress tensor in equation (2.2). A discussion of this problem is given by SPITZER (1962), who concludes that if the mean free path, λ, is short compared with the distance over which the pressure, p, velocity and other macroscopic quantities change significantly, then the pressure is a scalar quantity and we can put,

$$\underline{\nabla} \cdot \underline{\underline{\Psi}}_k = \underline{\nabla} p_k . \qquad \ldots (2.3)$$

In the case where a shearing velocity is present, transverse to $\underline{B}$ and parallel with surfaces of constant density and pressure, which is usually the case in well confined, azimuthally symmetric rotating plasmas, Spitzer obtains,

$$(\underline{\nabla} \cdot \underline{\underline{\Psi}}_k)_\perp = \underline{\nabla} p_{k\perp} - \underline{\nabla} \cdot (\mu_k \underline{\nabla}\, \underline{v}_k)_\perp \qquad \ldots (2.4)$$

where the second term is the sum of the off-diagonal elements of the stress tensor, and μ_k is the coefficient of viscosity. The subscripts refer to the direction transverse to $\underline{B}$. Finally an equation of state is required for the pressure, p_k, in terms of the other plasma parameters. In the analysis the 'perfect gas approximation' will be used, namely,

$$p_k = n_k k_B T_k \qquad \ldots (2.5)$$

where k_B is Boltzmann's constant, and T_k is the temperature of the k^{th} species. Before considering the total balance of a rotating plasma, the steady state guiding centre velocities of the individual species will be analysed.

2.1.2 *The Particle Velocity Components*

Substituting equation (2.4) into equation (2.2), and neglecting the gravitational term, we obtain in the steady state for the k^{th} species,

$$n_k m_k (\underline{v}_k \cdot \underline{\nabla}) \underline{v}_k = n_k Z_k e(\underline{E} + \underline{v}_k \times \underline{B}) - \underline{\nabla} p_k + \underline{\nabla} \cdot (\mu_k \underline{\nabla}\, \underline{v}_k) + \sum_{j \neq k} \underline{P}_{j,k} \qquad \ldots (2.6)$$

This equation can be considerably simplified if we now assume azimuthal and vertical symmetry with $v_{k\theta} \gg v_{kr}, v_{kz}$ and also that the initial B_z is not modified to a great extent by currents flowing in the plasma, such that $B_z \gg B_r, B_\theta$.

With these assumptions the radial and azimuthal components of equation (2.6) in cylindrical coordinates become respectively,

$$- n_k m_k \frac{v_{k\theta}^2}{r} \approx n_k Z_k e(E_R + v_{k\theta} B_z) - \frac{\partial p_k}{\partial r} + \Big(\sum_{j \neq k} \underline{P}_{j\,k}\Big)_r \qquad \ldots (2.7a)$$

$$n_k m_k \Big(\frac{dv_{k\theta}}{dr} + \frac{v_{k\theta}}{r}\Big) \approx \frac{\partial}{\partial r}\Big(\frac{\mu_k}{r} \frac{\partial}{\partial r}(r\, v_{k\theta})\Big) + \Big(\sum_{j \neq k} \underline{P}_{j\,k}\Big)_\theta \,. \qquad \ldots (2.7b)$$

These two equations are coupled by the momentum transfer term, P_{kj}, which can be written as (BONNEVIER (1966))

$$P_{kj} = - P_{jk} = - n_k n_j \langle \delta v_{kj} \rangle \frac{m_k m_j}{(m_k + m_j)} (\underline{v}_k - \underline{v}_j)$$
$$= - \alpha_{kj} n_k n_j (\underline{v}_k - \underline{v}_j) \qquad \ldots (2.8)$$

Here δ is the Coulomb cross section, v_{kj} is the relative velocity between particles k and j, and $\langle \delta v_{kj} \rangle$ represents the probability of the particles k and j colliding, averaged over the appropriate velocity distribution. For ion-electron collisions, the interaction parameters, α_{kj}, defined by equation (2.8) is given by (SPITZER, (1962)), by

$$\alpha_{ke} = Z_k^2 e^2 \eta \qquad \ldots (2.9)$$

and for ion-ion collisions by

$$\alpha_{kq} = \left(\frac{m_p}{m_e}\right)^{\frac{1}{2}} Z_k^2 Z_q^2 \left(\frac{A_k A_q}{A_k + A_q}\right)^{\frac{1}{2}} e^2 \eta \qquad \ldots (2.10)$$

(TAYLOR, (1961); POST (1959); LONGMUIR and ROSENBLUTH (1956)), where A_k and A_q are the respective mass numbers of the ions, and η is the resistivity of an electron-proton plasma, given by,

$$\eta = \frac{129}{T^{\frac{3}{2}}} \ln \Lambda \ \ \Omega - m \ . \qquad \ldots (2.11)$$

The non-dimensional parameter Λ denotes the ratio between the effective cross-sections of distant and close collisions (HOLT and HASKELL, (1965)).

Inspection of equations (2.9) and (2.10) show that due to the term $(m_p/m_e)^{\frac{1}{2}} \sim 43$, collisions between non-identical ions, in many cases, produce a much larger momentum transfer than that obtained with electron-ion collisions. This has important consequences in the theory of isotope separation in rotating plasmas, as will be seen in the following chapter.

2.1.3 The One-Fluid Equations

The equations formulated above, are useful when analysing the dynamics of individual particle species, and will be used extensively in the next chapter when isotopic separation will be considered. When the behaviour of the entire plasma is analyzed, however, it is mathematically easier to treat the different species, constituting the plasma, as a single fluid.

To obtain the one fluid model, we define expressions for the centre of mass fluid velocity, $\underline{V}$, current density, $\underline{j}$, charge density, δ, and the mass density, ρ, as follows:

$$\underline{V} = \frac{1}{\rho}\left(\sum n_q m_q \underline{v}_q + n_e m_e \underline{v}_e\right) \qquad \ldots (2.12a)$$

$$\underline{j} = e\left(\sum n_q Z_q \underline{v}_q - n_e \underline{v}_e\right) \qquad \ldots (2.12b)$$

$$\delta = \frac{e}{\epsilon_o}\left(\sum n_q Z_q - n_e\right) \qquad \ldots (2.12c)$$

$$\rho = \left(\sum n_q m_q + n_e m_e\right) \qquad \ldots (2.12d)$$

where the summations extend over all the different ion species. Summation of equation (2.1) over the entire plasma, using the above definitions, gives the continuity equation,

$$\frac{\partial \rho}{\partial t} + \nabla . (\rho \underline{V}) = 0 \quad . \qquad \ldots (2.13)$$

Similarly for equation (2.2) with (2.4) we obtain the momentum balance of the 'one fluid' plasma,

$$\rho\left(\frac{\partial \underline{V}}{\partial t} + (\underline{V} . \underline{\nabla})\, \underline{V}\right) = \underline{j} \times \underline{B} - \underline{\nabla} p + \underline{\nabla} . (\mu \underline{\nabla} \underline{V}) \qquad \ldots (2.14)$$

where quasi-neutrality has been assumed and the gravitational potential neglected. The momentum transfer terms have cancelled out as a consequence of Newton's third law.

The equation describing the current, $\underline{j}$, in the plasma, known as the 'Generalised Ohm's Law', can also be obtained from the moment equations in a similar fashion as above. It is usually given by

$$\frac{m_e}{e^2 n_e} \frac{\partial \underline{j}}{\partial t} = \underline{E} + \underline{V} \times \underline{B} - \frac{1}{en_e} \underline{j} \times \underline{B} - \eta \underline{j} + \frac{1}{en_e} \underline{\nabla} p_e \qquad \ldots (2.15)$$

Finally we have Maxwell's equations which complete the set of basic relations used here,

$$\underline{\nabla} \cdot \underline{E} = \frac{\delta}{\epsilon_o} \qquad \ldots (2.16a)$$

$$\underline{\nabla} \cdot \underline{B} = 0 \qquad \ldots (2.16b)$$

$$\underline{\nabla} \times \underline{E} = -\frac{\partial \underline{B}}{\partial t} \qquad \ldots (2.16c)$$

$$\underline{\nabla} \times \underline{B} = \frac{J}{\mu_o} + \frac{1}{\epsilon_o \mu_o} \frac{\partial \underline{E}}{\partial t} \qquad \ldots (2.16d)$$

The second term in (2.16d) represents the displacement current. This is of importance in relativistic plasmas and in plasmas in which high frequency electromagnetic waves are propagating. It can be neglected in the VORTEXplasma.

2.1.4 The Balance of a Steady State Rotating Plasma

Using the same assumptions as those used in the derivation of equation (2.7(a) and (b)) in section 2.1.2, the radial and azimuthal components of the momentum balance and Ohm's law become respectively,

$$-\rho \frac{V_\theta^2}{r} = j_\theta B_z - \frac{\partial p}{\partial r} \qquad \ldots (2.17a)$$

$$j_r B_z = \mu \frac{\partial}{\partial r} \left(\frac{1}{r} \frac{\partial}{\partial r} (rV_\theta) \right) + \frac{1}{r} \frac{\partial}{\partial r} (rV_\theta) \frac{\partial \mu}{\partial r} \qquad \ldots (2.17b)$$

$$\frac{1}{en_e} \left(j_\theta B_z - \frac{\partial p_e}{\partial r} \right) = E + V_\theta B_z - \eta_\perp j_r \qquad \ldots (2.18a)$$

$$\frac{1}{en_e} j_r B_z = - V_r B_z + \eta_\perp j_\theta \qquad \ldots (2.18b)$$

Substitution of the value of j_θ from equation (2.18a) into (2.17a) and solving for the azimuthal velocity, we obtain,

$$V_\theta = -\frac{E_R}{B_z} - \frac{\rho}{en_e B_z} \frac{V_\theta^2}{r} + \frac{1}{en_e B_z} \frac{\partial p_i}{\partial r} + \frac{\eta_\perp}{B_z} j_r \qquad \ldots (2.19)$$

The correction terms to the E/B drift velocity, which is normally dominant in rotating plasmas, therefore arise from the centrifugal drift, which increases the velocity and the positively directed ion pressure gradients and ohmic dissipation which decrease the plasma velocity.

Combining (2.17a) and (2.16d) and neglecting the displacement term, yields the radial balance,

$$\rho \frac{V_\theta^2}{r} = \frac{\partial}{\partial r}\left(\frac{B_z^2}{2\mu_o}\right) + \frac{\partial p}{\partial r} . \qquad \ldots (2.20)$$

Thus the outward centrifugal expansion of the rotating plasma is balanced by both the magnetic pressure and the plasma density gradient. In general, the azimuthal current will contribute in a similar way to the axial balance of the rotating plasma. The effect of the current is to bend the initial axial field lines and produce a radial, B_r, component. Ignoring inertia terms in the axial balance, we have,

$$j_\theta B_r \approx -\frac{\partial p}{\partial z} \qquad \ldots (2.21)$$

implying that the $j_\theta B_r$ force will tend to compress the plasma in the mid-plane regions away from the neutral particle layers at the end insulators. This fact has been used to advantage by ANGERTH et al (1962) and SRNKA (1974) to produce flow velocities in excess of the 'critical velocity' (see section 2.2).

The azimuthal balance is seen immediately from equation (2.17b), which shows that the driving $j_r B_z$ force is balanced by viscous drag. In general, this equation is difficult to solve as it requires detailed knowledge of the boundary conditions of the system; also the viscosity of the rotating plasma will, in general, vary in a complicated fashion over the discharge radius.

Calculations by SHKAROFSKY (1962,1963), give the general expression for the plasma viscosity to be,

$$\mu = \frac{nkT}{\nu_{ii}} \; \frac{g}{g^2 + 4x^2 h^2} \qquad \ldots (2.22a)$$

where g, x and h are functions of the ion-ion collision frequency, ν_{ii}, the ion mass and the magnetic field. For lowly magnetised isothermal plasmas (i.e. when $\omega\tau_{ii} \ll 1$, and $T = \text{constant}$), it is a good approximation to regard the plasma viscosity as a constant. BRAGINSKII (1958) finds the viscosity in this case to be,

$$\mu = 2.21 \times 10^{-16} \frac{T^{\frac{5}{2}} A^{\frac{1}{2}}}{Z^4 \ell n \Lambda} \quad N\,s\,m^{-2} \qquad \ldots (2.22b)$$

In the other extreme, when the plasma is highly magnetised ($\omega\tau_{ii} \gg 1$), the plasma viscosity transverse to the magnetic field is given by (THOMPSON, 1962)

$$\mu_{\perp} = 2.71 \times 10^{-47} \frac{\ell n\Lambda A^{\frac{3}{2}} n^2}{B^2 T^{\frac{1}{2}}} \quad N\,s\,m^{-2} \qquad \ldots (2.22c)$$

Recently, HELSTEN (1974b) has made a detailed, computer aided study of the momentum and heat balance of a fully ionized rotating plasma, using the transport coefficients calculated by Shkarofsky, and by assuming no-slip boundary conditions. The results are presented in Fig.2.2. A

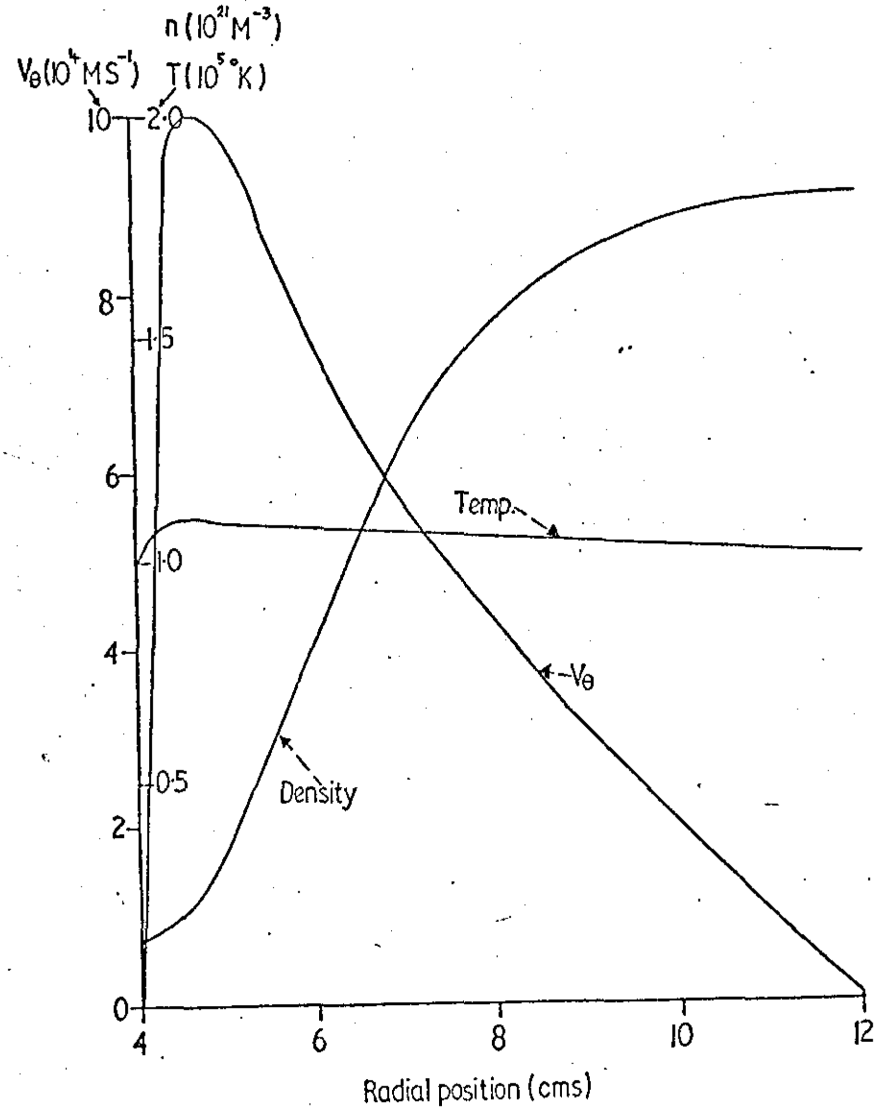

Fig.2.2
The radial balance of a completely ionized, highly magnetized, rotating plasma (from Helsten 1974)

comparison can be made between the velocity profile with variable viscosity, for a high B_z field ($\omega\tau_{ii} \gg 1$) using equation (2.22c), and a Poiseuille flow profile with constant viscosity, shown in Fig.2.4. It is evident that the Poiseuille profile represents a poor approximation in rotating plasmas with large magnetic fields. Nevertheless, primarily due to the ease of mathematical solution, the Poiseuille profile has been widely used to predict some of the salient experimental features of rotating plasmas (see section 2.3).

This completes our treatment of the basic dynamics of rotating plasmas. Attention will now be given to the main physical effects which are commonly observed in rotating plasma devices.

2.2 THE VELOCITY LIMITATION

ALFVÉN (1954,1960) has proposed that when the relative velocity between a plasma and a neutral gas increases to a value:

$$v_{rel} = v_{crit} = \left(\frac{2\,e\,\varphi_n}{m_i}\right)^{\frac{1}{2}} \qquad \ldots (2.23)$$

where φ_n is the ionization potential of the neutral species, a strongly enhanced ionization process should arise, limiting the relative plasma velocity to this value. The calculated values of the critical velocity of certain gases are given in Table 2.1.

TABLE 2.1

THE CRITICAL VELOCITY OF CERTAIN GASES

Gas	Ionized Mass (1.67×10^{-27}kgm)	Ionization Potential Φ (V)	Critical Velocity (km s^{-1})
H	1	13.6	51.0
He	4	24.5	34.4
N	14	14.6	14.2
Ne	20.2	21.6	14.4
A	39.9	15.6	8.7
U	238	~6.0	~2.2

This effect has serious consequences in rotating plasmas where there is nearly always a small but finite amount of residual neutral gas in the main body of the plasma, and, in particular, at the boundary regions. A great many experiments in different geometries have confirmed the validity of Alfvén's original hypothesis (FAHLESON (1960); ANGERTH et al (1962); DANIELSSON (1973)), however, the underlying physical mechanism responsible for it is still not completely understood (see the review by SHERMAN (1973)).

In coaxial geometry, the critical velocity exhibits itself as a voltage limitation across the discharge which is independent of neutral filling pressure and plasma current, over a large experimental range, and about proportional to the magnetic field strength (FAHLESSON (1961); ANGERTH et al (1962); LEHNERT (1971); DANIELSSON, (1970); SRNKA, (1974)). A simple theory of this phenomenon can be easily derived using the one-fluid equations. The total tube voltage, V_T, is given from equation (2.19) as,

$$V_T = \int_{r_1}^{r_2} E_R dr = - \int_{r_1}^{r_2} v_\theta B_z dr + \int_{r_1}^{r_2} \left(\frac{1}{en_e} \frac{\partial p_i}{\partial r} + \eta_\perp j_r - \frac{m_i v_\theta^2}{er} \right) dr + V_s \qquad \ldots (2.24)$$

where a term, V_s, has been added to include the effects of possible voltage drops across the anode sheath (see section 2.5). The pressure gradient, resistive and centrifugal terms contained in the second integral, are usually small compared with the e m f produced by the polarising field, $v_\theta B_z$, (LEHNERT (1971)) and so, if the limiting velocity is present, the voltage will reach a saturation value given by

$$V_{T\,crit} = (r_2 - r_1)\left(\frac{2 e \varphi_n}{m_i}\right)^{\frac{1}{2}} B_z + V_s \qquad \ldots (2.25)$$

This voltage plateau, termed the 'burning voltage' of the discharge, is a main feature of a number of rotating plasma experiments (see the review by LEHNERT (1971)). Both the critical velocity and the flat burning voltage profile have been observed in the present experiment (see section 6.2).

In view of the undesirable effects of such a velocity limitation in a plasma centrifuge or in basic thermonuclear research, some attempts have been made to avoid it. ANGERTH et al (1962) and SRNKA (1974) found that by using sufficiently large radial currents ($\geqslant 10^4$A), the plasma became completely ionized and speeds in excess of the critical velocity could be achieved. The success of these experiments was also attributed to the effective pinching of the plasma away from the end glass insulators by the associated $j_\theta B_r$ force, (see section 2.1.4). Attempts to produce super critical velocities in the F series of experiments at Stockholm, using specially designed poloidal magnetic fields (see Fig.1.1) to prevent plasma from coming into contact with the end insulators, have encountered a number of plasma instability problems (LEHNERT (1972,1973)). Recent experiments performed by HIMMEL and PIEL (1973), however, have indicated that a small admixture of gas with a higher critical velocity than that of the main gas, may increase the velocity of the slower ion species by collisions in the azimuthal direction. Although the two gas species will tend to separate, it is possible that the gas seeding technique could improve the overall efficiency of a plasma centrifuge, as shown by BOESCHOTEN (1975), (see also sections 1.2 and 7.3).

2.3 VISCOUS EFFECTS

Viscous effects at the electrode and insulator surfaces have important consequences in rotating plasmas, and lead to two dimensional effects in the radial current distribution (see section 7.2.1). This problem has been considered by BAKER et al (1961) and by KUNKEL et al (1963), and their simplified treatment is presented here.

Two extreme cases are considered, first, when the axial shear dominates over the radial one, and secondly when the radial shear dominates. In the first case, retaining the dominant terms, equation (2.17b) with

(2.18a) gives

$$\mu \frac{\partial^2 v_\theta}{\partial z^2} = j_r B_z = \frac{1}{\eta_\perp} (E_R - v_\theta B_z) B_z \qquad \dots (2.31)$$

where the viscosity has been assumed constant over the boundary layer region. The solution of this equation, subject to the no slip conditions that $v_\theta = 0$ at $z = \pm {}^h/2$ is given by

$$v_\theta = -\frac{E_R}{B_z}\left(1 - \frac{\cosh {}^z/\delta}{\cosh {}^h/2\delta}\right) \qquad \dots (2.32)$$

where the boundary layer δ is defined by

$$\delta = \frac{1}{B_z}\left(\frac{\delta}{\sigma}\right)^{\frac{1}{2}} \qquad \dots (2.33)$$

The velocity profile given by equation (2.32) for various values of the parameter, ${}^h/\delta$, is shown in Fig.2.3. The function j_r is then found by substitution of equation (2.32) into (2.31). Baker now assumes that $j_r \propto v \propto E \propto {}^1/r$ and calculates the effective resistance of the boundary layer region to be,

$$R_{eff} = \frac{V}{I} = -\frac{\int_{r_1}^{r_2} E_R \, dr}{2\pi r \int_{-h/2}^{+h/2} j_r d_z} = \frac{\ell n(r_2/r_1)}{4\pi\sigma\delta} \coth \frac{h}{2\delta} = R_o M \coth M \qquad \dots (2.34)$$

where the ratio $M = \frac{h}{2\delta}$ is the Hartmann number of this type of channel flow and R_o is the electrical resistance of the plasma disc at zero magnetic field.

The second case analysed is termed the long tube approximation, where the viscous drag is dominated by the radial shear. If only radial shear is considered, the azimuthal component of the equation of motion, equation (2.20b), becomes with the previous approximations,

$$j_r B_z = \frac{I B_z}{2\pi h}\frac{1}{r} = \mu\left(\frac{\partial^2 v_\theta}{\partial r^2} + \frac{1}{r}\frac{\partial v_\theta}{\partial r} - \frac{v_\theta}{r}\right) \qquad \dots (2.35)$$

the solution of which is,

$$v_\theta = \frac{I B_z}{4\pi h\mu}\left(\frac{C_1}{r} + C_2 r - r\,hr\right) \qquad \dots (2.36)$$

Where C_1 and C_2 are determined from the boundary conditions. This gives

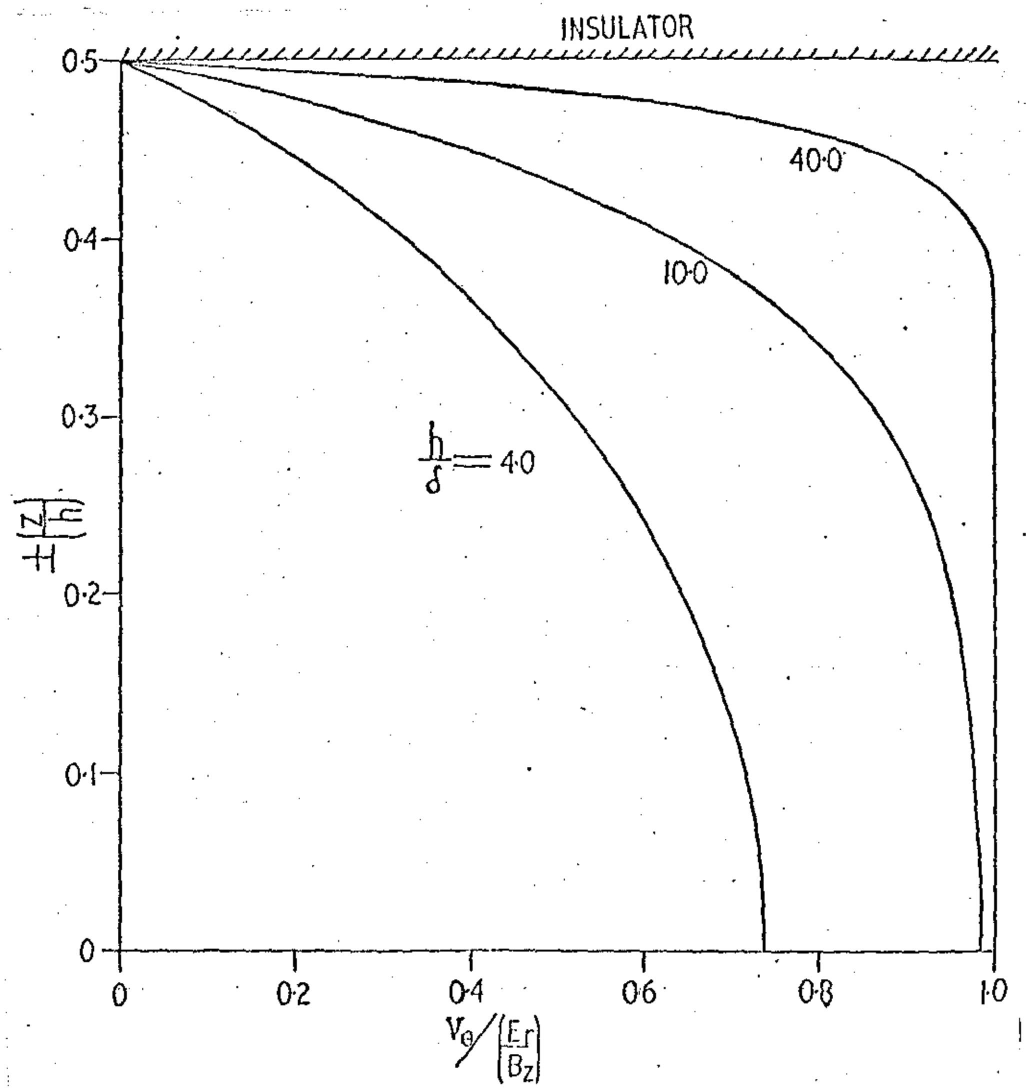

Fig.2.3
Plasma flow profiles of rotating plasma in contact with the end insulators of a homopolar device when the axial shear dominates

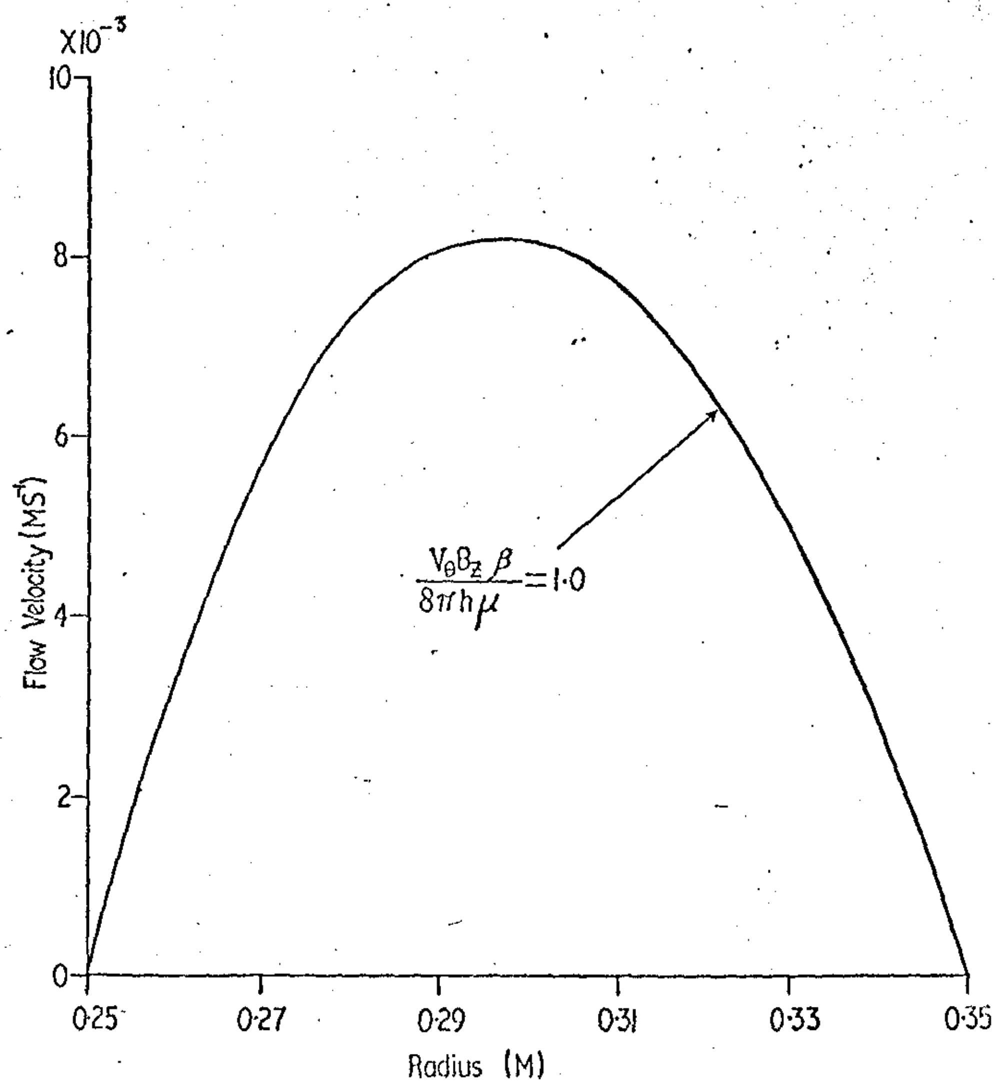

Fig.2.4
Typical Poiseuille flow profile with no slip boundary conditions in a homopolar device when the radial shear dominates

a Poiseuille flow type profile, a typical flow profile is shown in Fig.2.4. For the no-slip boundary condition shown ($v_\theta = 0$ at $r = r_1, r_2$) the constants from equation (2.36 are given by,

$$C_1 = r_1^2 r_2^2 \left(\frac{\ln r_2 - \ln r_1}{r_2^2 - r_1^2}\right).$$

$$C_2 = \left(\frac{r_1^2 \ln r_1 - r_2^2 \ln r_2}{r_2^2 - r_1^2}\right)$$

The effective resistance may now be found in an analogous way as before, using the Generalised Ohm's Law. Baker obtains

$$R_{eff} = R_o \left(1 + \frac{L^2}{\delta^2}\right) \qquad \ldots (2.37)$$

where L^2 represents the area calculated by integrating the bracketed term in (2.36) and dividing by $2\ln(r_2/r_1)$.

The current flowing along the insulator boundary layer may only be neglected if the volume resistance given by equation (2.37) is smaller than that given by equation (2.34), that is we must have, $h \gg 2L^2/\delta$. Since δ is usually very short (~ 1 mm) unless B is very weak, this condition is virtually impossible to fulfil in practice.

This analysis can be summarised as follows: the radial current is only axially uniform at the beginning of the plasma acceleration. When the steady state situation is reached, the high e m f produced by the rotating plasma, forces the majority of the current to flow in the boundary layers at the insulator surfaces. A small radial current is, however, drawn by the rotating plasma to offset viscous drag and loss processes.

2.4 NEUTRAL LAYERS AND PARTIALLY IONIZED REGIONS

When a fully ionized rotating plasma is created in a homopolar device, several mechanisms will lead to neutral and partially ionized regions forming at the electrodes and insulator surfaces. Neutral particles will free stream to the walls; ions and electrons will escape to the insulators along the B_z field by ambipolar diffusion, and diffusion of charged particles will also occur transverse to B_z. Due to their complexity, these regions are not yet completely understood. However, they play an important role in the boundary conditions of the system, and can affect the total balance of the plasma.

LEHNERT (1968, 1975) has analyzed the boundary region of rotating plasmas in some detail, and his main findings can be seen by inspection of Fig.2.5, which shows the behaviour of the neutral and plasma densities near

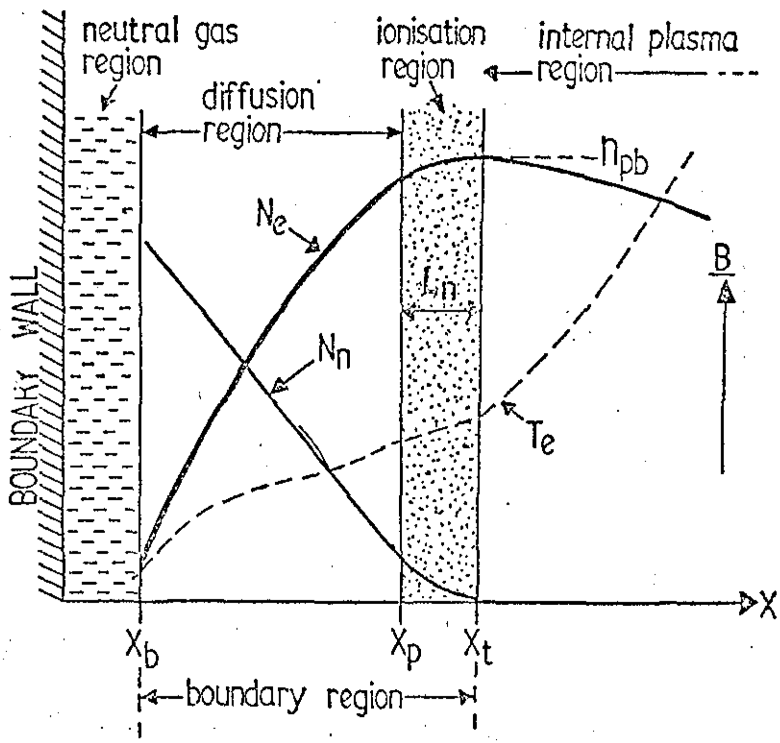

Fig.2.5
The particle balance at the neutral/plasma boundary layer of a rotating plasma

the boundary. Following his analysis, the boundary region can broadly be subdivided into two regions. First, there is a diffusion region $x_b < x \leq x_p$ of low temperature, where the fluxes of ions and neutrals are equal and oppositely directed. Secondly, there is an ionization region $x_p \leq x < x_T$ where the incoming neutrals are ionized due to the increasing temperature, T_e. The extent of the ionization region, L_n, has been calculated by LEHNERT (1968) to have the e-folding length,

$$L_n \approx \frac{1}{n_{pb}} \left(\frac{kT}{m\, \xi_n\, \xi}\right)^{\frac{1}{2}} \qquad \ldots (2.38)$$

where n_{pb} is the plasma density at the boundary (see Fig.2.5), $\xi_n = \frac{\nu_{in}}{n_n}$, $\xi = \xi/n_n$, where ν_{in} is the ion-neutral collision frequency and ξ is the net frequency at which charged particles are produced by ionization. Usually $\xi \ll \xi_n$ in the 'cold' outer regions of the plasma.

The dimension, L_n, is crucial in the formation of a fully ionized rotating plasma. If $L_n \ll (r_2 - r_1)$ then the plasma is said to be 'impermeable' in that it effectively screens itself from the surrounding neutral layer. If, However, L_n is comparable to $(r_2 - r_1)$ then the plasma boundary becomes diffuse and neutral particles can enter the rotating plasma and strongly affect the total balance. The Vortex plasma is characterised by sufficiently high densities at the boundary, n_{pb}, such as to make it impermeable to neutrals (see section 6.4.2).

2.5 ANODE SHEATH FORMATION

In highly ionized rotating plasmas of axial symmetry, a problem arises in that the driving (j_r) current is primarily carried by the ions. Physically this arises due to the fact that the electron Hall parameter $\omega_e \tau_{ei}$ is always much larger than that of the ions (see Table 6.1). Therefore, as the ions drain towards the cathode, the anode must produce ions to preserve the continuity of the electric current. In practice, however, metal electrodes are not perfect sources, or sinks, of ions or electrons, and an electron sheath and depleted ion region will form around the anode.

Such anode sheaths have been observed in homopolar geometry, by SRNKA (1974) and are also evident in the present experiment (see section 6.2). As pointed out by KUNKEL et al (1963) such an electron sheath will have large electric fields associated with it, and the $E \times B$ drift will produce enormous shear stresses which will almost certainly make the region unstable. This instability may well mean that the electrons are able to cross the magnetic field more easily and drain off towards the anode.

CHAPTER III

THE THEORY OF ISOTOPE SEPARATION IN ROTATING PLASMAS

The problem of isotope and element separation in rotating plasmas is, in general, a very complicated one. Consequently no theory published to date has reached a stage where quantitative predictions can be made with any certainty of the detailed performance and efficiency of a plasma centrifuge. The main theoretical difficulties arise in the determination of the complex flow profiles and loss processes, such as diffusion, recombination, viscous friction and heat conduction, which occur in rotating plasmas.

The various theories of isotopic separation using rotating plasmas found in the literature, cover a number of possible operating conditions, ranging from the partially ionized to the fully ionized centrifuge. In this chapter we shall deal mainly with those relating to the fully ionized state, as this corresponds to the plasma conditions in the experimental programme undertaken in this thesis. For completeness, the partially ionized theory is briefly mentioned at the end of the chapter.

3.1 THE THEORY OF BONNEVIER

Although the diffusion of particles in multicomponent plasmas had been analyzed earlier by SPITZER (1952), LONGMIRE and ROSENBLUTH (1956), POST (1959) and TAYLOR (1961), the first theory proposing the use of the high centrifugal forces of rotating plasmas to enrich elements and isotopes was presented by BONNEVIER (1966). For different mass species to be centrifugally separated in rotating plasmas, they must cross the axial magnetic field. To do this they must be acted on by mass dependent azimuthal forces. In his paper, Bonnevier proposed a simple mechanism which could give rise to these forces. In the radial momentum balance, as we shall see, the centrifugal term gives rise to a slightly higher azimuthal velocity for the heavier ions and the subsequent difference in velocity, generates collisional friction between the two species. These frictional forces are azimuthal and oppositely directed. The azimuthal forces across the axial magnetic field, drive the particles radially, outward for the heavier, and inwards for the lighter. Thus enrichment of the heavier ion species should occur at the outer radial positions of a plasma centrifuge.

Bonnevier's theory is obtained from the single particle fluid equations given in Chapter II. A model of a steady state, quasi-neutral, multicomponent plasma, rotating between two coaxial electrodes in an axial magnetic field, is considered. From equation (2.2) and (2.8), neglecting viscous and gravitational terms, the steady state momentum balance is given by,

$$n_k m_k \underline{v}_k \cdot \underline{\nabla} \underline{v}_k = Z_k e n_k (\underline{E} + \underline{v}_k \times \underline{B}) - \underline{\nabla} p_k - \sum_{k \neq q} \alpha_{kq} n_k n_q (\underline{v}_k - \underline{v}_q) \quad \text{.. (3.1)}$$

Vertical and azimuthal symmetry is now assumed with $v_\theta \gg v_r$. In his paper, Bonnevier showed that the latter approximation is valid, provided that the axial magnetic field is sufficiently strong such that $\Omega/\omega_i \ll 1$, where Ω is the plasma angular velocity. With these assumptions, the azimuthal component of equation (3.1) becomes,

$$v_{k\theta} = -\frac{E_R}{B_z} + \frac{1}{Z_k e n_k B_z} \left(\frac{dp_k}{dr} - n_k m_k \frac{v_{k\theta}^2}{r} \right) \quad \text{... (3.2)}$$

where the radial collision term has been neglected as a consequence of $v_\theta \gg v_r$. Equation (3.2) implies that, provided the separation of the ion species is sufficiently small, such that their respective pressure gradient terms are approximately equal, the heavier ion species has a slightly higher azimuthal velocity than the lighter species due to the centrifugal term. This gives rise to ion-ion and ion-electron collisions which produce different radial drifts for the electrons and the two ion species. A schematic diagram of the forces contributing to these drifts is shown in Fig.3.1 With the previous approximation, Bonnevier obtains the magnitude of the radial drift velocity for each species to be,

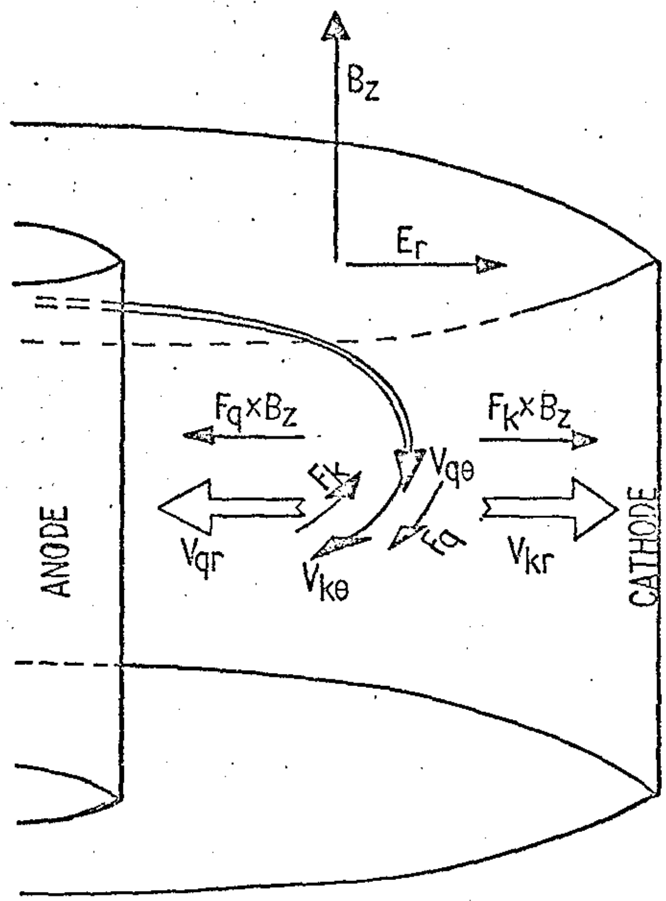

Fig.3.1
Schematic view of the separation process. Collisional friction (F_k and F_q) forces between the ion species lead to oppositely directed radial drifts V_{kr}, V_{qr}

$$v_{kr} = - \frac{1}{Z_n \, e \, B_z} \sum_{k \neq q} \alpha_{kq} n_q (v_{k\theta} - v_{q\theta}) . \qquad \ldots (3.3)$$

Expanding equation (3.3) using (3.2), for a plasma containing two ion species (k and j), and electrons (e), he obtains for the radial velocity of the k^{th} species, neglecting electron inertia,

$$v_{kr} = - \frac{kT}{Z_k e^2 B_z^2} \alpha_{ke} \left(\frac{dn_e}{dr} + \frac{n_e}{Z_k n_k} \frac{dn_k}{dr} - \frac{m_k n_e}{Z_k kT} \frac{v_{k\theta}^2}{r} \right)$$

$$- \frac{kT}{Z_k e^2 B_z^2} \alpha_{kj} \left(\frac{n_j}{Z_k n_k} \frac{dn_k}{dr} - \frac{1}{Z_j} \frac{dn_j}{dr} - \frac{n_j}{kT} \left(\frac{m_k v_{k\theta}^2}{Z_k r} - \frac{m_j v_{j\theta}^2}{Z_j r} \right) \right) \ldots (3.4)$$

It should be noted from the above equation that coefficients of the density gradients depend on the charge, whereas the centrifugal terms contain the charge to mass ratio. This is of importance in fusion reactors, since it means that highly charged impurity ions will tend to concentrate in, and cool, the denser regions of a hydrogen, fusion plasma. If, on the other hand, both ion species are equally ionized in a rotating plasma, then the heavier ions will diffuse in the positive radial direction at a faster rate than the lighter species.

The temperature and densities in the rotating plasma can distribute themselves, in the steady state, in such a way that the radial particle flux due to ion-ion collisions, is zero. Neglecting the electron-ion collision term, α_{ke}, as small compared with the ion-ion term in equation (3.4), (see section 2.1.2), the following is obtained,

$$\frac{n_j}{Z_k n_k}\frac{dn_k}{dr} - \frac{1}{Z_j}\frac{dn_j}{dr} = \frac{n_j}{kT}\left(\frac{m_k v_{k\theta}^2}{Z_k r} - \frac{m_j v_{j\theta}^2}{Z_j r}\right) \qquad \ldots (3.5)$$

This equation can be simplified and solved if we now assume that $Z_k = Z_j = 1$ and that, to a first approximation, $v_{k\theta} \approx v_{j\theta} = V_\theta$. (This is a usual approximation used in conventional centrifuge theory). With these approximations, equation (3.5) has the solution,

$$\frac{\eta}{\eta_o} = \frac{r_o}{r}\exp\left(3\,\theta\frac{(A_k - A_j)}{A_k}\right) \qquad \ldots (3.6)$$

where $\theta = \frac{A_k m_p v_\theta^2}{3\,kT}$ represents the ratio between the energy stored in mass motion and in the thermal energy of the most abundent ion species; $\eta = \frac{n_k}{n_j}$.
This expression should be compared with that for a conventional centrifuge, equation (1.1) in Chapter I. The equations are of the same form, although the fundamental separation process is different.

Under the conditions of a strong magnetic field ($w_i \tau_i \gg 1$) where the present theory is valid, an initial axial magnetic field will have a radial component induced due to the azimuthal current. In this situation there will also be a separation of the ion species along the field, as shown in Fig.3.2. The calculations follow similar lines to those of an undisturbed magnetic field case, and Bonnevier obtains for the separation along the field,

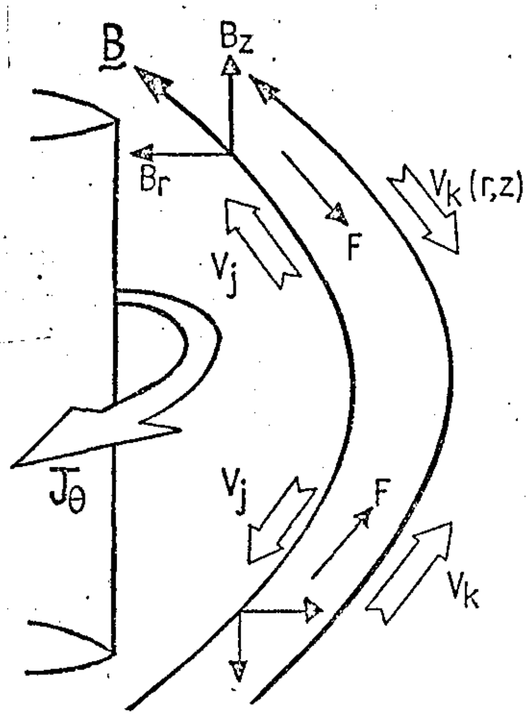

Fig.3.2
Schematic view of the separation process in a poloidal magnetic field. The component of centrifugal force, F, along the field leads to 2-D separation

$$\left(\frac{\eta}{\eta_o}\right)_{\parallel} = \frac{r_o}{r} \exp\left(3\,\theta\;\frac{B_r}{B}\,\frac{A_k - A_j}{A_k}\right) \qquad \ldots (3.7)$$

Thus, in quasi equilibrium, the distribution of ions transverse and parallel to the field, simply depend on the ratio of the two field components, B_r and B_z. Measurements made by BONNEVIER (1971) in the F 1 device, which has a poloidal magnetic field (see Fig.1.1), have shown experimentally that separation does occur along the field, in qualitative agreement with equation (3.7).

3.2 THE THEORY OF McCLURE AND NATHRATH

The theory proposed by McCLURE et al (1971, 1974) and NATHRATH et al (1973, 1975), also applies to fully ionized rotating plasmas. The basic separation mechanism proposed (azimuthal ion-ion collisions) is the same as the Bonnevier model. The main differences between this and Bonnevier's formulation, arise from the fact that firstly, a simple expression is derived (from the one-fluid model) for the azimuthal flow velocity as a function of radius, whereas in Bonnevier's model the azimuthal velocity was treated as an average value; and secondly, the effect of the axial flow of material on the separation factor and density profile is taken into account.

In this theory a model of plasma rotation in a radial electric field and an axial magnetic field, is chosen with a constant temperature throughout the plasma volume. The azimuthal centre of mass velocity of the plasma is determined from the one fluid momentum equation (equation (2.14)). Including radial mass flow, viscous forces and assuming constant viscosity, μ, this is,

$$\frac{d^2 v_\theta}{dr^2} + \frac{(1-\alpha)}{r}\frac{dv_\theta}{dr} - \frac{(1+\alpha)}{r^2} v_\theta = -\frac{j_r B_z}{\mu} \qquad \ldots (3.8)$$

where $\alpha = \frac{m v_r}{\mu}$. Assuming infinite cylinders in the axial direction, we can put $j_r \propto \frac{1}{r}$ giving $j_r B_z = \frac{C}{r}$ where C is a constant. Equation (3.8) now, has the general solution

$$v_\theta = \frac{A}{r} + Br^{(\alpha+1)} - \frac{C}{r\mu} \qquad \ldots (3.9a)$$

for finite radial flux, and,

$$v_\theta = \frac{A}{r} + Br + \frac{C}{2\mu} r \ln r \qquad \ldots (3.9b)$$

for zero radial flux. These solutions give Poisseuille type flow profiles of the type shown earlier in Fig.2.4, and have been used extensively in the literature of rotating plasmas, (LEHNERT, (1971); BAKER et al, (1958)). In their paper McCLURE et al (1971) compared the velocity given by equation (3.9a) and (3.9b) with experimental flow measurements made by SCHWENN (1970), on the hollow cathode high current arc described in section 1.4. Good agreement was found using equation (3.9b) (no axial flow) with the boundary conditions $v_\theta = 0$ at $r = 0$, $r = r_0$ (no slip conditions). However other experiments, for example the Ixion device (BOYER et al (1958)), Vortex I (SRNKA (1974)), steady state rotating plasmas (NOESKE (1971)), and the present experiment, indicate that in other geometries, the Poisseuille flow profile is a poor approximation to the experimental results. Difficulties also arise in the specification of the boundary conditions in coaxial systems, particularly at the inner electrode, due to the anode sheath. In general, the velocity profile can only be obtained from a self consistent analysis of the fluid equations given in Chapter II.

The theoretical derivation of the separation factor now proceeds along similar lines to Bonnevier's formulation. However, in this case, since the velocity profile is known and constant temperature has been assumed, unique solutions of the separation factor and density distribution can be obtained.

A quasi-neutral plasma containing electrons and two ions species (k and j) is considered. Writing the momentum equation for each species (equation (3.4)) and introducing the quantities $w_k = \frac{Z_k e B_z}{m_k}$, $u_{k\theta} = v_{k\theta} - v_\theta$, $\tau_{kj} = \frac{m_k}{\alpha_{kq} n_q}$ and $\Omega = \frac{v_\theta}{r}$, they obtain a system of three inter-related differential equations involving the densities and the particle fluxes, $\Gamma_k = n_k v_{kr}$. By neglecting quantities of the order $\left(\frac{u_{k\theta}}{v_\theta}\right)^2$ and $\left(\frac{\Omega}{w_k}\right)$ and assuming that $Z_k = Z_j = Z$, the following is obtained

$$\frac{d\eta}{dr} - \frac{(m_k - m_j)}{kT} \frac{v_\theta^2}{r} \eta = \frac{eB_z}{kT} \frac{(1+\xi^2)}{n_e \xi} Z (\eta\Gamma_k - \Gamma_q) \qquad \text{... (3.10)}$$

where

$$\xi = \frac{m_k Z}{eB} (\alpha_{ej}^* + Z_q \alpha_{qj}^*),$$

α^* being the value of α for $Z = 1$.

For the density distribution the following is obtained,

$$\frac{dN^2}{dr} - \frac{2m_k v_\theta^2}{(Z+1)\beta_{ke}^* kT} N^2 = \frac{2 e B_z Z^2}{(Z+1)\beta_{ke}^* kT} (\Gamma_k + \Gamma_q) \qquad \text{... (3.11)}$$

where

$$\beta_{ke}^* = \frac{1}{(\omega_e n_e \tau_{ke})}.$$

The general solution of equation (3.10) for $\xi \gg 1$ is given by,

$$\frac{\eta}{\eta(r_1)} = \left\{ 1 - \frac{eB_z \beta^* Z}{kT\eta(r_1)} \int_{r_1}^{r} \Gamma_q(r') e^{-\left[\frac{m_k - m_j}{kT} \int_{r_1}^{r'} \frac{v_\theta^2}{r''} dr'' - \frac{eB\beta^* Z}{kT} \int_{r_1}^{r'} \Gamma_k(r'') dr''\right]} dr' \right\}$$
$$e^{\frac{(m_k - m_j)}{kT} \int_{r_1}^{r} \frac{v_\theta^2}{r'} dr' + \frac{eB\beta^* Z}{kT} \int_{r_1}^{r} \Gamma_k(r') dr'} \qquad \text{... (3.12)}$$

and for equation (3.11) for all ξ, by,

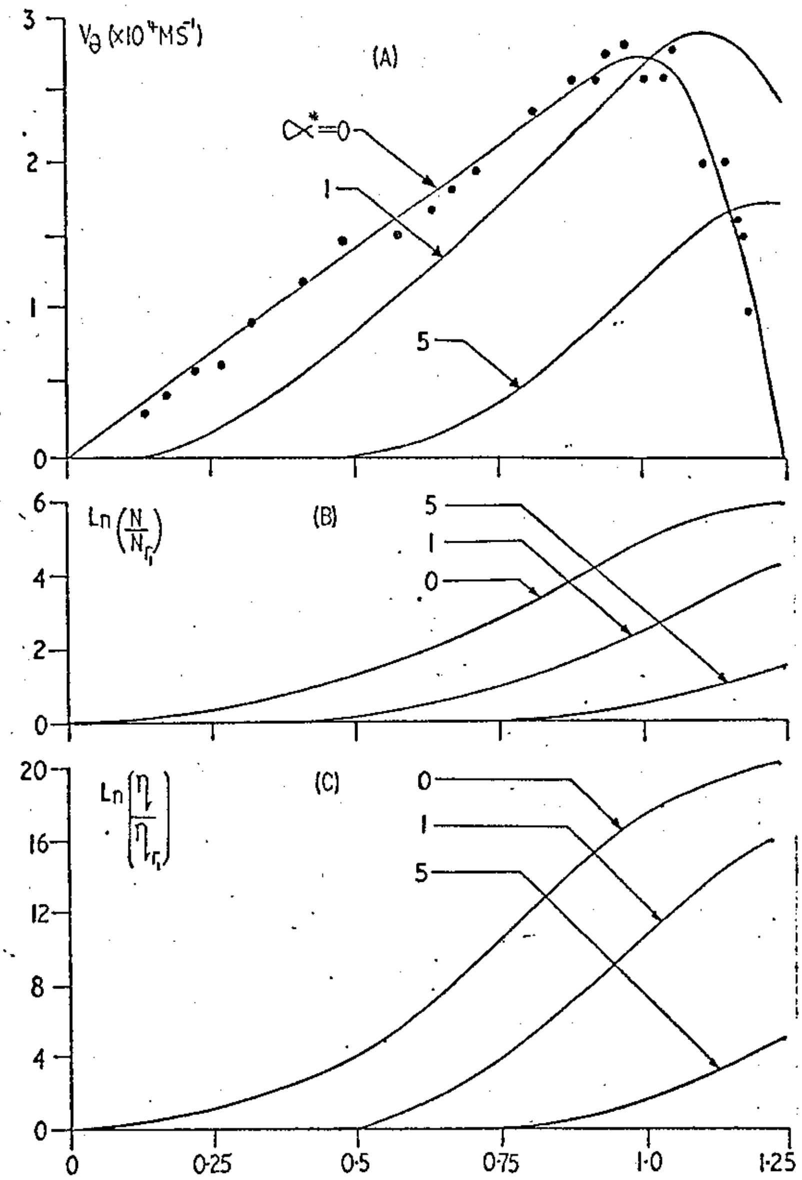

<u>Fig.3.3</u>

The variation of (A) plasma flow velocity, v_θ; (B) density, N, and (C) separation factor, η, with radius. (Calculated from equations (3.12) and (3.13), with $B_z = 1T$, $T = 3.5\times10^4$ ^oK, $\Delta M = 3AMU$, $M_k = 1$ AMU). The experimental results of SCHWENN (1970) are shown for comparison

$$N = N_k^2 - \frac{2 e B_z Z^2}{(Z+1)\ \beta^*_{ke} kT} \int_{r_1}^{r} e^{-\frac{2m_k}{(Z+1)kT}\int_{r_1}^{r'} \frac{V_\theta^2}{r''} dr''} \left[\Gamma_k(r') + \Gamma_q(r')\right] dr'$$

$$\times\ e^{\frac{m_k}{(Z+1)kT}\int_{r_1}^{r} \frac{V_\theta^2}{r'} dr'} \quad . \qquad \ldots (3.13)$$

Hence unique solutions can be calculated for the separation factor. In the limit of no radial flux, equation (3.12) reduces to that given by Bonnevier (equation (3.6)) if an average value of the flow velocity is taken over the radius. Equations (3.12) and (3.13) are plotted in Fig. 3.3 for various values of the parameter α (corresponding to the radial flow of material). It can be seen that any outward for of material reduces both the separation factor and the density gradient.

3.3 A NEW APPROACH

The theory of NATHRATH et al presented above, depends on the assumption that the V_θ profile has a Poisseuille flow profile. In general this is not the case for reasons already mentioned. Another consideration is that the radial electric field is an easier quality to measure experimentally than the plasma flow velocity. A different approach was therefore adopted by the author and HAAS (1974), in which the separation factor was calculated in terms of the radial electric field component. The model of isotopic separation developed in this section also takes into account the effect of radial flow of material on the separation factor and the density distribution.

A model of a quasi-neutral, azimuthally symmetric rotating plasma, containing singly ionized ions of type k and j with $m_j > m_k$ and $n_k \gg n_j$ is considered rotating between two infinitely long coaxial electrodes of radii $r = r_1$ and $r = r_2$ in an axial magnetic field, B_z. The main steps of the development are given here, a more rigorous treatment is given in Appendix 1.

3.3.1 The Density Profile

From equation (3.2) we assume to a first approximation, that the flow velocity is related to the electric field by the following equation:

$$v_\theta \approx -\frac{E_R}{B_z} \quad . \qquad \ldots (3.14)$$

This is normally a good approximation in rotating plasmas and is valid in the Vortex II plasma as shown in section 6.6. Substituting equation (3.14) into equation (3.2) we obtain for the first order ion and electron velocities,

$$v_{k\theta} = -\frac{E_R}{B_z} + \frac{m_k}{eB_z}\left[\frac{kT}{m_k}\frac{1}{n_k}\frac{dn_k}{dr} - \frac{1}{r}\frac{E_R^2}{B_z^2}\right] \qquad \ldots (3.15a)$$

$$v_{j\theta} = -\frac{E_R}{B_z} + \frac{m_j}{eB_z}\left[\frac{kT}{m_j}\frac{1}{n_j}\frac{dn_j}{dr} - \frac{1}{r}\frac{E_R^2}{B_z^2}\right] \qquad \ldots (3.15b)$$

$$v_{e\theta} = -\frac{E_R}{B_z} - \frac{kT}{eB_z}\frac{1}{n_e}\frac{dn_e}{dr} \qquad \ldots (3.15c)$$

where constant temperature has been assumed and the electron inertial term neglected. Similarly, from equation (3.4) we obtain the radial components of the particle velocities; for the k^{th} species we have,

$$v_{kr} = -\frac{kT}{e^2B_z^2}\,\alpha_{ke}\left(\frac{dn_e}{dr} + \frac{n_e}{n_k}\frac{dn_k}{dr} - \frac{m_k n_e}{kT}\frac{E_R^2}{B_z^2 r}\right)$$

$$-\frac{kT}{e^2B_z^2}\,\alpha_{kj}\left(\frac{n_j}{n_k}\frac{dn_k}{dr} - \frac{dn_j}{dr} - \frac{n_j}{kT\,r}\frac{E_R^2}{B_z^2}\left(m_k - m_j\right)\right) \qquad \ldots (3.16)$$

Similar expressions are obtained for the j^{th} ion species and the electrons, as shown in Appendix 1.

The one dimensional radial continuity equations for the particle species, in the absence of ionization and loss terms, are given by,

$$n_k\, v_{kr}\, r = A_k \qquad \ldots (3.17a)$$

$$n_j\, v_{jr}\, r = A_j \qquad \ldots (3.17b)$$

$$n_e\, v_{er}\, r = A_e \quad . \qquad \ldots (3.17c)$$

Substituting the electron radial velocity component (equation (A1.4c) into equation (3.17c), we obtain the following equation for the electron density,

$$- \frac{A_e e^2 B_z^2}{kT\, \alpha_{ke}\, r} = \frac{dn_e^2}{dr} - \frac{E_R^2}{kT\, B_z^2\, r} \quad n_e(n_k m_k + n_j m_j) \ . \qquad \ldots (3.18)$$

We now assume that $n_j \ll n_k$ throughout the plasma volume (valid for many isotopes), giving $n_k m_k \gg n_j m_j$ if $m_j \sim m_k$. This also implies that $n_k \sim n_e$ from quasi neutrality. With these assumptions, equation (3.18) may be written,

$$- \frac{A_e e^2 B_z^2}{kT\, \alpha_{ke}\, r} = \frac{dn_e^2}{dr} - \frac{E_R^2}{kT\, B_z^2\, r} m_k n_e^2 \ . \qquad \ldots (3.19)$$

Equation (3.19) can only be solved if the $E_r(r)$ dependence is known. This can, in principle, be found from a self-consistent analysis of the fluid equations which would require extensive computation beyond the scope of this thesis. Rather we specify a function for E_R to give an analytical expression for the separation factor and the density profile. In particular, we use the vacuum electric field (i.e. assume no space charge) giving the electric field,

$$E_R = E_{(r_1)} \ \frac{r_1}{r} \qquad \ldots (3.20)$$

where $E_{(r_1)}$ is the value of the electric field component at the inner electrode. Substituting equation (3.20) into equation (3.19), we obtain a first order linear differential equation for the electron density,

$$- \lambda = x \frac{dy}{dx} - \frac{y}{x} \mu \qquad \ldots (3.21)$$

where

$$\lambda = \frac{A_e e^2 B_z^2}{2kT\, \alpha_{ke}} \ , \quad y = n_e^2 \ , \quad x = r^2 \ \text{and} \ \mu = \frac{E_{(r_1)}^2 r^2 m_k}{2kT\, B_z^2} \ .$$

This has the solution,

$$\frac{y}{y(r_1)} = e^{-t} \left[e^{t(r_1)} + \frac{\lambda}{y_{(r_1)}} \left(\int_{-\infty}^{t} \frac{e^t}{t}\, dt - \int_{-\infty}^{t(r_1)} \frac{e^t}{t}\, dt \right) \right] \qquad \ldots (3.22)$$

where $t = \mu/x$, and $t_{(r_1)}$ and $y_{(r_1)}$ are the initial conditions at $r = r_1$. The integrals contained in equation (3.22) are related to exponential integrals and can be found from standard mathematical tables. Equation (3.22) therefore gives the radial electron distribution and also, due to the quasi-neutrality condition, the radial distribution of the combined $(n_k + n_j)$ ion species. For finite λ (radial flux), the radial flux decreases the density gradient.

3.3.2 The Separation Factor

To calculate the separation factor, η, we next consider the ion continuity equations, together with the radial ion velocities. Combining equation (3.16) with equation (3.17a), we obtain,

$$\frac{\alpha_{ke}}{e^2B_z^2}\left[r\,kT\left(n_e\frac{dn_k}{dr} + n_k\frac{dn_e}{dr}\right) - \frac{E_R^2}{B_z^2}m_k n_k n_e\right]$$
$$+\frac{\alpha_{nj}}{e^2B_z^2}\left[r\,kT\left(n_j\frac{dn_k}{dr} - n_k\frac{dn_j}{dr}\right) + \frac{E_R^2}{B_z^2}n_k n_j(m_j - m_k)\right] = -A_k. \qquad \ldots (3.23)$$

Since in our approximation $n_k \sim n_e$, the first three terms in equation (3.23) reduce as a first approximation to,

$$\frac{\alpha_{ke}}{e^2B_z^2}\left[r\,kT\frac{dn_e^2}{dr} - \frac{E_R^2}{B_z^2}m_k n_e^2\right]$$

which is $-A_e$ from equation (3.19). Equation (3.23) can now be written,

$$\frac{\alpha_{kj}}{e^2B_z^2}\left[r\,kT\,n_k^2\frac{d}{dr}\left(\frac{n_j}{n_k}\right) - \frac{E_R^2}{B_z^2}n_k n_j(m_j - m_k)\right] = -(A_e - A_k) \ . \qquad \ldots (3.24)$$

For zero radial current, J_R, it is easy to show from equation (3.17a,b,c) and equation (3.12b) that $(A_e - A_k) = A_j$, the radial flux of the heavier, less abundant ion species. Setting $J_R = 0$ is a reasonable approximation in the body of rotating plasmas, as shown in the discussion of viscous effects in section 2.3.

Dividing equation (3.24) through by n_k^2, setting $A_e - A_k = A_j$ and rearranging using (3.20), we obtain an equation describing the radial dependence of the separation factor,

$$\frac{d\eta}{dx} = \left(\frac{E_{(r_1)} r_1}{B_z}\right)^2 \left(\frac{m_j - m_k}{2\,kT}\right) \frac{\eta}{x^2} - \frac{A_j\, e^2 B_z^2}{2\,\alpha_{kj}\, kT} \left(\frac{1}{yx}\right) \qquad \ldots (3.25)$$

which has the solution,

$$\eta = \eta_{(r_1)} \exp\left(-\frac{\gamma}{x}\right)\left(\exp\left(\frac{\gamma}{x_{(r_1)}}\right) - \frac{\beta}{\eta_{(r_1)}} \int_{r_1}^{x} \frac{1}{xy} \exp\left(\frac{\gamma}{x}\right) dx\right) \qquad \ldots (3.26)$$

where $\beta = \dfrac{A_j\, e^2 B_z^2}{2\,\alpha_{kj}\, kT}$, $\gamma = \left(\dfrac{E_{(r_1)} r_1}{B_z}\right)^2 \left(\dfrac{m_j - m_k}{2\,kT}\right)$

with x and y defined in equation 3.21.

Equation (3.25) may be normalised by setting,

$$Y = \frac{y}{y_{(r_1)}} \quad , \quad X = \frac{x}{r_1} \quad , \quad \eta^* = \frac{\eta}{\eta_{(r_1)}}$$

giving

$$\frac{d\eta^*}{dX} = \left(\frac{m_j - m_k}{2kT}\right)\left(\frac{E_{(r_1)}}{B_z}\right)^2 \frac{\eta^*}{X^2} - \frac{A_j\, B_z^2\, T^{\frac{1}{2}}}{2\left(\frac{m_p}{m_e}\right)^{\frac{1}{2}}\left(\frac{A_k A_j}{A_k + A_j}\right)^{\frac{1}{2}}}\, 129\, \ln\Lambda\, y_{(r_1)}\, \eta_{(r_1)}\, YX \qquad \ldots (3.27)$$

where we have used equations (2.10) and (2.11). Provided the separation factor is small, we can also put as a first approximation,

$$\frac{A_j}{\eta_{(r_1)}} \approx A_e \frac{\eta}{\eta_{(r_1)}} = A_e\, \eta^* \, . \qquad \ldots (3.28)$$

Substituting equation (3.28) into equation (3.27) we obtain the following:

$$\frac{d}{dX}(\ln\eta^*) = \left(\frac{m_j - m_k}{2\,kT}\right)\left(\frac{E_{(r_1)}}{B_z}\right)^2 \frac{1}{X^2} - \frac{A_e\, B_z^2\, T^{\frac{1}{2}}}{258k\, \ln\Lambda\, y_{(r_1)} \left(\frac{m_p}{m_e}\right)^{\frac{1}{2}}\left(\frac{A_k A_j}{A_k + A_j}\right)^{\frac{1}{2}}} \frac{1}{YX} \qquad \ldots (3.29a)$$

$$= \left(\frac{m_j - m_k}{2\,kT}\right)\left(\frac{E_{(r_1)}}{B_z}\right)^2 \frac{1}{X^2} - \frac{\beta^*\, T^{\frac{1}{2}}}{\left(\frac{m_p}{m_e}\right)^{\frac{1}{2}}\left(\frac{A_k A_j}{A_k + A_j}\right)^{\frac{1}{2}}}\, YX \qquad \ldots (3.29b)$$

with Y given from equation (3.21) as,

$$\frac{d}{dX}(\ln Y) = \left(\frac{E_{(r_1)}}{B_z}\right)^2 \frac{m_k}{2kT} X^2 - \frac{A_e B_z^2 T^{\frac{1}{2}}}{258k \ln \Lambda y_{(r_1)}} YX \qquad \text{... (3.30a)}$$

$$= \left(\frac{E_{(R_1)}}{B_z}\right) \frac{m_k}{2kT} X^2 - \frac{\beta^* T^{\frac{1}{2}}}{YX} \qquad \text{... (3.30b)}$$

Equations (3.29b) and (3.30b) thus give unique solutions for the density and separation factor for a given radius and set of plasma parameters. These two coupled equations have been solved numerically using a standard Runge-Kutta routine available from the Culham Laboratory computer library (HODGE et al (1969); EDGLEY (1975)). The solutions of equations (3.29b) and (3.30b) for different plasma parameters with the neon isotopes are shown in Figs.3.4 and 3.5. They have been calculated on the basis that the maximum value of the electric field (occurring at the inner radius at $r = r_1$) is given by the critical electric field discussed in section 2.2. That is

$$E_{(r_1)} = E_{crit} = B_z\left(\frac{2 e \varphi_k}{m_k}\right)^{\frac{1}{2}} \qquad \text{... (3.31)}$$

The solutions show that the separation factor depends strongly on the temperature (as do conventional centrifuges), but that the radial outflow of material, specified by the parameter β^*, defined by equations (2.29) and (2.30), has only a minor effect on the separation of the two ion species. This results from the fact that, although to a first approximation with no radial flux, the interaction parameter, α_{hj}, has no effect on the separation factor; when there is a finite radial flux, the magnitude of the correction term (the second term on the right-hand side of equation (3.29b)) is small, since α_{kj} is large, increasing with mass. This implies that the first order approximation of Bonnevier, (equation (3.6)), should represent a good approximation for the separation factor, particularly for the heavy isotopes, if the velocity profile is known. The radial density gradient, however, is more dependent on the radial flux.

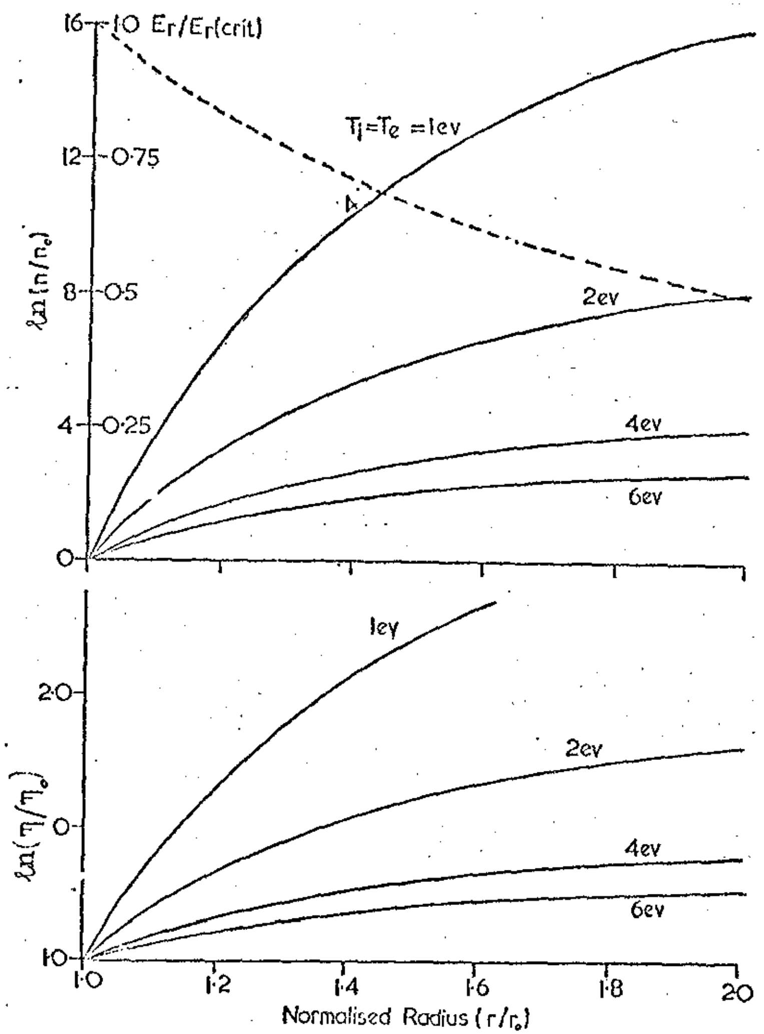

Fig.3.4

The variation of plasma density, n, and separation factor, η, with temperature in a rotating neon plasma

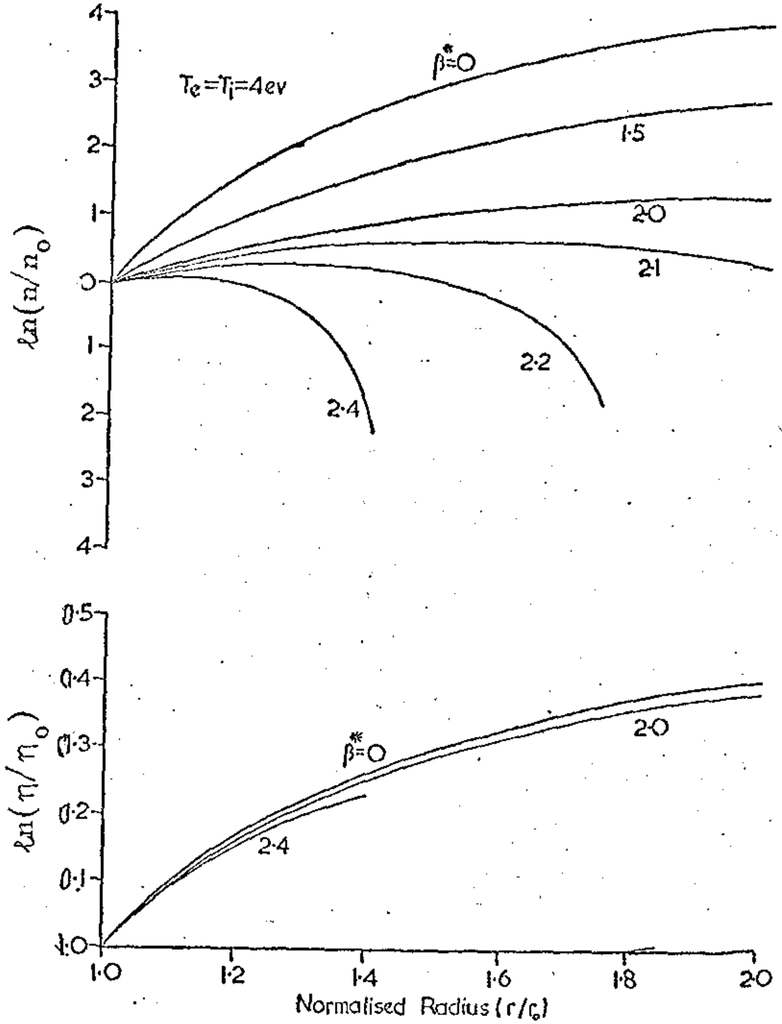

Fig.3.5

The variation of plasma density, n, and separation factor, η, with the parameter β^* in a rotating neon plasma

3.3.3 Boundary Conditions

Two further conditions remain to be fulfilled before the separation factor given by equation (3.29), and the density profile, given by equation (3.30), are completely determined, since the boundary conditions used have been completely arbitrary. These boundary conditions may be specified by evoking two conservation relations which are; firstly, the total number of ions, N, is constant across the radius (since the problem considered is purely one-dimensional); and secondly, the ratio, η_A, of the total number of the two ion species across the radius is also constant.

These conditions enable the boundary conditions of the density and separation factor to be obtained for a given total number of particles and isotopic abundance, and are written,

$$\int_{r_1}^{r_2} (n_k + n_j)\, r\, dr = \frac{N}{2\pi h} \qquad \ldots (3.32)$$

$$\frac{\int_{r_1}^{r_2} n_j\, r\, dr}{\int_{r_1}^{r_2} n_k\, r\, dr} = \frac{N_j}{N_k} = \eta_A \qquad \ldots (3.33)$$

For simplicity, these criteria will be applied to a rotating plasma with no radial flux. The inclusion of radial flux is straightforward in principle, but complicates the problem unduly. Even the present idealised case of the $\frac{1}{r} E_R$ profile leads to problems requiring computation, as will be shown.

In the absence of radial flux, equation (3.21) may be solved to give, after some rearrangement,

$$(n_k + n_j) = (n_k + n_j)_{r_1} \exp \frac{1}{2r_1^2}\left(1 - \frac{r_1^2}{r^2}\right) \qquad \ldots (3.34)$$

Similarly, equation (3.25) has the solution,

$$\eta = \frac{n_j}{n_k} = \left(\frac{n_j}{n_k}\right)_{r_1} \exp \frac{\gamma}{r_1^2}\left(1 - \frac{r_1^2}{r^2}\right) \qquad \ldots (3.35)$$

The density boundary condition, $(n_k + n_j)_{r_1}$ is given from equation (3.32) and equation (3.34) as,

$$(n_k + n_j)_{r_1} = \frac{N\, e^{-1/2r_1^2}}{2\pi h \int_{r_1}^{r_2} r\, e^{-1/2r^2}\, dr} \qquad \ldots (3.36)$$

The integral is given by

$$\int_{r_1}^{r_2} r\, e^{-1/2r^2}\, dr = \frac{1}{4}\left[2 r_2^2\, e^{-1/2r_2^2} - 2 r_1^2\, e^{-1/2r_1^2} + E_i\left(\frac{1}{2r_1^2}\right) - E_i\left(\frac{1}{2r_2^2}\right)\right] \qquad \ldots (3.37)$$

where $E_i(x)$ represents the exponential integral defined by,

$$E_i(x) = \int_x^\infty \frac{e^{-t}}{t}\, dt \ .$$

The calculation of the separation factor boundary condition, $\left(\frac{n_j}{n_k}\right)_{r_1}$, is slightly more involved. From equations (3.32), (3.33), (3.34) and (3.35), we obtain,

$$\int_{r_1}^{r_2} n_k\, r\, dr = \int_{r_1}^{r_2} \frac{(n_k + n_j)_{r_1}\, r \exp \frac{1}{2r_1^2}\left(1 - \frac{r_1^2}{r^2}\right) dr}{1 + \left(\frac{n_j}{n_k}\right)_{r_1} \exp \frac{\gamma}{r_1^2}\left(1 - \frac{r_1^2}{r^2}\right)} = \frac{N_k}{2\pi h} = \frac{N}{(1+\eta_A)\, 2\pi h} \qquad \ldots (3.38)$$

and using equation (3.36) we finally obtain

$$\int_{r_1}^{r_2} \frac{r\, e^{-1/2r^2}\, dr}{1 + \left(\frac{n_j}{n_k}\right)_{r_1} e^{\gamma/r_1^2}\, e^{-\gamma/r^2}} = \frac{\int_{r_1}^{r_2} r\, e^{-1/2r^2}\, dr}{(1 + \eta_A)} \qquad \ldots (3.39)$$

The integral on the left-hand side has, to the author's knowledge, no known analytic solution. The equation may only be solved by specifying a value of $(n_j/n_k)_{r_1}$ and calculating the integral either by graphical or computer methods and 'shooting' for the required η_A. It should be noted from equation (3.39) that the separation factor boundary condition is independent of the plasma density.

3.4 THE PARTIALLY IONIZED CENTRIFUGE

In contrast to the fully ionized centrifuge theories presented above, LEHNERT (1970) has considered the theoretical aspects of mass separation in a partially ionized centrifuge consisting mainly of neutral gas. Under certain experimental conditions, he suggests that the neutrals can be accelerated by the volume force produced by collisions with the rotating ions and electrons, putting them into rotation in a more efficient way than by the viscous shear forces of a mechanical rotor. In a later paper (LEHNERT (1973a)), the theory is extended and put on a more analytical basis. Also in this paper the possibility of controlling the $v_\theta(r)$ profile by external imposed electric and magnetic fields is considered.

For completeness, the theory of BOESCHOTEN (1975) should also be mentioned in this section. He has proposed that a rotating plasma could be used to replace the rotor in a partially ionized device.

CHAPTER IV

THE VORTEX II ROTATING PLASMA EXPERIMENT

The Vortex II experiment is a modified version of an earlier device built at Culham Laboratory by SRNKA (1973). It is a rotating plasma experiment built in homopolar geometry and designed to study the isotopic separation effect in rotating plasma. A general view of the experiment, together with some of the diagnostics used, is shown in Fig.4.1.

The experiment basically consists of a coaxial electrode system in an axial magnetic field. The annular vacuum vessel is filled with gas (usually neon), at a pressure of 50 mtorr, which is then pre-ionized by an oscillating radial current from a capacitor bank. A critically damped current pulse, of ~3.5 ms duration from the main capacitor bank, then sets the resulting plasma into rotation. Various diagnostics, which are described in the next chapter, are used to determine the flow parameters and plasma composition. This chapter gives a detailed description of the construction and power supplies of the machine.

4.1 THE DISCHARGE CHAMBER

The fundamental part of the apparatus is a coaxial, non-magnetic stainless steel electrode system of radii 0.15 m and 0.35, and height 0.3 m. The set-up is shown in Fig.4.2. Pyrex glass sheets of thickness 0.02 m are located at the top and bottom of the electrodes. 'O' ring seals are used throughout the machine so that the interelectrode space can be evacuated. Diagnostic ports are situated on the outer electrode and on the top glass insulator, enabling radial and vertical probe scans to be made in the discharge. The addition of holes in the glass insulator proved a special problem in the Vortex machine. Holes drilled in glass give rise to microcracks and subsequently weaken its mechanical properties. A 0.025 m glass fibre sheet was therefore positioned above the top glass insulator to prevent the possibility of implosion.

FIG.4.1
General view of the experimental area, showing the VORTEX 11 rotating plasma device, the laser and mass analysing system

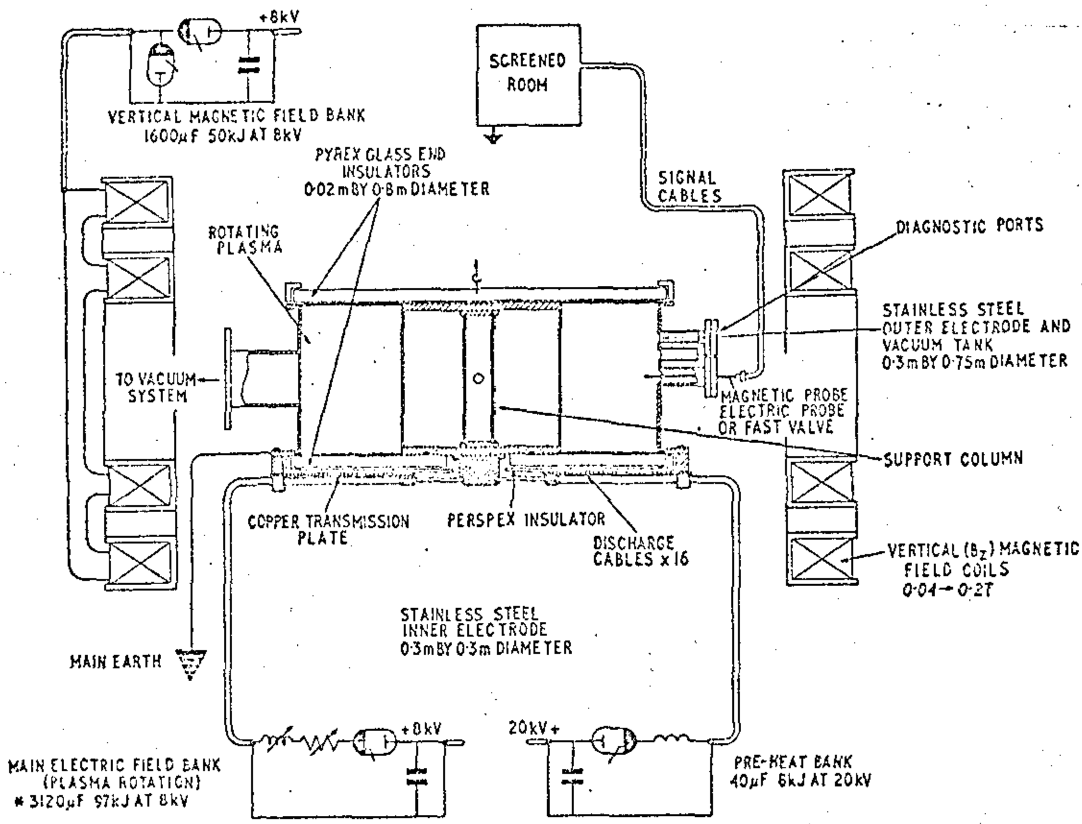

Fig.4.2
Schematic cross sectional view of the VORTEX II device

The electrode system, mounted on aluminium alloy supports, is positioned between four magnetic field coils. The field coil configuration consists of a Helmholtz pair with two additional coils to improve the vertical field uniformity. The optimum coil spacing was calculated using a computer code at Culham giving a B_z field, uniform to within 7% throughout the discharge volume.

In order to prevent the possibility of preferential breakdown at different azimuthal positions, and to therefore reduce the risk of plasma 'spoking' (BARBER et al (1963,1972); LEHNERT (1972)), electrical energy is supplied to the electrodes using 16 uniformly spaced coaxial cables. The inner electrode is the anode and the outer the cathode.

KEY TO FIGURE 4.3

(a) PREHEAT

V 1	8A Variac. 0-270 V
T 1	200 mA 20 kV charging transformer
T 2	RC 74 1:1 pulse transformer
D 1	10 mA 30 kV P I V diode
S1, S2, S4	Copper knife earthing switches
S 3	Early make copper knife earthing switch
R 1	40 × 15 kΩ 2W oil immersed
R 2	500 MΩ Morganite dump
L 1	0.3 μH
C 1	2 × 20 μF 23 kV capacitor bank
S.G.	100 V protective spark gap
V.S.U.	Output to 1737 voltage sensing unit
IG 1	BK 472 ignitron

(b) MAGNETIC FIELD

V 2	8A Variac 0-270 V
T 3	200 mA 8 kV charging transformer
T3, T5	RC 74 1:1 pulse transformers
D 2	100 mA 14 kV P I V diode
S5, S6, S8	Copper knife earthing switches
S 7	Early make copper knife earthing switch
R 4	13.5 kΩ 1000 W
R 5	500 MΩ 25 kV Avo multiplier
R 6	50 Ω 10 MW Morganite dump
R 7	350 Ω 100 W
R 8	1.33 Ω coil resistance
L 2	121 mH coil inductance
C 2	40 × 40 μF 8 kV capacitor bank
IG 2	BK 24 ignitron
IG 3	BK 44 clamp ignitron

(c) RADIAL ELECTRIC FIELD

V 3	8A Variac 0-270 V
T 6	1A 5 kV charging transformer
T 7	RC 74 1:1 pulse transformer
D 3	EHT 1700 B rectifiers
S9, S10, S12	Copper knife earthing switches
S 11	Early make copper knife earthing switch
R 9	6 × 1 k, 200 W resistor
R 10	6 × 1 k, 200 W charging resistor
R 11	500 MΩ 25 kV Avo multiplier
R 12	50 Ω 10 MW Morganite dump
R 13	0 - 250 mΩ
R 14	20 × 1 kΩ
R 15	100 Ω 2 W
L 3	0 - 220 μH
C 3	10 μF 10 kV capacitor
C 4	42 × 78 μF 8 kV capacitor bank
IG 4	BK 24 ignitron

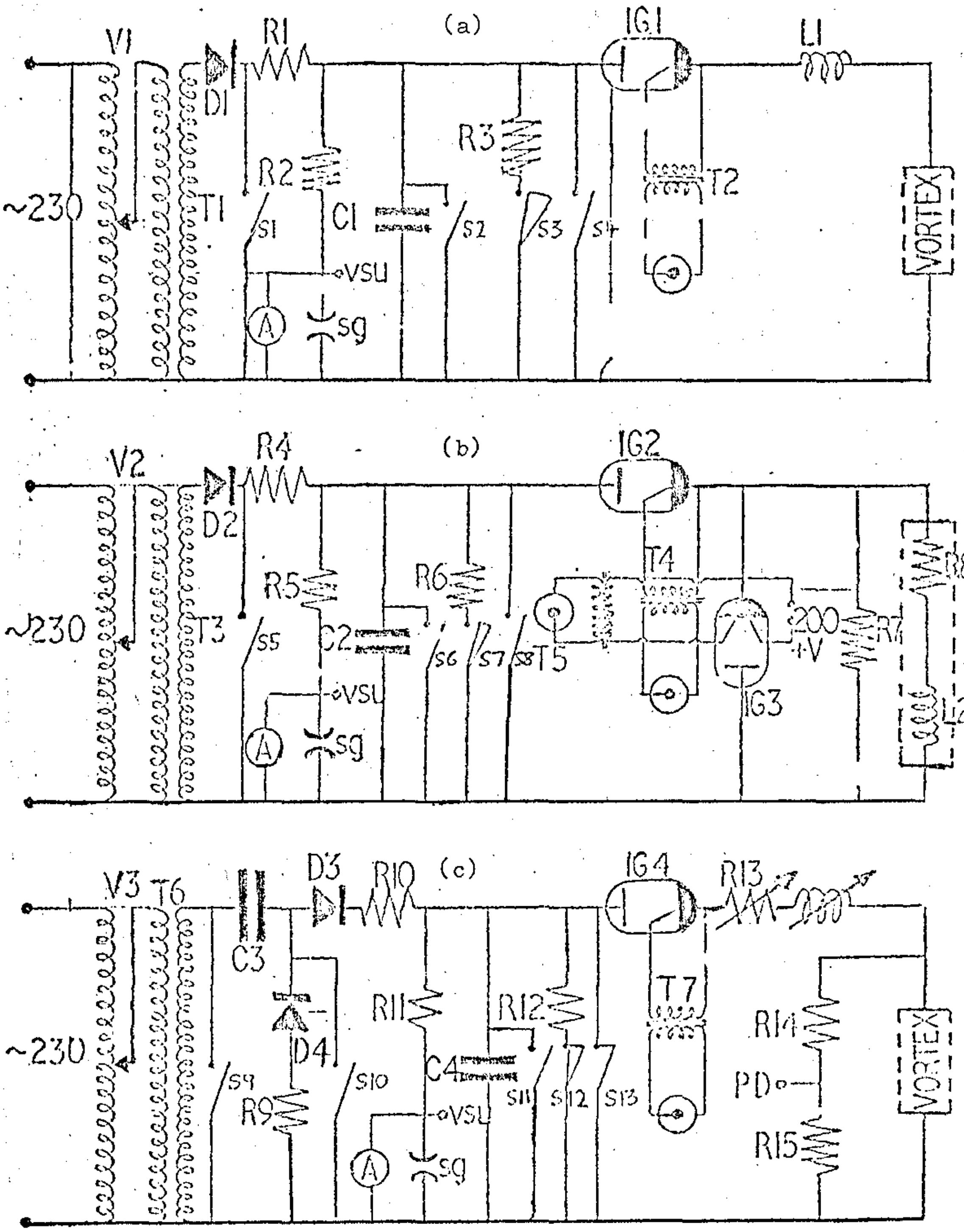

Fig.4.3

Details of (a) the preheat discharge circuit,
(b) the magnetic field circuit, and
(c) the main radial current discharge circuit

4.2 VACUUM SYSTEMS AND GAS SUPPLY

The experimental chamber is evacuated using a 6 inch oil diffusion pump with a liquid nitrogen cooled vapour trap. An oil sealed rotary pump provides a backing pressure of ~ 20 mtorr for the diffusion pump, and is also used to rough the vacuum vessel down from atmosphere. Backing pressure is monitored using a Pirani gauge; a Bayard-Alpert ionization gauge monitors the base pressure of the machine. The pumping system is connected to the machine through a 4 inch diameter glass tube for insulation purposes. A pirani gauge and an absolute McLeod gauge, are connected to the outer electrode to monitor the gas filling pressure.

After evacuation to typically 1×10^{-6} torr, the diffusion pump baffle valve is semi closed to reduce the pumping speed, and gas (normally high purity neon) is leaked into the interelectrode volume using a regulator and a needle valve. The constant flow gas supply is adjusted to give an operating pressure of 50 mtorr .

4.3 MAIN ELECTRICAL CIRCUITS AND POWER SUPPLIES

Electrical energy is supplied to the magnetic fields coils, the preheat and radial electric field discharges by three large capacitor banks which are charged over a three minute operating cycle. The circuits details are shown in Fig.4.3.

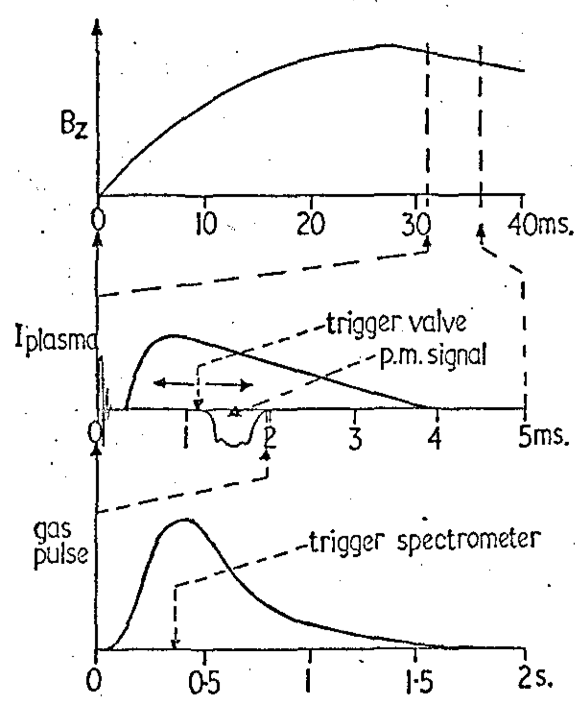

Fig.4.4
Experimental timing sequence of the magnetic field, preheat, main radial discharge and gas sampling system

4.3.1 Magnetic Field

The vertical magnetic field (B_z) circuit, consists of an under-critically damped series L C R circuit. The capacitor bank consists of forty

40 μF. 8 KV capacitors in parallel. The Vortex magnetic field is produced by activating an ignitron which then discharges the stored electrical energy of the capacitor bank, through the field coils. Each of the four field coils is an 80 turn copper cable winding, mounted on plywood formers and escapsulated in epoxy resin. A clamp ignitron is triggered at the first current peak, 27 ms after the start ignitron. Thereafter the coil current decays by resistive dissipation with a time constant of 91 ms. This is much longer than the gas discharge time (typically 3.5 ms) and therefore the field remains essentially constant over this period. The maximum field obtainable with the circuit is 0.2T.

4.3.2 Preheat

The radial preheat discharge (PH), consists of an undercritically damped LCR circuit. The capacitor bank is a parallel combination of two 20 μF, 23 KV capacitors which are normally charged to 10 KV. The capacitor bank is connected to the electrodes by 16 coaxial cables, in parallel, which provide a low impedance circuit.

The oscillating current pulse ($I_{peak} = 120$ kA, $f \approx 50$ kHz) produces both initial gas breakdown (which occurs ~2 μs after the PH ignitron is activated for a gas pressure of ~50 mtorr) and turbulent mixing of the resulting plasma. The result of this is that a reproducible afterglow plasma is produced before the main radial current is applied.

4.3.3 Radial Electric Field Discharge (Plasma Rotation)

The circuit consists of a critically damped LCR series arrangement. The main capacitor bank is a parallel arrangement of forty 78 μF, 8 KV capacitors giving a total stored energy of 97 KJ at maximum charging voltage. The inductance was manufactured using 27 turns of 11 KV cable wound on a 0.23 m radius wooden former, and encapsulated in eposy resin. The coil is tapped along its length such that the inductance can be varied up to 220 mH.

The variable resistor consists of four $62\,m\Omega$ expanded metal resistors connected in series.

The discharge circuit is activated $100\,\mu s$ after the end of the PH discharge, with a current risetime of 0.8 ms , peak current $I_{peak} \approx 8$ KA and total duration some 3.5 ms.

4.4 OPERATIONAL SEQUENCE

The experiment operates on a semi-automatic basis with a three minute cycling time between plasma discharges. During this time the main capacitor banks are charged to a pre-set voltage, determined by the Variac controls on the master control panel, and voltage sensing units. At the end of the cycle, the charging current is stopped automatically by voltage sensing units. A master trigger pulse is then sent to a number of standard 2000 series time delay units connected in series. These delay units then trigger the respective circuits at the correct times. Other delay units are used to trigger diagnostic equipment during the plasma discharge.

The experimental timing sequence, showing typical oscillogram waveforms of the B_z PH and ER discharges, is shown in Fig.4.4.

4.5 SAFETY SYSTEMS

The safety systems are designed to prevent access to any high voltage area during the machine operation, and also to enable rapid dumping of the capacitor banks in the case of an emergency. These consist of door interlock switches, emergency stop switches in the HT areas, and an emergency stop button on the control panel. The activation of any of these switches, or interlocks, automatically causes the capacitor banks to be shorted and earthed. Audible warnings are also provided preceding an experimental discharge.

CHAPTER V

VORTEX II DIAGNOSTICS

The diagnostics used on the Vortex II device can broadly be categorised as; General measurements, which include gas pressure, magnetic field, current and voltage measurements, as well as subjective measurements such as visual inspection of electrode and insulator wear; Plasma measurements, involving spatial and temporal determination of electron temperature, electron density and plasma flow velocity; and finally, Isotopic separation measurements.

With the exception of the fast valve sampling system, used to measure the isotopic enrichment (described in section 4.6), and the CO_2 laser interferometer, described in section 4.7, the experimental measurements have been made using a number of standard diagnostic techniques which are well documented in the literature (see HUDDLESTONE and LEONARD, (1965)). The following sections describe the theory, construction and use of these diagnostics.

5.1 DISCHARGE CURRENT AND VOLTAGE MEASUREMENTS (I_T and V_T)

The interelectrode voltage, V_T, is monitored with a conventional resistive divider circuit, which is shown in Fig.5.1. This circuit was calibrated with a signal generator over the experimental frequency range ($0 < w \leq 10^6$ s^{-1}) and gave $V_T = 412\, V_s$, where V_s is the voltage appearing on the oscilloscope.

Total radial plasma current is measured using a calibrated Rogowskii coil which is positioned around the current input cable of the machine. A passive RC integrating circuit, shown in Fig.5.2, was used to display the current as a function of time on an oscilloscope. Similar Rogowskii coils and integrators were used for the PH and fast valve power circuits. In

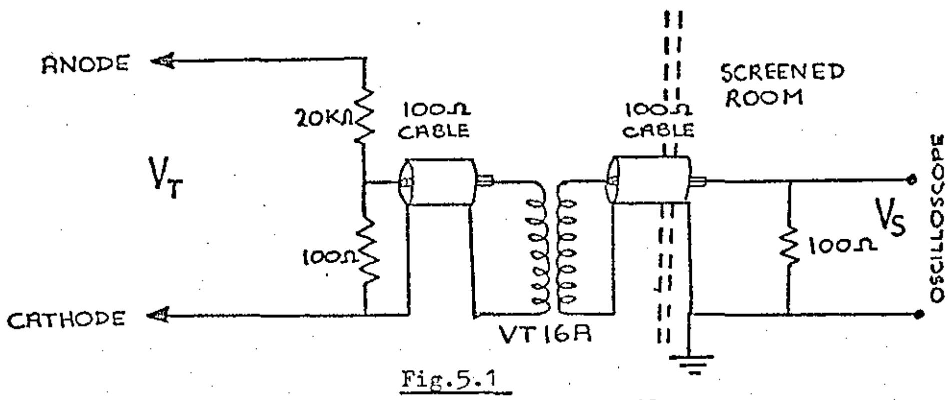

Fig.5.1
Resistive divider circuit details

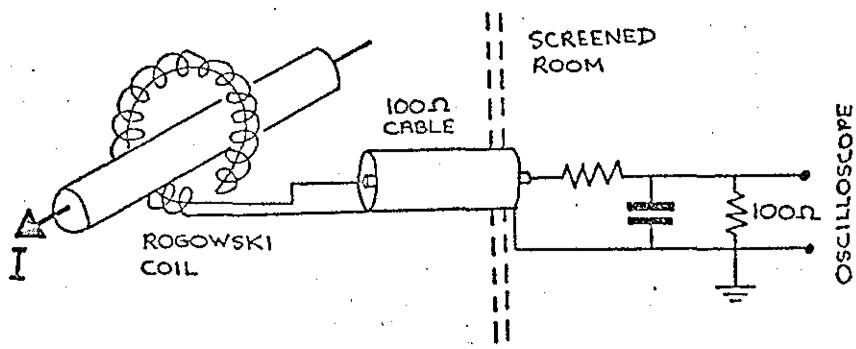

Fig.5.2
Rogowski coil and passive RC integrating circuit

all cases the RC integrating time exceeded the total observation time by at least a factor of $\times 10$, in order to reduce measurement corrections.

5.2 ELECTRODE AND GLASS INSULATOR DAMAGE

Some interesting information can be obtained in a somewhat subjective fashion by visual inspection of discharge damage to the electrodes and to the two glass insulators.

Most electrode wear occurred at the top and bottom of the anode surfaces. In these regions, extending some 1 cm from the ends, the surface layer of the electrode showed evidence of melting, suggesting a high degree of ohmic dissipation, and consequently high current densities in these regions. There was also strong evidence of current tracking damage to the top and bottom glass surfaces, extending approximately 8 cms from the inner electrode (anode). The glass insulator damage was symmetrical around the anode, and similar damage occurred on both glass plates.

The probable cause of the localised electrode and insulator wear (discussed more fully in section (2.3)) is the high current densities which occur at the top and bottom of the discharge when the plasma flow is fully developed. Under these circumstances the boundary resistance is much smaller than the volume resistance of the rotating plasma. This is a common phenomenon in discharges of this geometry, as shown by BAKER et al (1961) and KUNKEL et al (1963). Damage also occurred on the upstream facing surfaces of all the diagnostic probes inserted in the plasma flow.

5.3 MAGNETIC FIELD MEASUREMENTS

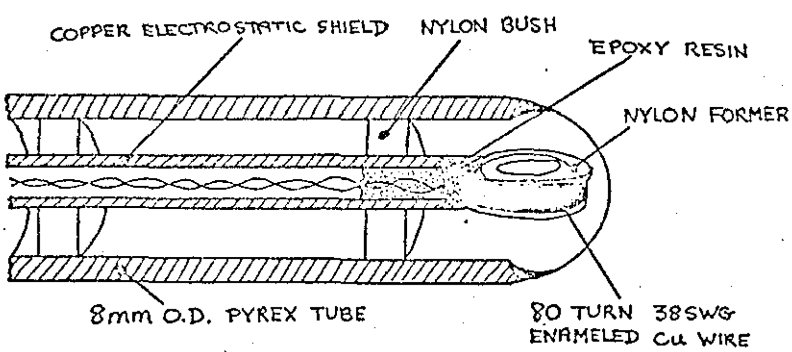

Fig.5.3
Construction details of the magnetic field probe

Measurements of the vacuum interelectrode magnetic field were made using a multiturn search coil, which is shown schematically in Fig.5.3. It consists of an 80 turn enamelled copper winding on a 10 mm diameter former, giving an nA of 7.86×10^{-4} m^2. The output signal from the search coil, V_p, is given by the well-known equation

$$V_p = - nA \frac{dB}{dt} \quad . \qquad \dots (5.1)$$

The resulting signal was displayed on an oscilloscope and integrated graphically to obtain the B_z field.

Spurious pickup was minimised by using twisted enamelled copper connection wires in the magnetic probe, and by screening them with brass tubing. Similar screening was employed with the Langmuir and electric field probes, described in the following sections.

5.4 LANGMUIR PROBES

Floating double Langmuir probes of the type used on the TARANTULA I experiment (PAUL et al (1969)) were used to determine the electron density and temperature in the PH and ER discharges. The probe design is shown in Fig.5.4. Essentially it consists of two planar, equal area, platinum electrodes of 0.5mm diameter, enclosed in a ceramic insulator. Pick-up is suppressed in the same way as with the B_z probe design.

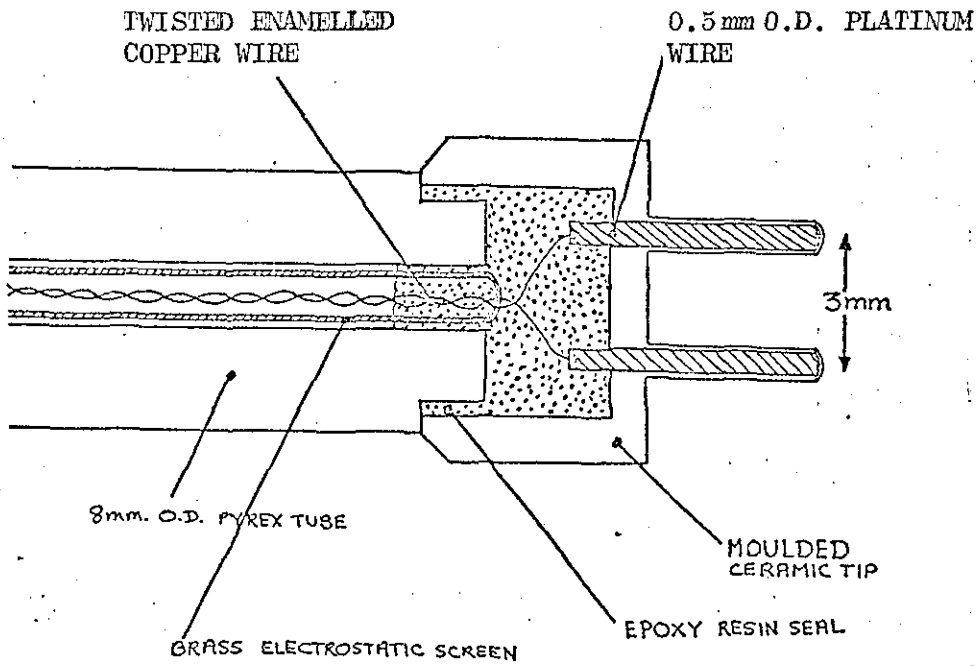

Fig.5.4
Construction details of the Langmuir probe

Langmuir probes suffer from a number of disadvantages. Firstly, the physical presence of the probe in the plasma may affect the plasma; secondly, the probe may be damaged or contaminated in intense discharges, and thirdly, the interpretation of results in the case of highly collisional plasma or plasma in strong magnetic fields, (i.e. where the Hall parameter, $\omega\tau \gg 1$), is very complex. Despite these disadvantages, however, Langmuir probes have been used extensively in plasma physics research. Moreover, the plasma disturbance (which will always be greater than the Debye length, λ_D, due to electric field penetration from the sheath into the plasma), is confined to a region of the order of the probe dimension under many circumstances. The theory is also reducible to a relatively simple form if the probe sheath can be regarded as effectively collisionless. The condition for this to occur can be expressed by the ordering, (CHEN (1964)),

$$\lambda_D < a_e < r_p \leq \lambda_{ei} < a_i ,$$

where λ_D is the Debye length, a_e the electron thermal gyro radius, r_p the probe radius, λ_{ei} the electron-ion mean free path, and a_i the ion thermal gyro radius. This condition holds in both the PH and ER discharges (see section 6.4).

Langmuir probes have an advantage over other diagnostics in that they are relatively easy to use experimentally. They also remain one of the few diagnsotics which can give localised measurements in the plasma (at least in the case of small magnetic fields), since almost all other techniques, such as interferometry or spectroscopy, give information averaged over a large plasma volume.

Since the original theory published by LANGMUIR (1924), the theory of the electric probe in a plasma has been developed extensively, particularly in the collisionless limit (BOHM (1949); BERNSTEIN and RABINOWITZ (1959); ALLEN et al (1957)). Theoretical studies have also been carried out on the effects of a magnetic field on the probe sheath (ALLEN and MAGISTRELLI (1959); SANMARTIN (1970)), and also on the use of probes in plasmas which have a directed flow velocity (SMITH et al (1970); SEGAL et al (1973); VAREY (1970); ALLEN and MAGISTRELLI (1962)). Although in most cases these studies have resulted in rather complicated numerical solutions, experimental evidence of the validity of Bohm's analytic formula for a collisionless probe sheath (given in the next section) has been obtained by CRAIG (1972), using a similar Langmuir probe to that used in the present experiment.

The experimental procedure of determining the electron temperature and density from the probe measurements will now be described.

5.4.1 Measurement Technique

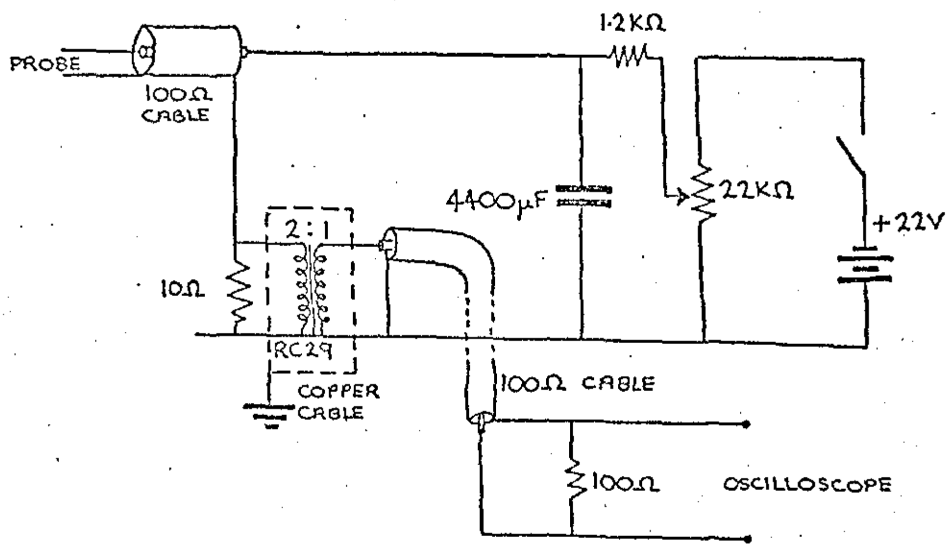

Fig.5.5
Langmuir probe d c measurement circuit

Two circuits have been used to determine the electron density and temperature. The d.c. circuit, shown in Fig.5.5, maintains a constant potential difference between the probe tips throughout the discharge. By varying the voltage from shot-to-shot, the double probe characteristic is obtained from which the temperature can be calculated, using the 'equivalent resistance' method (SCHOTT (1964)) in which the probe voltage interval between the meeting of tangents drawn in the probe characteristic, is equated to $4 \times T_e$ in eV. This method is shown schematically in Fig.5.6. For equal area probes, the electron temperature, T_e, is related to the slope of the probe characteristic, at zero potential difference between the tips, by the expression,

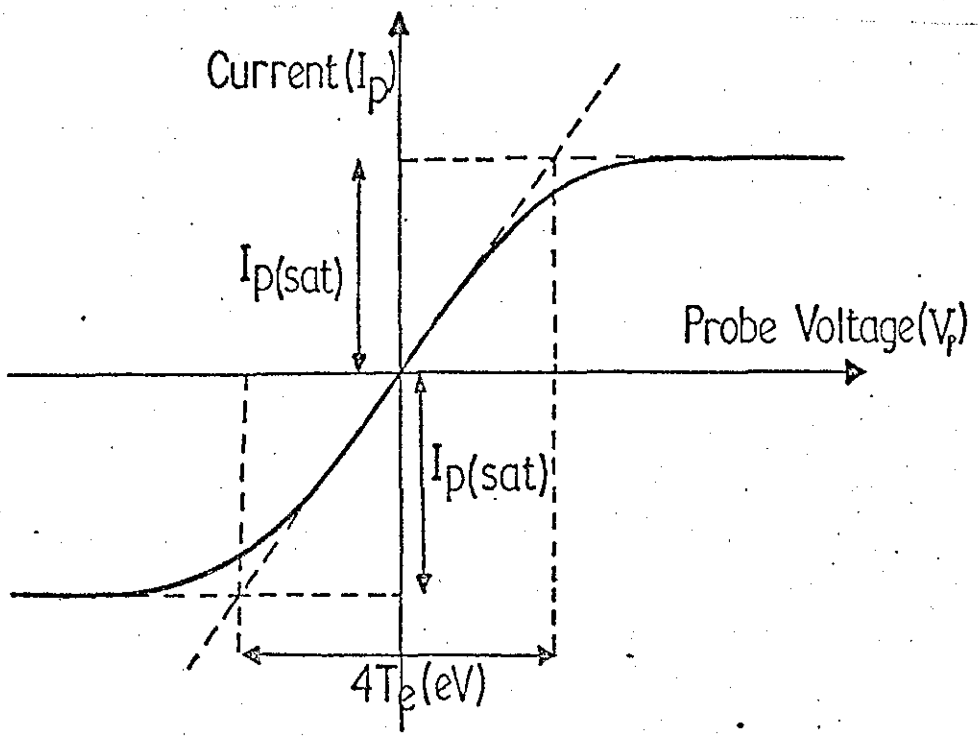

Fig.5.6
Idealized double probe characteristic

$$T_e = \frac{I_{p(sat)}e}{2k}\left(\frac{dV_p}{dI_p}\right)_{V_p=0} \qquad (eV) \qquad \ldots (5.2)$$

where $I_{p(sat)}$ is the ion saturation current. The electron density can then by found from $I_{p(sat)}$ using Bohm's expression

$$n_e = \frac{I_{p(sat)}}{0.4A_p e}\left(\frac{m_i}{2kT_e}\right)^{\frac{1}{2}} \qquad (m^{-3}) \ . \qquad \ldots (5.3)$$

The other cicuit used (Fig.5.7) sweeps the voltage between the probe tips through a preset range, large enough to saturate the ion current to both tips alternatively. The advantage of this technique is that the complete probe characteristic is obtained in one shot. The method is valid provided the sweeping frequency, ω, is much less than the ion plasma frequency, ω_{pi}, (CHEN (1964)). This is always the case in the Vortex plasma since $\omega \sim 2 \times 10^6$, whereas ω_{pi} is typically $\sim 10^{10}$ in the Vortex device. A probe characteristic, taken in the PH afterglow plasma, with the sweep probe, is shown in Fig.5.8. The saturated probe characteristic can be clearly seen.

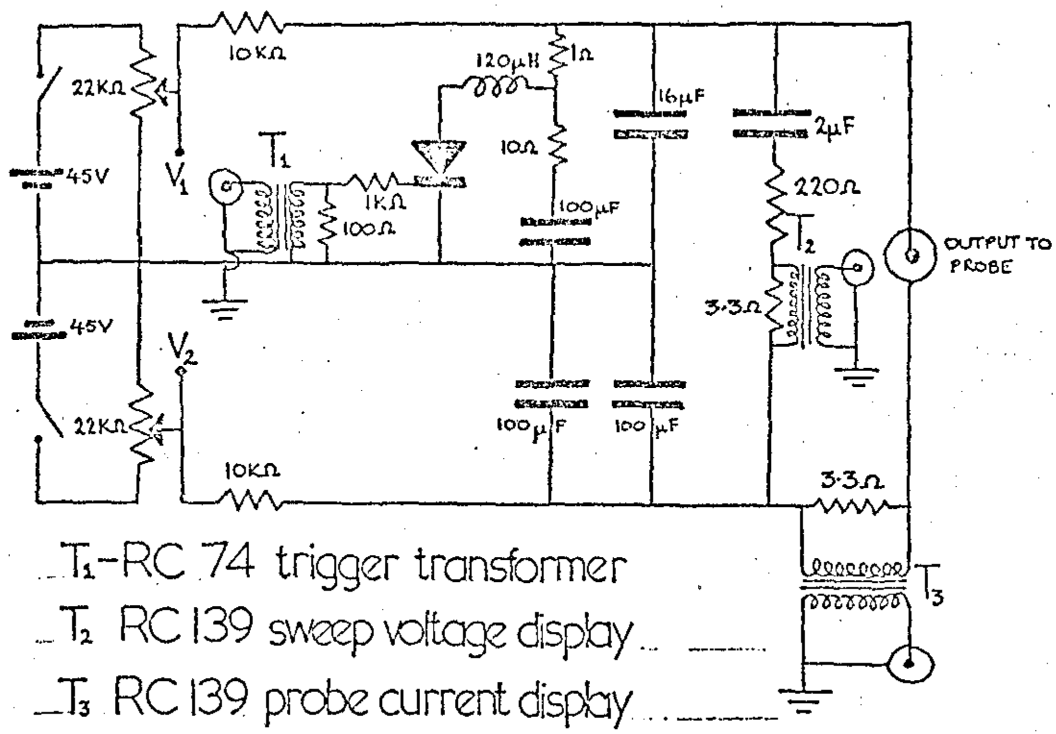

Fig.5.7
Langmuir probe swept measurement circuit

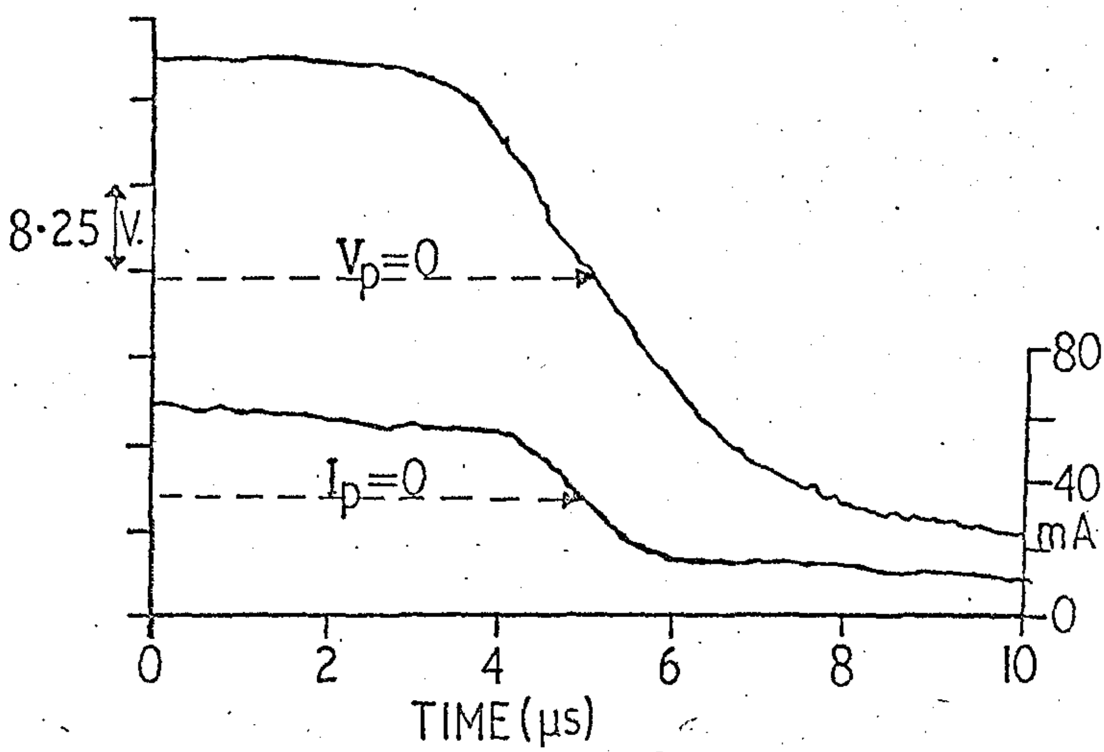

Fig.5.8
Typical raw data from swept Langmuir probe

When taking probe measurements, care was taken to ensure that magnetic field and flow effects were reduced as much as possible, by aligning the tips along the B_z field lines and parallel with the plasma flow (VAREY (1970); NOESKE (1974); SRNKA (1974)). In order to reduce the effect of impurities being present on the probe electrode surfaces, the probe tips were cleaned using a high current between the tips after every four shots, with a simple RC discharge circuit (RUMSBY (1974); SWIFT and SCHWAR (1970)). A further consideration was that the voltage drop across the current measuring transformer/resistor combination (typically ~ 0.1 V), was much less than the inter-tip probe voltage (typically ~ 10 V).

5.4.2 Directed Probe Measurements

As already mentioned in Chapter II, the ions in the Vortex plasma have a net azimuthal drift, whereas the electrons are effectively stationary compared with their thermal velocity. A common technique which utilises this net ion drift as a diagnostic to determine n_e and v_e, incorporates the use of a directed electric probe. This is essentially a planar Langmuir probe, the tips of which can be orientated in any direction relative to the flow.

When the tips are orientated transverse to the ion flow, and normal to the B_z field, the ion motion can be neglected, and the probe tips collect random thermal ions only, in an identical fashion to the Langmuir probe described in the previous section. When the probe tips are directed upstream, the saturated ion current changes from the thermal value to one which includes the effect of the directed ion flux. Calculations by SAGALYN (1963) give this saturated current to be,

$$I_{p(sat)} = \frac{A_p n_e e V_{th}}{2}\left[\exp(-x^2) + \pi^{\frac{1}{2}}\left(x + \frac{1}{2x}\right)\operatorname{erf}(x)\right] \quad \ldots (5.4)$$

where $x = \dfrac{2V_\theta}{V_{th}\pi^{\frac{1}{2}}}$, $V_{th} = \left(\dfrac{8kT}{\pi m_i}\right)^{\frac{1}{2}}$. In the limit as $\dfrac{v_{flow}}{V_{th}} \to 0$, $I_{p(sat)} \longrightarrow A_p n_e e V_{th}$, the current to a stationary probe in a Maxwellian gas (without

Bohm's 0.4 correction). When $V_\theta > V_{th}$, $I_{sat} \rightarrow A_p n_e e V_{flow}$; this is the current to a probe moving with a velocity, V_θ, in a plasma where the random motion of the ions can be neglected (as also shown by VAREY (1970)). In the experimental procedure, the probe was orientated upstream and transverse to the plasma flow. The difference between the saturated ion currents was then equated to,

$$I_{upstream} - I_{transverse} = A_p n_e e V_\theta \,. \qquad \ldots (5.5)$$

This is a reasonable approximation to Sagalyn's formula in the Vortex plasma, and gave good agreement with the values of n_e and V_{flow} calculated independently by other diagnostics (see section 6.6).

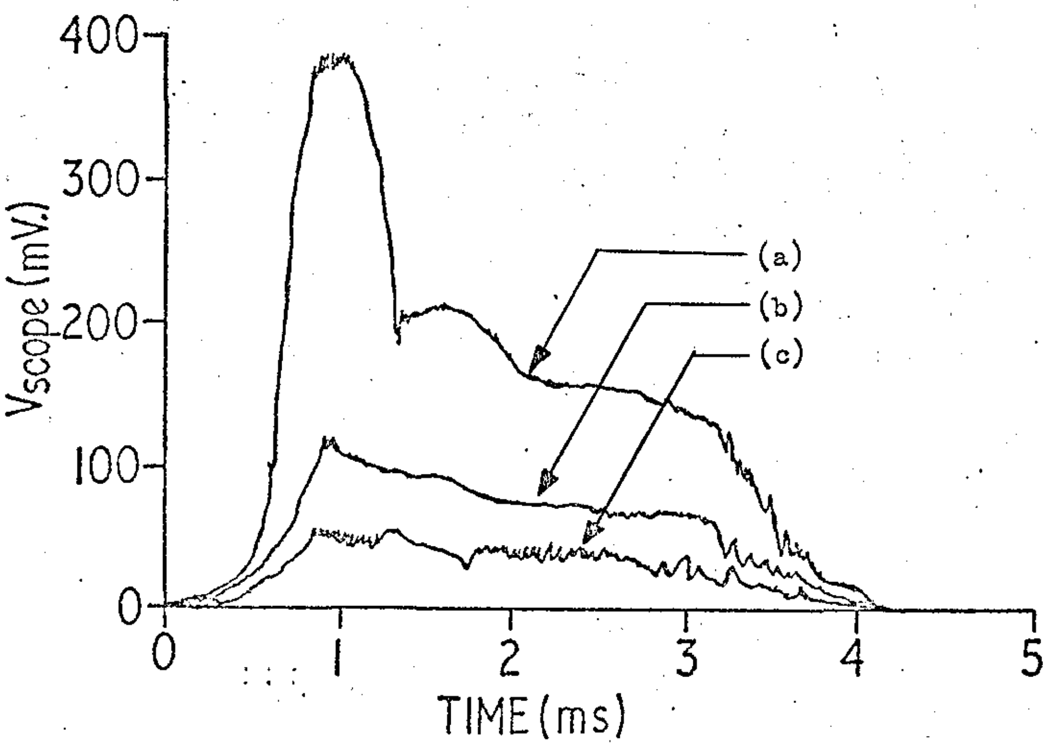

Fig.5.9
Typical raw data from directed Langmuir probe facing (a) upstream; (b) transverse, and (c) downstream in the plasma flow

Typical oscillograms of the saturated ion current to the directed probe for various probe orientation, are shown in Fig.5.9. The effect of the plasma motion when the probe tips are facing the flow is evident.

5.5 ELECTRIC FIELD MEASUREMENTS

A floating, coaxial electrode probe with a high impedance circuit was used to measure the plasma electric field. The probe and circuit are shown in Figs.5.10(a) and (b). Since the electric field is given by

$$E = -\frac{\partial V}{\partial s} \qquad \ldots (5.6)$$

by measuring the voltage difference, ΔV_p, between the coaxial electrodes, the electric field can be calculated from

$$E \approx \frac{\Delta V_p}{d} \qquad \ldots (5.7)$$

where d is the electrode separation. Clearly, as d is made small, equation (5.6) gives a better approximation to equation (5.5). However, the probe signal also reduces and a compromise value of $d = 5$ mm was used in the experiments. The electric probe circuit was calibrated against frequency and gave a signal ratio of $V_p/V_s \sim 8$. Where V_s is the measured oscilloscope voltage.

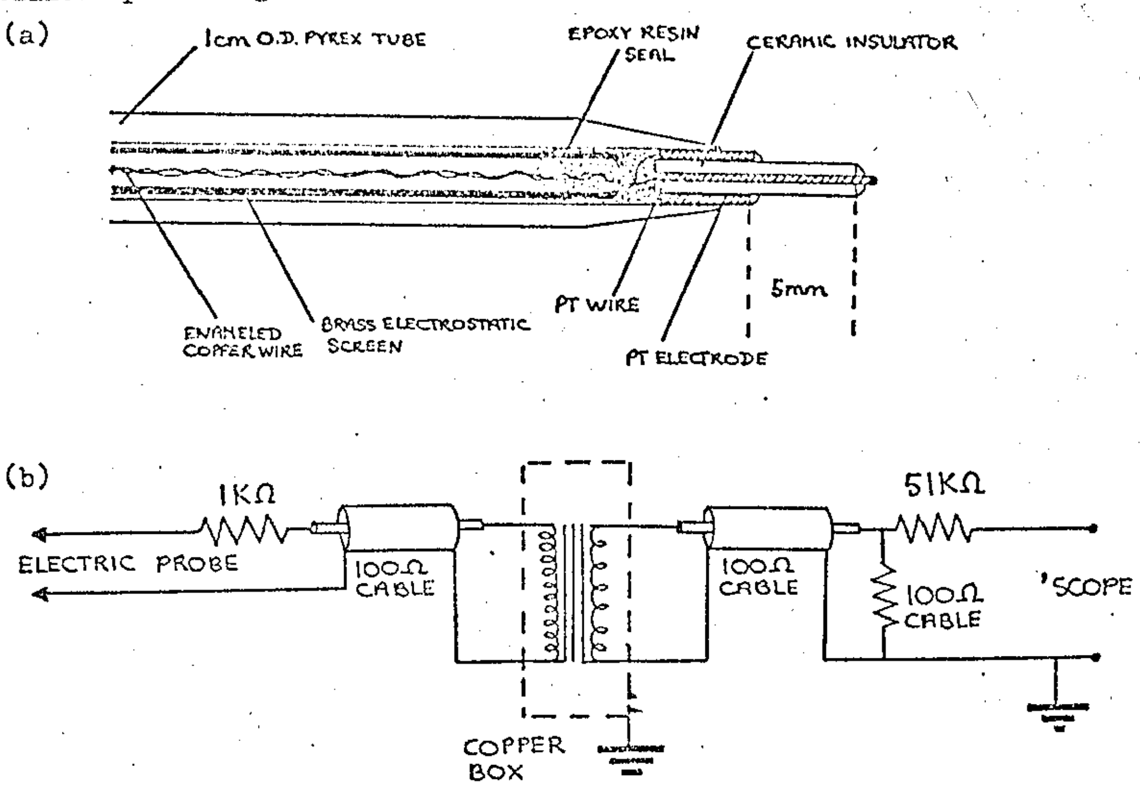

Fig.5.10
(a) Construction details of coaxial electric probe
(b) High impedance electric field measuring circuit

5.6 THE PLASMA SAMPLING SYSTEM

A special problem when considering isotopic separation in a pulsed rotating plasma, is the extraction and mass analysis of ions from the discharge. Spectroscopic observation, although not affecting the plasma, is not practicable since the wavelength difference between isotopes is very small; neon, for example, has an isotopic wavelength shift of only $\sim 6\times10^{-2}$ cm^{-1} (SNAVELY (1974)). Isotopic mass analysis of the plasma ions must therefore entail the physical insertion of a sampling probe into the discharge. Although this undoubtedly affects the plasma, it is the only method available which gives both spatial and time resolved measurements of isotopic enrichment in the plasma.

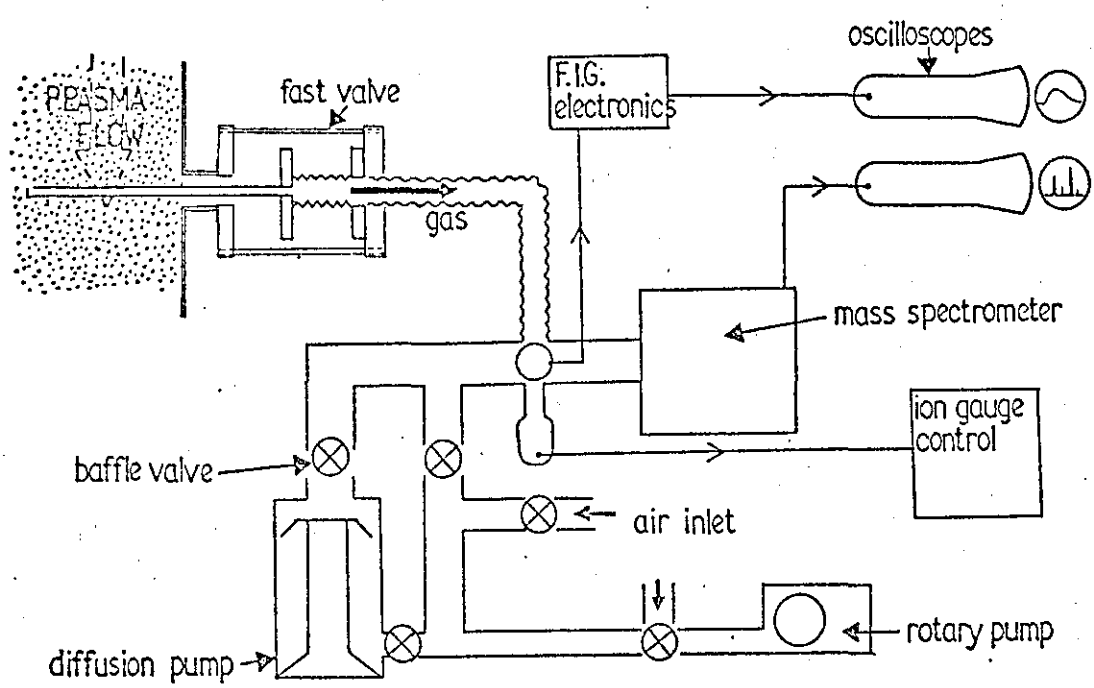

Fig.5.11
Schematic view of plasma sampling system

The complete experimental arrangement of the sampling system is shown in Fig.5.11 (see also Fig.4.1). Essentially it consists of a fast acting valve, moveable in the 'r' and 'z' plane of the discharge, connected by a flexible tube to a fast scanning M S 10 mass spectrometer, and a fast acting ionization gauge. The valve 'floats' at plasma potential and is insulated from the rest of the vacuum system by a glass tube which forms part of the pumping line. The vacuum system has been electro-polished and ultrasonically cleaned; this procedure, together with the use of copper and gold vacuum seals, enables a base pressure of $\sim 2\times10^{-8}$ torr to be attained with a 2 inch diffusion pump and a liquid nitrogen vapour trap.

The sampling system was tested under a number of different operating conditions and gave valve open times ranging from 300 - 980 μs , fast enough to have reasonable time resolution during the plasma rotation (typically ~ 3.5 ms) . Fast ion gauge measurements showed that enough particles are collected with a valve open time of ~ 500 μs , to ensure accurate measurements with the mass spectrometer. The following sections describe the valve in more detail.

5.6.1 The Fast-Acting Valve

(a) Construction details

The mechanical valve, partly based on work by HILL and MONTAGUE (1966), and BURCHAM (1973), is depicted in Fig.5.12. The solenoid circuit details are shown in Fig.5.13.

The valve consists of a stainless steeel tube with a 15° knife edge at one end and attached to an aluminium drive disk at the other end. The knife edge is held against a copper plug of cone semi-angle 80° by a compressed spring, to ensure a good vacuum seal. A stainless steel bellows and sliding 'O' ring seals, allow the aluminium flange axial movement whilst still retaining the vacuum. Two $3\frac{1}{2}$ turn pancake solenoids in SRBF supports are situated a short distance on either side of the flange. A glass sheath covers the valve tube as an insulation from the plasma and to ensure a good vacuum seal with the sliding seals on the Vortex device.

Construction details of fast acting valve.

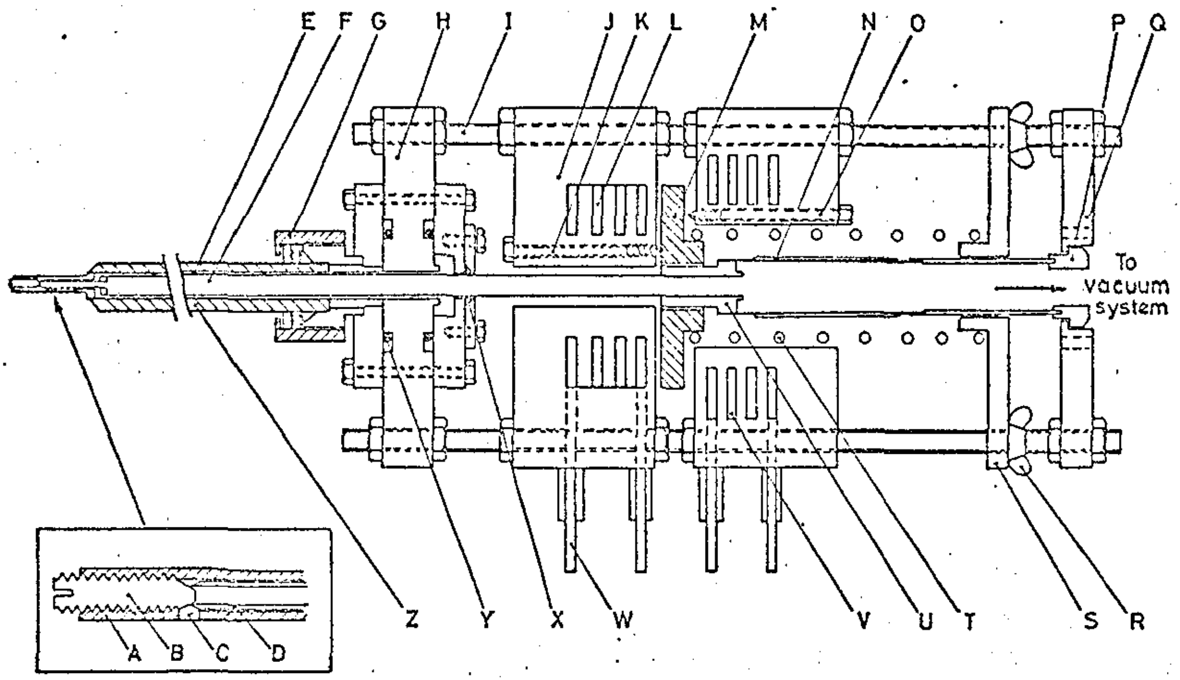

Fig.5.12
Construction details of fast acting valve

KEY FOR FIG.5.12

A Stainless steel tube
O.D. = 5 mm , I.D. = 3 mm , length = 30 mm

B 4 BA screw-in copper sealing plug

C 2 mm diameter valve inlet aperture

D Stainless steel tube
O.D. = 3 mm , I.D. = 2 mm , length = 33 mm

E Stainless steel tube
O.D. = 7.95 mm , SWG = 22 , length = 35.56 cms

F Stainless steel tube
O.D. = 6.35 mm , SWG = 22 , length = 43.18 cms

G Sliding O ring seal and clamp assembly

H Stainless steel flange

I 3 x 6 mm screwed rods

J SRBF solenoid support

K Spring loaded 'break' contact

L $3\frac{1}{2}$ turn Brass pancake solenoid
O.D. = 5.08 cms , I.D. = 2.54 cms

M HE aluminium alloy drive disc
O.D. = 5.08 cms , 0.51 cms thick

N Stainless steel bellows

O Spring loaded 'make' contact

P Stainless steel knife edge flange

Q Stainless steel flange

R 6 mm Butterfly nuts

S Stainless steel spring compressor

T Compression spring

U Stainless steel support boss for aluminium drive disc

V $3\frac{1}{2}$ turn brass pancake solenoid
O.D. = 6.61 cms , I.D. = 4.06 cms

W Coaxial cable connection

X Sliding O ring seal

Y O ring seal

Z Pyrex glass tube. O.D. = 10.8 mm

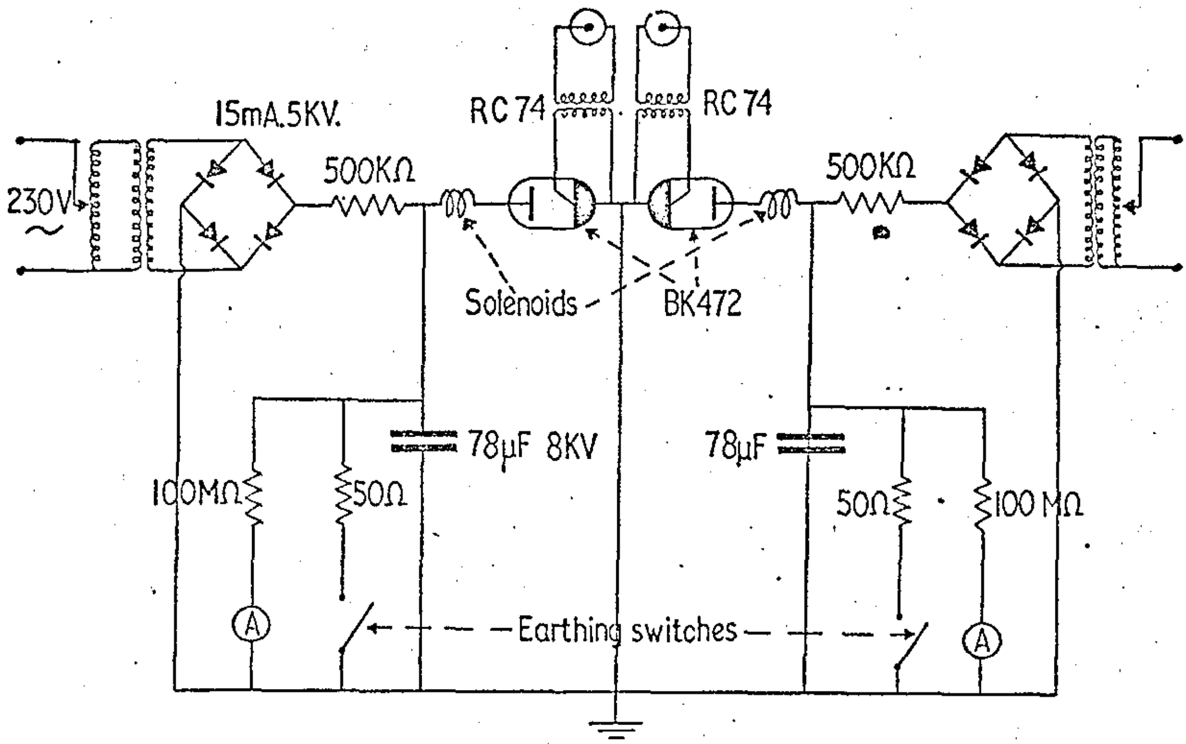

Fig.5.13
Circuit details of fast valve control circuit

The open time of the valve is monitored using a type 9524B , EMI photomultiplier tube, with a -600V power supply to the dynodes. The photomultiplier detects a light signal when the valve opens in the plasma. 'Make' and 'break' spring loaded mechanical contacts were initially used, but were unsatisfactory due to excessive bounce during the valve operation. The photomultiplier, shielded against the machine B_z field by three concentric mild steel tubes, is connected to a glass viewing port at the end of the valve assembly by a flexible fibre optics tube. Experiments performed with a bright light source have shown that a photomultiplier signal is obtained when the knife edge is moved away from the copper plug.

(b) Operation

The valve operates in the following way: when the solenoid is pulsed with a large current of frequency, f, eddy currents are produced in the adjacent aluminium flange, if the flange thickness is greater than the skin-depth, δ, given by,

$$\delta = \left(\frac{1}{\pi f\, \sigma \mu}\right)^{\frac{1}{2}} \qquad \ldots (5.8)$$

where μ is the permeability, and σ the conductivity of the flange. The induced current density, together with the magnetic field, B, produces a force,

$$\underline{F} = \underline{j} \times \underline{B} \qquad \ldots (5.9)$$

which moves the flange away from the solenoid and thus opens the valve at the end of the tube. At the end of the pulse the valve is closed by the compression spring. Firing the other solenoid to speed valve closure, produced only a marginal improvement in valve performance, and consequently only the first solenoid was used in the experimental work.

(c) Valve dynamics

An expression for the valve motion, which is important in the design if high operating speeds are required, can be simply derived if frictional forces are neglected. We then have for the valve motion,

$$F = m \frac{d^2x}{dt^2} + kx \qquad \ldots (5.10)$$

where F is the magnetic force on the flange, k is the spring constant, m is the effective mass of the moving parts, and x is the valve displacement. An expression for the force on the drive disk, derived by NOVAK and PEKAREK (1970), is,

$$F = \left(\frac{\pi \mu}{200}\right) \left(\frac{n R_D}{d}\right)^2 I^2 = C \left(\frac{I}{d}\right)^2 \qquad \ldots (5.11)$$

where R_D is the drive disk radius, n is the number of solenoid turns, I is the solenoid current, d is the distance between solenoid and disc, and C is a constant defined by the equation.

In valves of this type the drive disc displacement during the acceleration period, is small compared with the drive disc/activating coil spacing. The spacing d, can therefore be regarded as a constant, while the current pulse lasts, giving the force as,

$$F = \frac{c}{d^2} I^2_{max} \exp\left(-\frac{2t}{\tau}\sin^2\omega t\right) = F_{max} \exp\left(-\frac{2t}{\tau}\sin^2\omega t\right) \quad \ldots (5.12)$$

where the undercritically damped current relation has been included with $\tau = 2L/R$, and $\omega = (1/LC)^{\frac{1}{2}}$. Combining equations (5.9) to (5.11), and solving for the valve displacement, we get

$$x = \frac{F_{max}\tau}{4m}\left[\left(\exp\left(-\frac{2t}{\tau}\right)-1\right)\frac{\tau}{2}\left(1+\frac{\omega^2\tau^2+1}{(\omega^2\tau^2+1)^2}\right)+\left(1-\frac{1}{1+\omega^2\tau^2}\right)t\right]-\frac{k x_o t^2}{2m}$$

$$\ldots (5.13)$$

where x_o is the initial precompression of the spring. This equation is plotted in Fig.5.14 for two values of the peak force, $F_{max} = 5\times10^3$N, 6×10^3N, and for three values of the spring precompression, $x_o = 5\times10^{-3}$m, 10×10^{-3}m, 15×10^{-3}m. The value of the spring 'k' used in the valve was found experimentally to be 3.2×10^4 N/m, and the effective mass of the moving parts, 95×10^{-3} kg, (drive disc and one third of the spring mass (BOOTH, (1973)). Open times,of the valve, observed for the same spring compressions, are also shown on the graph and suggest that F_{max} is approximately 6×10^3N. This value compares favourably with the value of 7.5×10^3N calculated from equation (5.10), considering the fact that flux leakages between turns have not been taken into account.

Typical oscillograms of the solenoid current and valve open time, obtained from the photomultiplier for the three spring precompressions, are shown in Fig.5.15. They show that there is a lag of approximately 140 μs before the valve opens. Now the velocity of longitudinal waves in this stainless steel tube is 5000 ms^{-1} (KOLSKY (1953)), giving an expected delay of ~86 μs before the valve should open. The discrepancy of ~50 μs could possibly be attributed to the fact that the photomultiplier does not register a signal until the valve is open some 0.01 mm, owing to the 'bedding-in' distance of the stainless steel knife edge/copper seal.

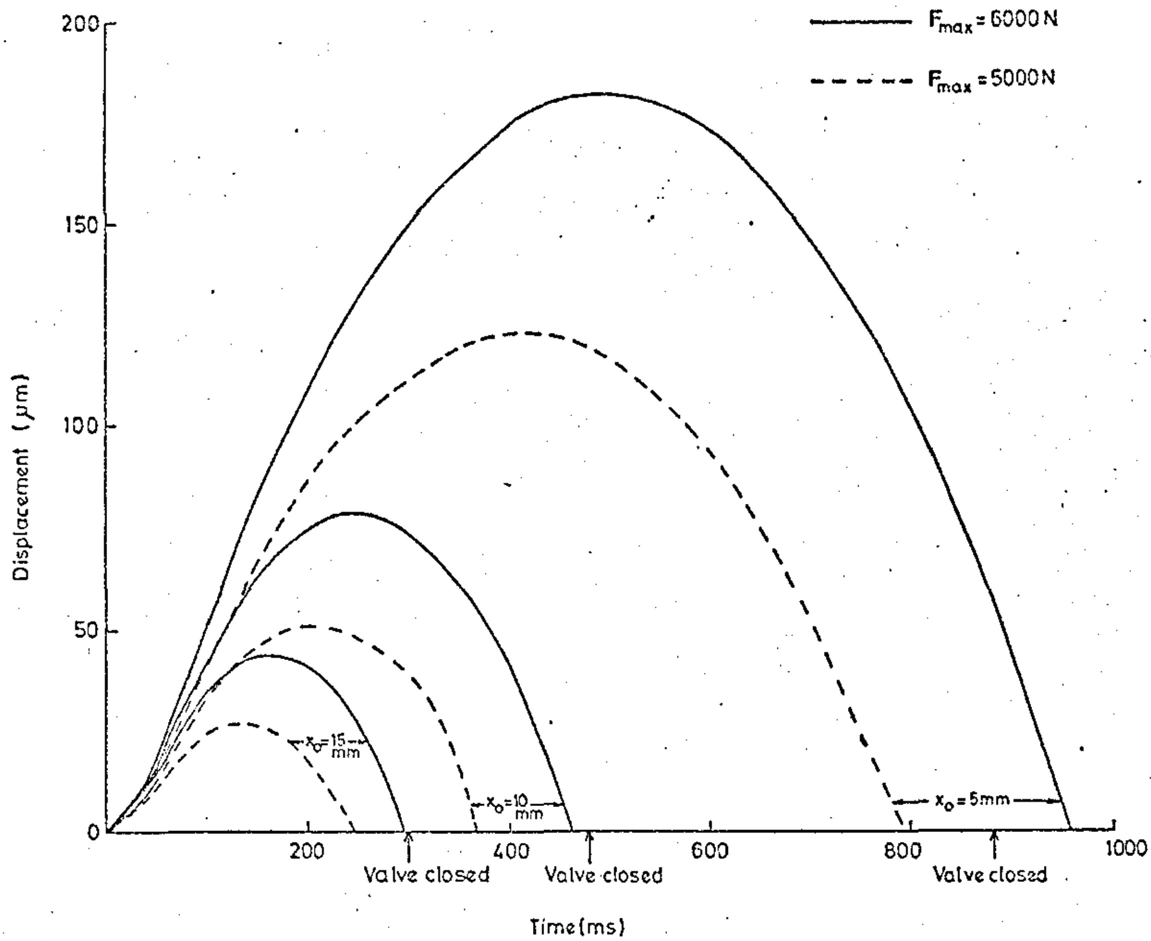

Fig.5.14

Theoretical response of fast valve for various spring compressions and peak magnetic forces

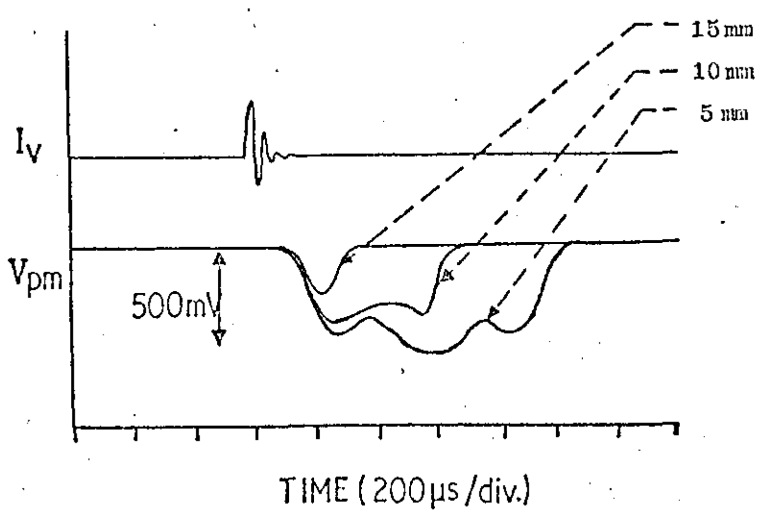

Fig.5.15

Typical oscillogram of solenoid current and photo-multiplier response for various values of spring compression.

5.6.2 The Number of Gas Particles Collected

In the design of the gas analysing system, it is an important consideration to ensure that enough particles are collected to be accurately analysed by the mass spectrometer. This is a function of the inlet pressure for the valve, the valve dynamics, the volume of the analysing chamber, and the statistical fluctuation of the number of particles analysed (see section 5.6.3). Measurements made in the Vortex rotating plasma indicate stagnation pressures of the order 1 – 10 torr, (see sections 5.6.3 and 6.3.6). By assuming a static filling pressure of this magnitude, therefore, the number of particles collected can be calculated from kinetic theory in the following way. The number of particles, Φ, impinging on a unit area per unit time is given by

$$\Phi = \frac{n}{4}\left(\frac{8kT}{\pi m}\right)^{\frac{1}{2}} \qquad \ldots (5.14)$$

for neon at room temperature, this becomes,

$$\Phi = 4.7\times10^{24}\, P_{torr}\ m^{-2}\ s^{-1} \,. \qquad \ldots (5.15)$$

The total number of particles collected is then,

$$N = \Phi D \int_{\text{valve open}}^{\text{valve closed}} x\, dt \qquad \ldots (5.16)$$

where D is the knife edge diameter, and x is given by equation (5.12). This expression has been calculated for the three spring compressions (5 , 10 , 15 mm) with $F_{max} = 6000\,N$. The results of this calculation are shown in Table 5.1. Fast ion gauge measurements (see section 5.6.4) give the total number of particles collected with a spring compression of 10 mm , and a valve inlet pressure of $P \doteq 9$ torr as 1.6×10^{15}, compared with the calculated value of 1.5×10^{15}, so the agreement is very good.

TABLE 5.1

THE NUMBER OF NEON ATOMS COLLECTED AS A FUNCTION OF SPRING COMPRESSION

Spring Precompression (mm)	Valve Closing Time (μs)	Number of Particles Collected
5	980	$10.34\ P_{torr} \times 10^{14}$
10	450	$1.69\ P_{torr} \times 10^{14}$
15	300	$0.56\ P_{torr} \times 10^{14}$

5.6.3 Stagnation Pressure Measurements

As well as analysing the collected gas sample, the fast valve system can be used to determine the amount of gas collected (as described in the previous section) and hence to determine the equivalent pressure of the plasma flow, if a valve calibration against pressure is known. At the end of each experimental run therefore, the machine was filled to a certain pressure with neon and the valve operated. This serves to calibrate the sampling system against pressure. A typical calibration is shown in Fig.5.16.

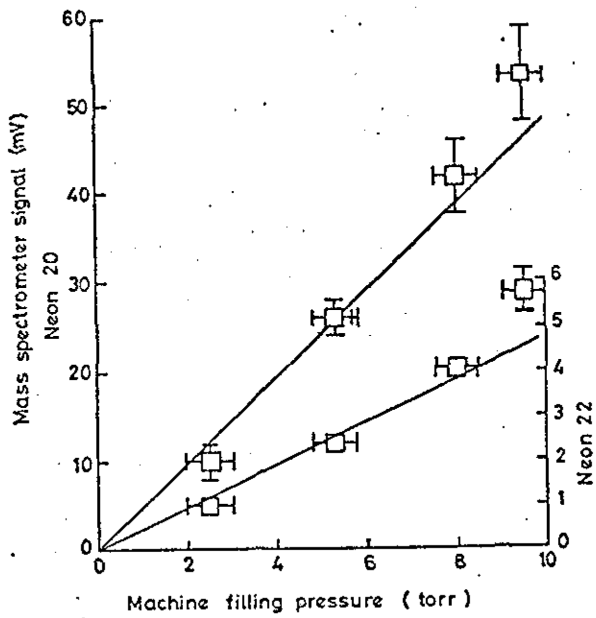

Fig.5.16
Calibration of mass spectrometer signal with machine filling pressure

The rotating plasma stagnation pressure, P_s, is given approximately by BONNEVIER (1971) as

$$P_s = n_i \left(kT_i + \frac{m_i\ v_\theta^2}{2}\right) \mathrm{N\,m^{-2}} \qquad \ldots (5.17)$$

A knowledge of P_s therefore, enables a circular check to be made on T_i,

n_i ($\approx n_e$) and v_θ. This method gave good agreement with the other diagnostics used (see section 6.7).

5.6.4 The Fast Ion Gauge

The gas analysing system is continuously pumped throughout the isotopic enrichment experiments in order to reduce impurity gases and to produce a sufficiently low pressure in the mass spectrometer. A fast ion gauge was therefore constructed to record the time at which the gas pulse from the valve reached the analysing chamber, since normal ionization gauges are limited in response time by their control circuitry.

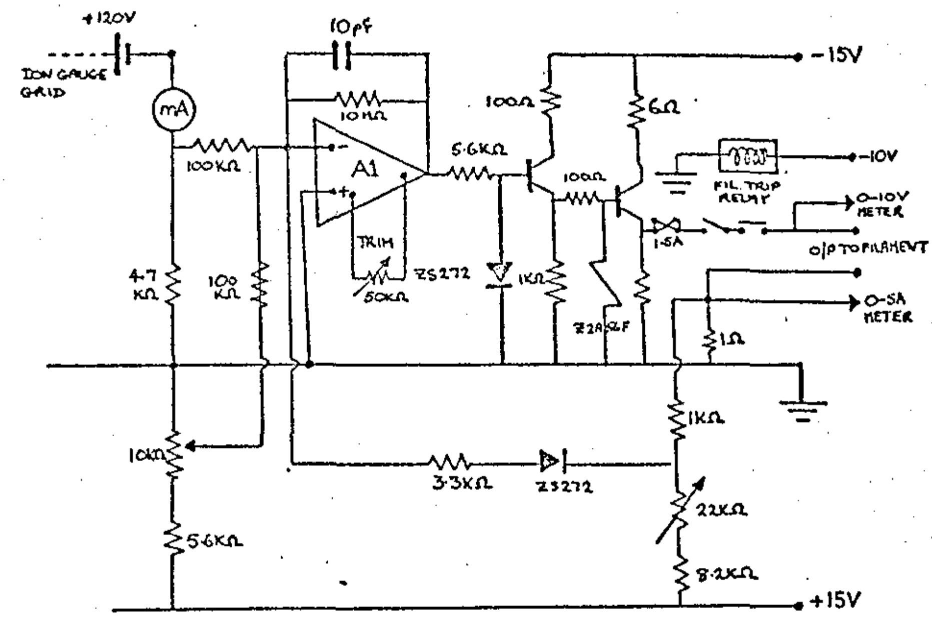

FILAMENT CONTROL UNIT

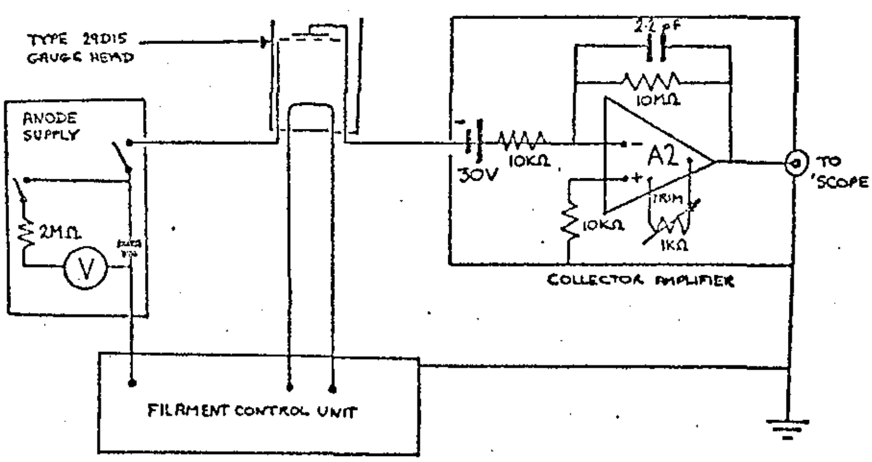

Fig.5.17
Control circuitry for fast ion gauge

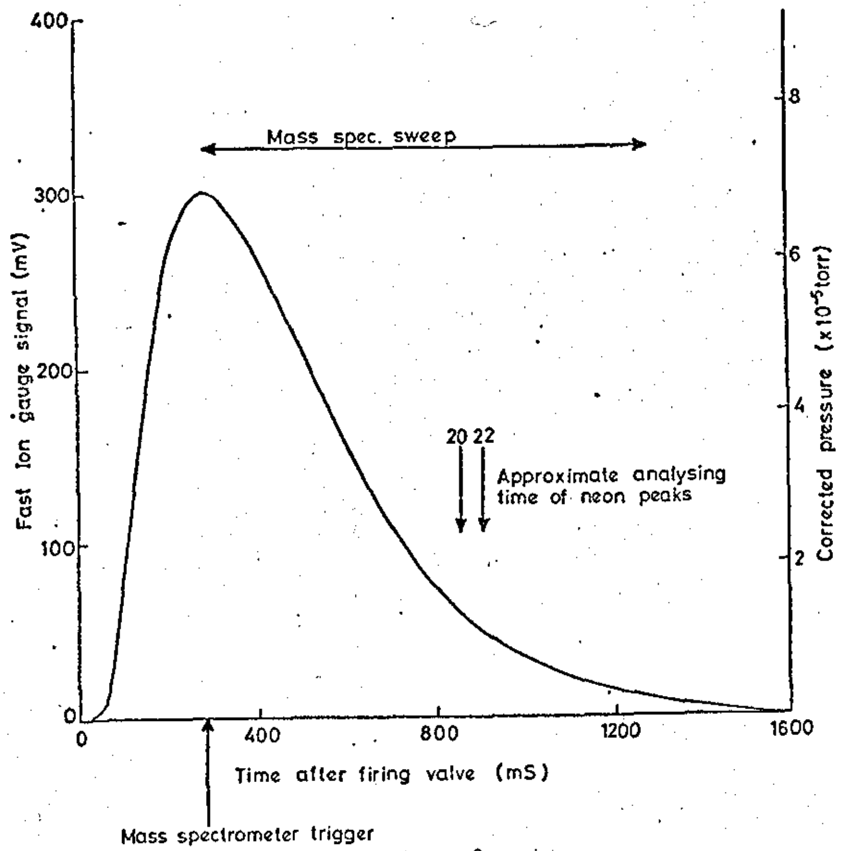

Fig.5.18
Raw data showing the fast ion gauge response

The gauge used is a conventional type 29 B 15 ionization gauge, and the control system is a version of the type constructed by AXON and REID (1968). The complete system is shown in Fig.5.17. Typical operating conditions of the ion gauge are: Filament current = 1.45 A, filament voltage = 4 V, filament emission = 1 mA. An oscillogram trace of the gas flow in the system for a valve spring compression of 10 mm with 9 torr inlet pressure is shown in Fig.5.18. A graphical integration of this trace gives the total number of particles collected to be $\sim 1.6 \times 10^{15}$ (see section 5.6.2).

Further experiments performed with the valve have shown that the gas flow in the system is very reproducible from shot-to-shot, and also that for ~ 1.2 seconds after firing the valve, there is sufficient gas in the system to be analysed accurately with the mass spectrometer. It is important to operate the mass spectrometer when there is no residual B_z

field from the Vortex machine, since any stray fields distort the mass spectrometer electron multiplier tube and the ion trajectories. The mass spectrometer was therefore triggered 280 ms after activating the valve - the machine B_z field is negligible at this time.

5.6.5 The Mass Spectrometer

The mass spectrometer used is a conventional MS 10, 180° ion deflection model with a modification by JEFFERIES (1964) to facilitate fast scans through a preset mass range. The mass spectrometer is capable of scanning from 2 AMU through to 100 AMU in 10^{-1} s, making it ideal for monitoring the relative abundances of various gases in transient flow systems. In all experiments the mass spectrometer was operated under the following conditions; electron beam (ionization) current = 50 μA, electron beam energy = 70 eV, filament current = 3.2 A, electron multiplier voltage = 3 kV, sweep duration = 1 s.

(a) Calibration of the neon isotopes with pressure

As will be seen in section 6.5.2, the stagnation pressure of the plasma varies throughout the discharge volume. A number of experiments were therefore performed to determine whether variations in pressure at the valve inlet produced any systematic errors in the determination of the relative abundances of the neon isotopes. Fig.5.16, used previously to show that the mass spectrometer signal is a linear function of valve inlet pressure, also shows that the neon isotopic abundance ratio is independent of inlet pressure. The average value of $^{22}Ne/^{20}Ne$ obtained, is 9.9% compared with the known value of 9.65%. The discrepancy can possibly be attributed to oscilloscope electronics or to measuring errors.

(b) Statistical fluctuations of the number of collected gas particles

Experiments by JEFFERIES (1964) with the modified MS 10, have shown that the device has a sensitivity of 10^{-5} A/torr at 50 μA electron beam current. The amount of time required to scan each mass peak was also found to be $\sim 5 \times 10^{-3}$ s. From section 5.6.4, we see that a minimum partial pressure of $\sim 10^{-5}$ torr for ^{20}Ne and $\sim 10^{-6}$ torr for ^{22}Ne is obtained in the mass spectrometer for a valve inlet pressure of ~ 1 torr. In this the worst experimental case (see the stagnation pressure measurements in section 6.5.2), the number of ions collected in each mass peak is therefore,

$$^{20}\mathrm{Ne} \; ; \quad N = 5\times10^{-3} \times 6.3\times10^{8} = 3.15\times10^{6}$$

$$^{22}\mathrm{Ne} \; ; \quad N = 3.15\times10^{5} \; .$$

The statistical fluctuation, $\sqrt{N}$, is therefore 0.06% for ^{20}Ne and 0.18% for ^{22}Ne showing that most experimental errors in the determination of isotopic enrichment arise due to measurement errors in the measurement of oscillogram traces or to oscilloscope electronics.

5.7 INTERFEROMETRIC DETERMINATION OF ELECTRON DENSITY

An mentioned in section 5.4, Langmuir probes have a number of disadvantages which result in the fact that measurements made in complicated plasmas, such as in Vortex, may only be order of magnitude estimates. Absolute measurements of the accuracy of Langmuir probes in plasmas, have been made by IRISAWA and JOHN (1973) and by JONES (1974) in theta-pinch devices. In both experiments the probe measurements of T_e and n_e were compared with those obtained by Thompson scattering of high powered CO_2 laser beams from the plasma. Good agreement was found in both cases for the value of T_e. However, Insawa found that the probe n_e measurements were a factor of ~ 4 lower than those given by laser scattering, whereas Jones found good agreement. These experiments show the necessity of obtaining more absolute n_e measurements than those given by probes.

The relative n_e value calculated from probes should, however, be accurate, provided the plasma conditions do not change appreciably throughout the discharge volume. An absolute measurement of the electron density was therefore made using a laser interferometer similar to the type used by ASHBY et al (1964). Although this method gives only the integrated line of sight measurement of n_e, the relative n_e profile is known from probe measurements which can then be calibrated absolutely.

For the Ashby-Jephcott arrangement to give accurate results, the number of interference fringes, N, obtained must be > 1. As we shall show in the next section, N is proportional to the wavelength, λ, of the laser radiation, and to the integrated line-of-sight density, $\int n_e \, d\ell$. Normally, a helium-neon laser, with a wavelength of 0.63 µm, is used in plasmas which have a sufficiently large $\int n_e \, d\ell$ to give $N > 1$. With 0.63 µm radiation, the condition for this to occur is given by:

$$\int n_e \, d\ell > 1.8 \times 10^{21} \text{ m}^{-2} \qquad \ldots (5.18)$$

A special problem encountered with measurements in the Vortex plasma, was that $\int n_e \, d\ell$ (initially obtained from probe measurements) is typically $\sim 10^{20}$ m^{-2} (see section 6.4.1). The system was subsequently modified by using a CO_2 laser with a wavelength of 10.6 µm. The laser was constructed and used in an Ashby-Jephcott arrangement for the first time. This system gave enough fringes to allow accurate values of $\int n_e \, d\ell$ to be determined.

5.7.1 Theory of the Method

Ashby et al have shown that when the output beam from a laser is reflected back into the laser cavity by an external mirror, the laser output intensity is strongly influenced by any phase change in the reflected beam. This phase shifts, $\Delta\varphi$, is determined by the refractive index μ_p of the medium, and the length L_p of the wave path in this medium:

$$\Delta\varphi = \frac{2\pi L_p}{\lambda} (\mu_p - 1) . \qquad \ldots (5.19)$$

The laser intensity therefore, undergoes one cycle of modulation for each complete wavelength change in the optical path between the partially reflecting laser output mirror and the external mirror. The optical path length can be varied by either vibrating the external mirror, or by changing the refractive index of the medium between the two mirrors. It is this second method which allows electron density measurements to be made.

The refractive index of a highly ionized plasma for electromagnetic radiation of frequency $\omega/2\pi$ is given by,

$$\mu = \left(1 - \frac{\omega_{pe}^2}{\omega^2}\right)^{\frac{1}{2}} \qquad \ldots (5.20)$$

where $\omega_{pe} = \left(\frac{n_e e^2}{\epsilon_o m_e}\right)^{\frac{1}{2}}$ is the electron plasma frequency. In the Vortex plasma, $\omega \gg \omega_{pe}$ giving, to a good approximation,

$$\mu \simeq 1 - \tfrac{1}{2}\left(\frac{\omega_{pe}}{\omega}\right)^2 . \qquad \ldots (5.21)$$

Since the number of fringes produced by a plasma of length L_p is,

$$N = \frac{2L_p}{\lambda}(\mu - 1) \qquad \ldots (5.22)$$

we get, combining equations (5.21), (5.22), and inserting the value of the electron plasma frequency,

$$N = \left(\frac{e}{2\pi c}\right)^2 \frac{\lambda}{\epsilon_o m_e} \int n_e \, d L_p$$

$$= 9.4 \times 10^{-21} \int n_e \, d L_p \qquad \ldots (5.23)$$

The number of fringes therefore, gives the integrated line of sight measurement, $\int n_e \, d L_p$, directly.

5.7.2 Experimental Arrangement

A diagram of the laser interferometer system is shown schematically in Fig.5.19. Essentially it consists of a CW CO_2 laser with an external, 80% reflecting, germanium mirror, M3, a totally reflecting mirror, M4, and a Mullard CdHgT_e liquid nitrogen cooled infrared detector. A diverging lens is positioned in front of the detector to reduce the incident radiative power (typically ~1W) in an acceptable level (~10 mW). The laser beam passes radially through the vertical midplane of the machine through two anti reflection coated germanium windows. The external mirror, M4, is used to allow the detector to be positioned some 5 m away from the

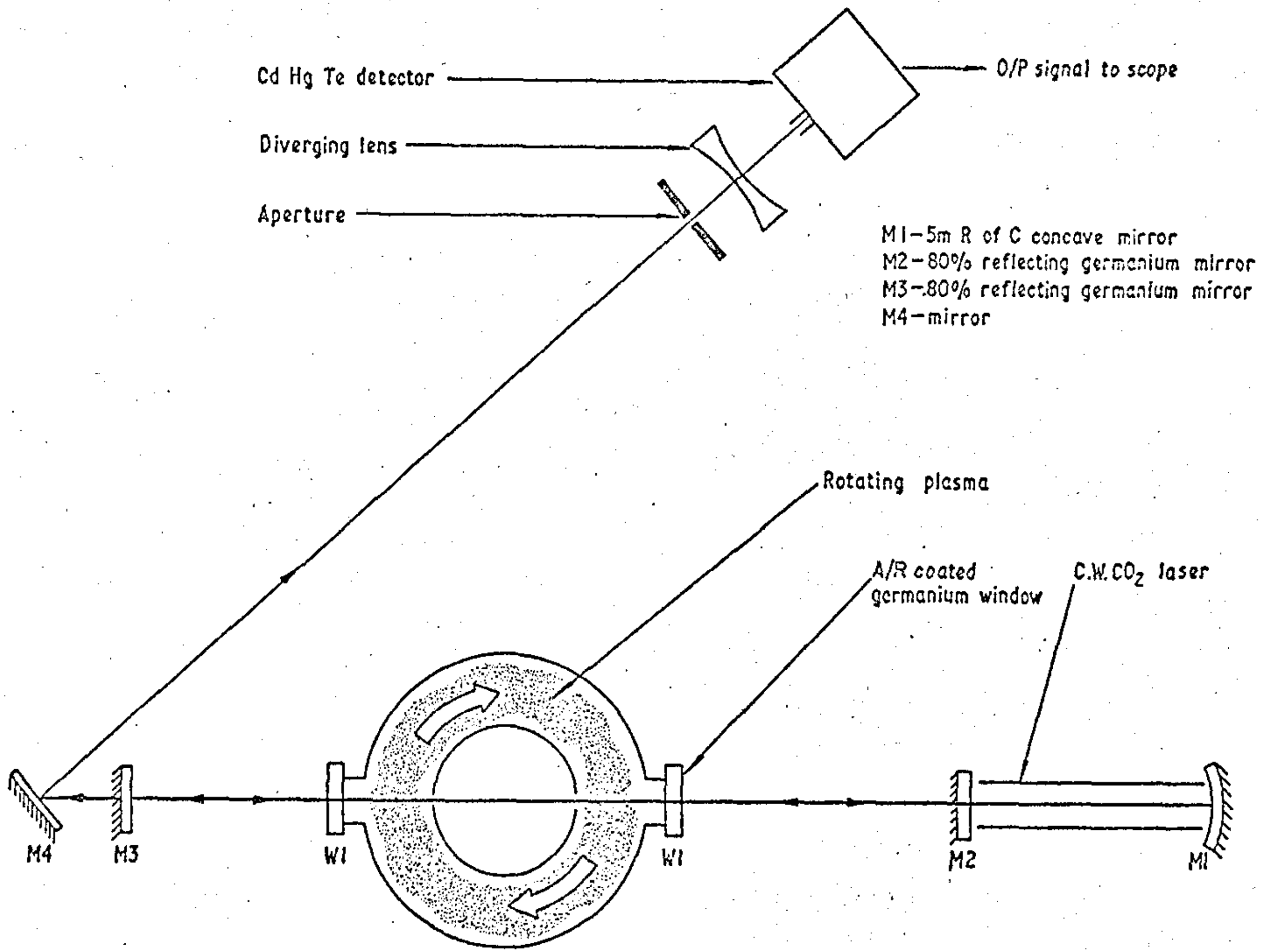

Fig.5.19
Schematic view of the laser interferometer set-up

the discharge (the maximum distance possible in the experimental area). This reduces stray pick-up from the discharge to a minimum. Interference is also reduced by enclosing the detector in a copper box.

The laser, shown in more detail in Fig.5.20, consists of a glass tube of 1 m length and 20 mm diameter, on which are mounted two electrodes positioned 0.56 m apart. The cathode and the laser tube are water cooled. A gold plated concave mirror of radius of curvature 5 m and an 80% reflect- planar germanium mirror, are mounted at both ends of the tube on flexible rubber connections a distance 1.07 apart (~ 0.25 m from the discharge, in order to prevent mirror surface damage). Mirror adjustment is made using two micrometer screws and a flexible support. The design considerations of the laser will now be briefly discussed.

Calculations by KOGELNIK and LI (1966) show that a concave/planar mirror arrangement of the type used here is stable if,

$$0 < \left(1 - \frac{L}{R}\right) < 1 \qquad \ldots (5.24)$$

where L is the mirror spacing, and R is the radius of curvature of the concave mirror. The beam radius, r_0, at the output mirror, defined as the distance at which the amplitude is 1/e times that on the axis, and the beam divergences, θ, are also given by,

$$r_0 = \left(\frac{\lambda^2}{4\pi^2} L(2R - L)\right)^{\frac{1}{4}} \qquad \ldots (5.25)$$

$$\theta = \frac{\lambda}{\pi r_0} \qquad \ldots (5.26)$$

Giving $r_0 = 2.3$ mm and $\theta = 1.48 \times 10^{-3}$ radians for this particular laser cavity.

The laser tube is evacuated by a rotary pump and gas is continuously leaked into the system using a needle valve and a two-stage regulator. The gas used comprises of a pre-mixed quantity of 70% N_2, 20% He, and 10% CO_2. The two additive gases (N_2 and He) produce a far greater operating efficiency than that obtained using pure CO_2, as discussed by DEMARIA (1973).

C.W. CO_2 Laser - Schematic

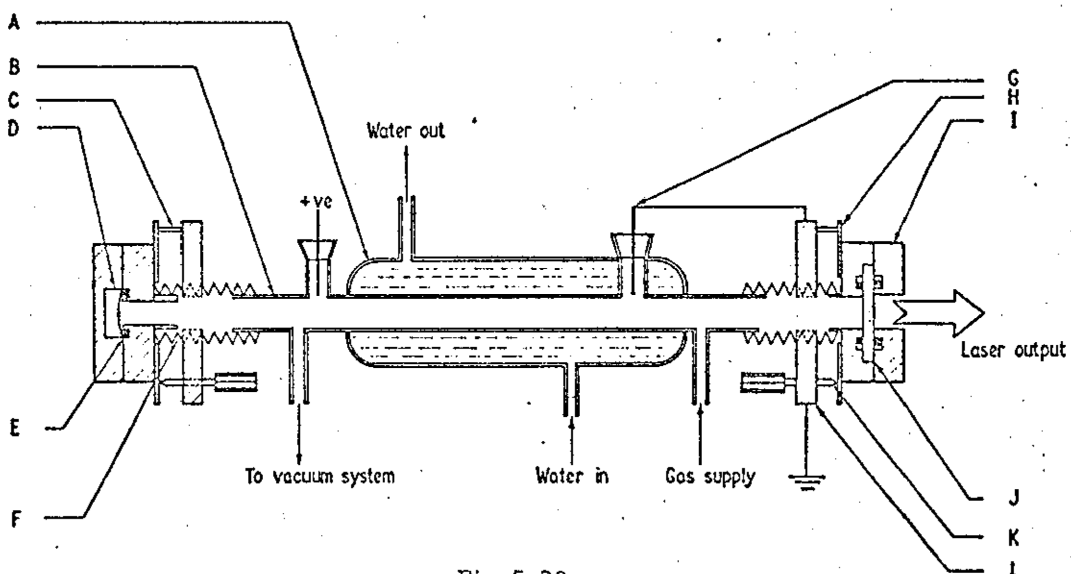

Fig.5.20
Schematic view of the CO_2 laser

KEY TO FIGURE 5.20

A. Water Jacket

B. Laser tube; 1 m long, 0.02 m o/d

C. Flexible steel bolt (4BA)

D. Totally reflecting mirror, radius of curvature = 5 m, o/d = 0.025 m

E. 'O' ring seals

F. Flexible bellows

G. Water cooled cathode

H. Aluminium support plate

I. Perspex flange, o/d = 0.08 m

J. Partially reflecting germanium mirror (R ≈ 80%)

K. Micrometer for mirror alignment

L. Aluminium support plate; 0.13 m × 0.10m.

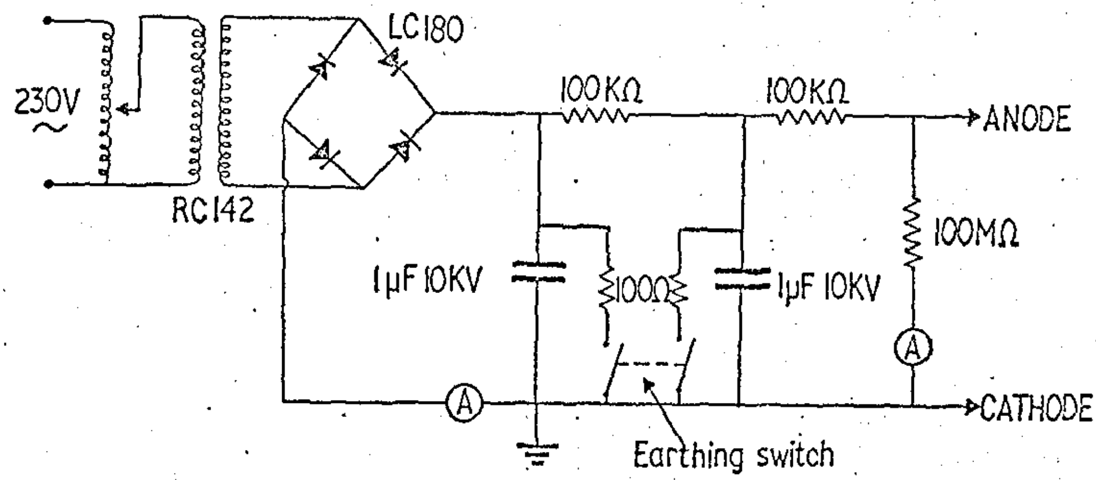

Fig.5.21
Laser power supply schematic

The laser power supply is shown in Fig.5.21. It gives a well smoothed supply of ~ 6 mA at 4.8 kV to the electrodes, with a tube pressure of 8 torr. The laser efficiency was found to be $\sim 8\%$ with these operating conditions giving a measured output power of ~ 2.3 W in the fundamental (TEM 00) mode.

5.8 ERROR ANALYSIS

All measurements, other than gas filling pressure, were made by recording oscillograms on polaroid film. The appropriate signal was then measured with a finely ruled scale. Systematic errors were minimised by calibrating the various diagnostics as shown previously.

The main source of error appeared as random shot-to-shot fluctuations in the plasma and the sampling system. Consequently a number of measurements were made at each condition; a minimum of four shots for the probe measurements and a minimum of ten shots for the laser interferometry and mass analysis measurements. Each data point shown in this thesis is comprised of the calculated mean value, x_0, and the error bars shown are ± one standard deviation, δ, defined by

$$\delta = \sqrt{\frac{\Sigma(x - x_0)^2}{n - 1}} \qquad \ldots (5.27)$$

The experimental results obtained with the diagnostics are presented in the next chapter.

CHAPTER VI

EXPERIMENTAL RESULTS

The experimental programme undertaken on the Vortex II plasma, progressed through two main stages. The first part of the experimentation was concerned with the basic discharge characteristics and a detailed analysis of the plasma dynamics. This enabled the discharge conditions for maximum plasma density, flow velocity and stability, to be found. The optimum conditions were, $V_{ER} = 8\,KV$ (i.e. maximum discharge energy) and $B_z \geq 0.1\,T$. In the second phase of the experimental programme, the phenomenon of isotopic separation was studied. As a complete parametric analysis of the dependence of isotopic enrichment on discharge conditions was considered outside the scope of this thesis, only two main operating conditions were studied in detail. These were $V_{ER} = 8\,KV$ with $B_z = 0.1\,T$ and $B_z = 0.2\,T$.

A description of the plasma dynamics and isotopic enrichment, using the neon isotopes, is presented in this chapter. In general, they are strongly dependent on time, the two space coordinates (r,z), and on the initial conditions p_0, B_z and J_R.

6.1 PREHEAT CHARACTERISTICS

A typical oscillogram trace of the preheat current and voltage in neon with a machine filling pressure of 50 mtorr, $B_z = 0.1\,T$ and $V_{ph} = 10\,KV$ is shown in Fig.6.1. A voltage of about 2.4 KV develops across the electrodes after the preheat ignitron is fired, and breakdown occurs typically 1.4 μs later. Thereafter, the current and tube voltage decay to zero in an undercritically damped fashion after 120 μs, primarily due to the impedance of the external discharge circuit. Tube voltage reverses sign with the current implying that the azimuthal plasma velocity also changes sign with the oscillatory current pulse. This leads to turbulent mixing and a

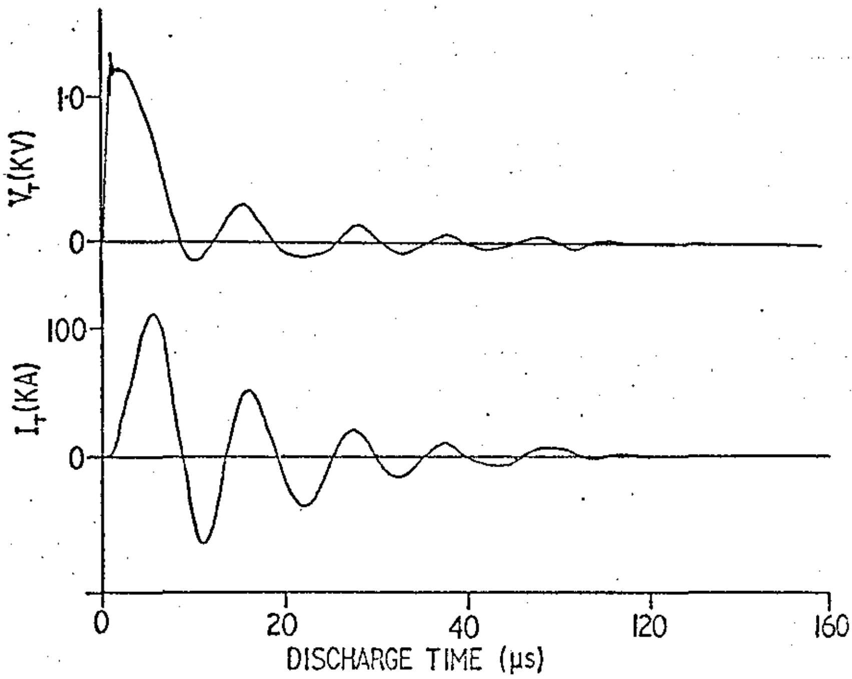

Fig.6.1
Typical oscillograms of the pre-heat current and voltage waveforms

uniform afterglow plasma is produced. The magnitudes of the plasma current and voltage were found to be insensitive to the machine filling pressure over the range $p_o = 10 - 200$ mtorr.

Measurements were made of the electron density, n_e, and temperature, T_e, at the end of the PH pulse, using dc and swept Langmuir probes. The calculated values of n_e and T_e obtained by the two methods agreed to within 20%. Fig.6.2 shows the probe characteristic obtained with the Langmuir probe and dc circuit, 100 μs after the end of the PH pulse in neon, with $B_z = 0.1\,T$. Using the equivalent resistance method (see section 5.4.2) this gives $T_e \approx 2.25$ eV with $n_e \approx 1.6 \times 10^{20}$ m^{-3}. Radial profiles of T_e and n_e taken at the same time with the swept Langmuir probe

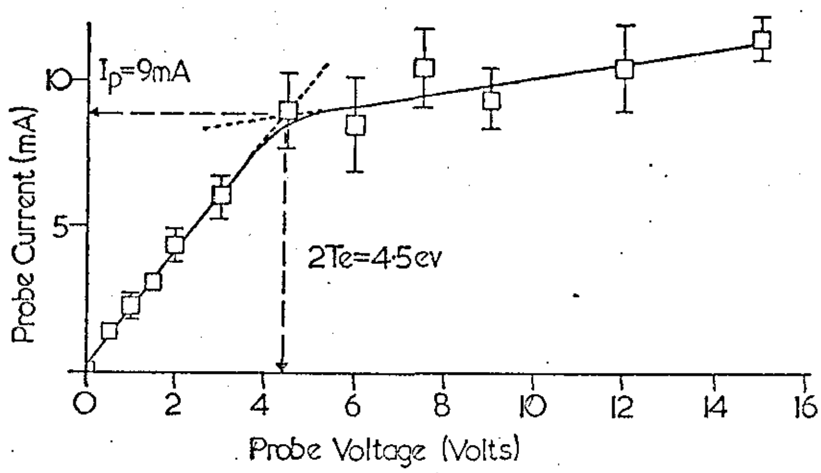

Fig.6.2
Langmuir probe characteristic during the pre-heat afterglow

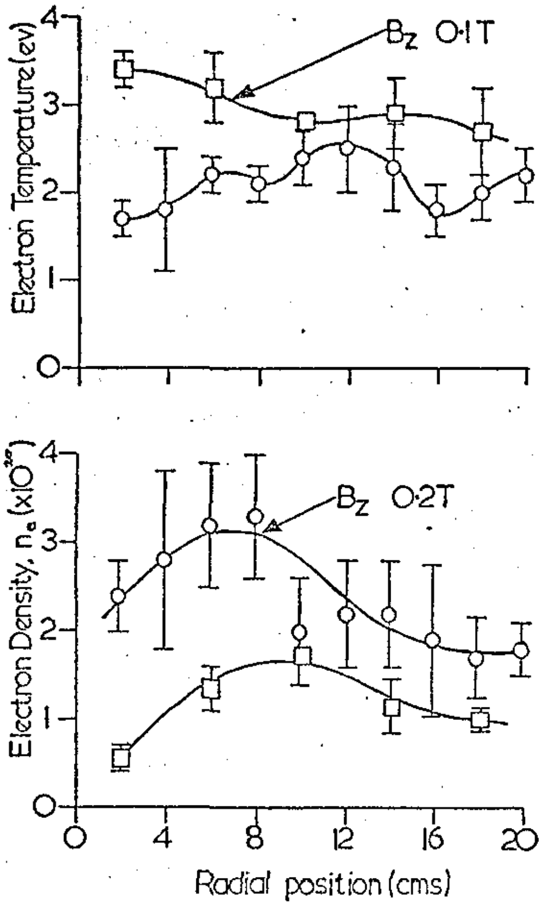

Fig.6.3
Swept probe measurements of the radial profiles of T_e and n_e in the pre-heat afterglow

(Fig.6.3) show good agreement with the d c probe measurements. For $B_z = 0.1\,T$ the swept method gives $T_e \approx 2.8\,eV$ and $n_e \approx 1.75 \times 10^{20}\,m^{-3}$. Integration of the radial density traces, assuming vertical uniformity, shows that the plasma density corresponds to 7% of the initial neutral gas ionized with $B_z = 0.1\,T$, and 14% with $B_z = 0.2\,T$. Most of the neutrals will have free streamed to the outer radii and to the end insulators, although some will still be present in the main plasma body. These neutrals may be responsible for the current spoking which occurs in the acceleration phase of the plasma, when the main E_R bank is applied (see section 6.3). The outward centrifuging of the neutral and plasma losses to the walls, contribute to the shape of the density profiles shown in Fig.6.3. The high values of T_e and n_e obtained at the outer electrode surface ($r = 20$ cms) are attributed to the fact that the diagnostic port has a diameter of 2.5 cms , making both T_e and n_e higher than they are at other azimuthal positions.

These probe measurements indicate that a reproducible afterglow plasma is produced 100 μs after the end of the PH pulse. This time was therefore chosen as the starting time of the main radial (E_R) discharge.

6.2 TUBE CURRENT AND VOLTAGE MEASUREMENTS

The current/voltage characteristics of the Vortex discharge, exhibit complex behaviour. The tube voltage is dependent on the magnetic field, the machine filling pressure, the radial current and also on two-dimensional and time dependent phenomena in the discharge. The radial current is governed primarily by the external circuit parameters and is only slightly affected by p_0 and B_z (increasing with p_0 and decreasing with B_z).

A set of oscillograms obtained with $B_z = 0.1\,T$, $p_0 = 50\,\text{mtorr}$ with varying levels of peak current, is shown in Fig.6.4. These may be interpreted in terms of the simple model for the interelectrode voltage, V_T, discussed in section 2.2. For peak currents of 4 KA and less (Figs.6.4 (a) and (b)), which we shall call the low current regime, the input power is insufficient to completely ionize the gas in the main plasma volume. There will, therefore, be neutrals in the plasma volume and the critical velocity effect will be expected to occur. This will give rise to a voltage limitation across the device. The voltage limitation calculated from equation (2.25) is sketched in Fig.6.4(b) and indicates the critical velocity phenomena present in Vortex for low current inputs. Closer inspection of Fig.6.4(b) shows that after the E_R bank is triggered at $t = T_1$, the voltage rises to the critical voltage (plasma acceleration phase), and remains reasonably constant from $t = T_2$ to $t = T_3$. Thereafter the input power is insufficient to offset viscous drag and other plasma loss processes, and the voltage decays until at $t = T_4$, the plasma balance breaks down and the plasma enters a lowly ionized mode with a corresponding rise in the tube voltage. A similar effect is seen in Fig.6.4(c).

At higher current inputs ($I_p > 4\,\text{KA}$), the tube voltage exceeds the critical voltage by approximately a factor of 3, rising to a value of 800 V during the acceleration phase, as shown in Figs.6.4(c) and (d). At peak

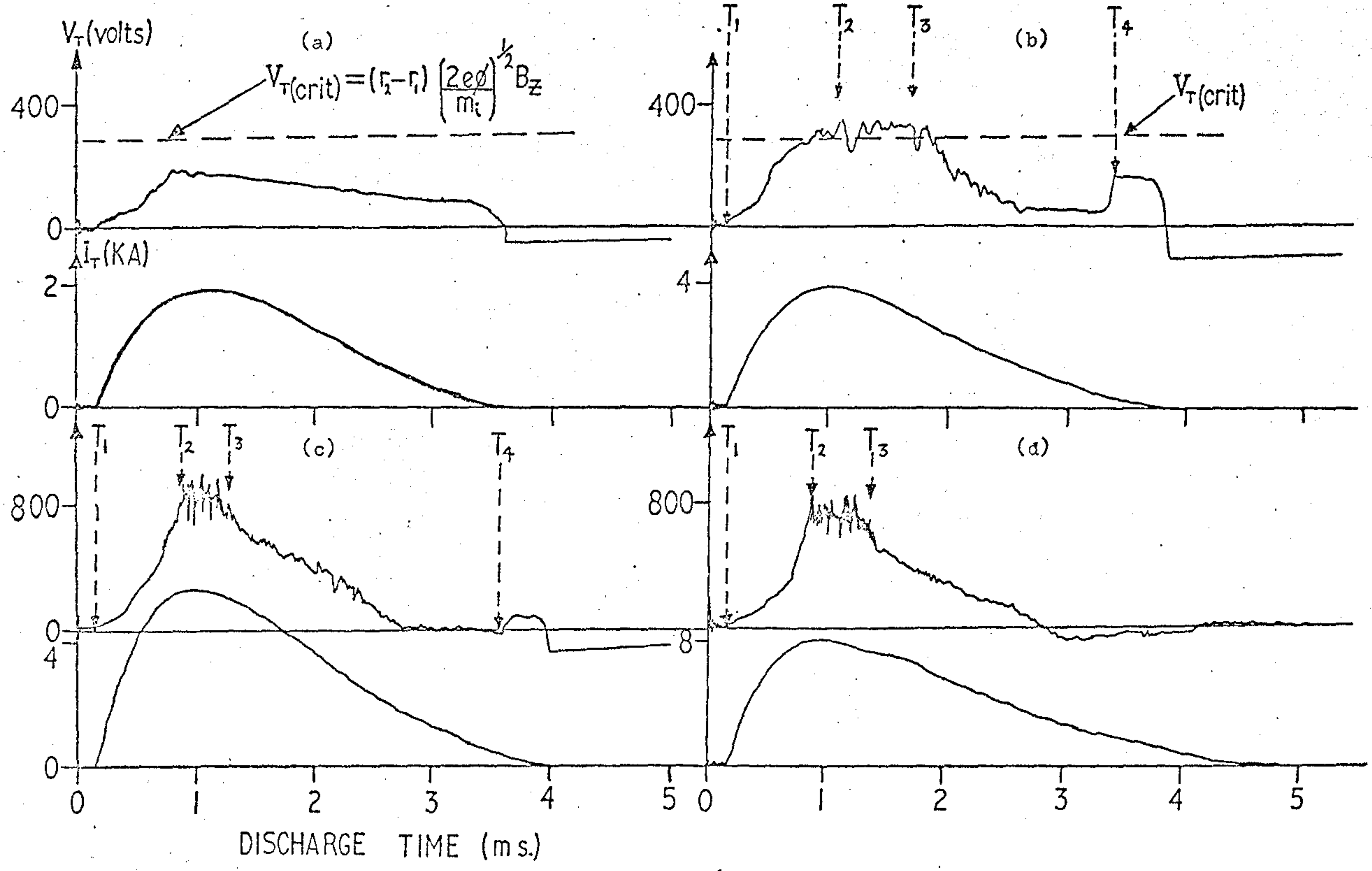

Fig.6.4
Typical oscillograms of the current and voltage in the E_R discharge with
$B_z = 0.1\,T$, $p_o = 50$ mtorr for various peak currents

tube voltages, large fluctuations appear. Radial electric field measurements (section 6.3) suggest that these voltage fluctuations are due to large amplitude oscillations in the electric field, which develop at radial positions of $r \leq 8$ cms from the anode during the plasma flow. After reaching the peak voltage at $t = T_2$ (Fig.6.4(c) and (d)), the average voltage remains constant for $\sim 500\,\mu s$ until at $t = T_3$ a rapid voltage decrease occurs. Plasma flow velocity and midplane electric field measurements, show that this voltage decrease cannot be attributed solely to the decay of the $v_\theta B_z$ polarising field. A likely explanation is that the voltage drop is caused by viscous effects at the top and bottom electrodes, which become predominant when the flow is fully developed (see section 2.3). This effect is more marked at higher B_z values.

The effect of B_z on the peak tube voltage, V_T, was also studied. Fig.6.5 shows the results of varying the magnetic field with constant peak E_R bank voltage (~ 8 KA peak radial current). As shown, the tube voltage scales directly with B_z. According to equation (2.25) the tube voltage should vary linearly with B_z if the anode sheath is negligible, or the sheath scales directly with B_z. Inspection of Fig.6.5 shows that $V_T \propto B_z$ for a machine filling pressure of 50 mtorr. The magnitude, however, is a factor of ~ 2 higher than that calculated from equation (2.25). Another problem which arises in the interpretation, is that electric field measurements (see section 6.3) show that over the measurable region ($r \approx 10 - 20$ cms) the plasma flow velocity also increases linearly with B_z and only approaches the critical velocity at the highest magnetic field of $B_z = 0.2\,T$. From equation (2.24) we would, therefore, expect that the tube voltage should scale as B_z^2. However, the measurable E_R profile only accounts for $\sim 10\%$ of the total interelectrode voltage, most of the interelectrode voltage being dropped in the region near the anode. In this region, v_θ must be independent of B_z for V_T to scale with B_z. A possible explanation, proposed

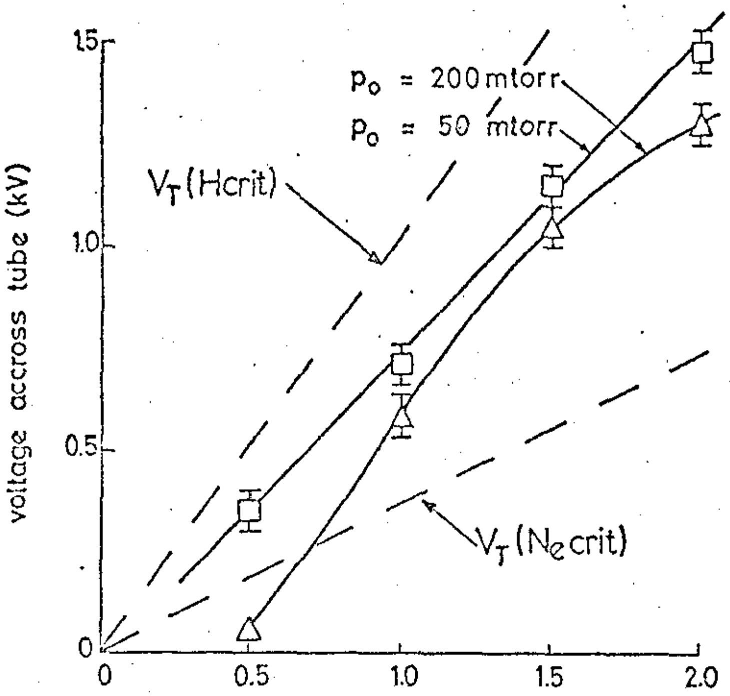

Fig.6.5
Experimental data showing the effect of B_z and p_o on tube voltage

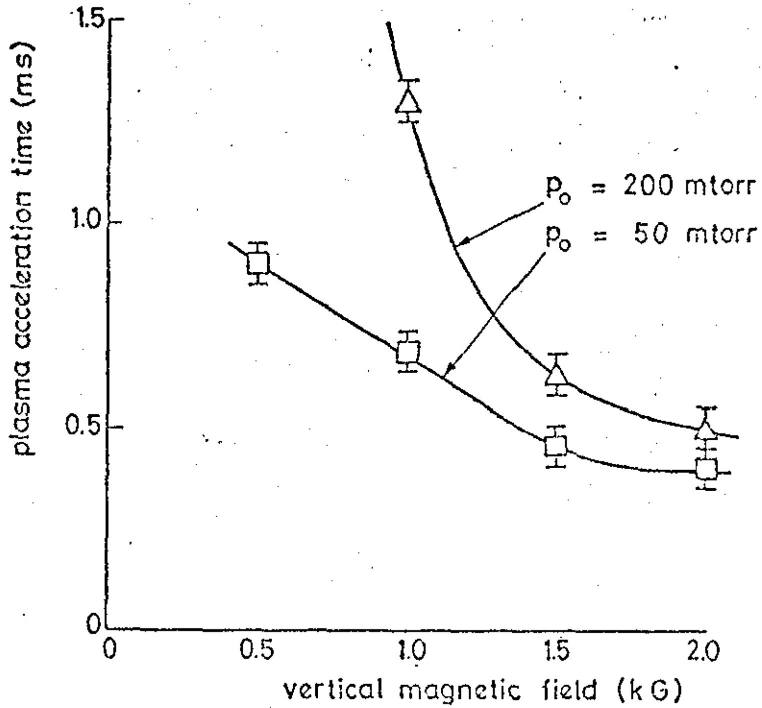

Fig.6.6
Experimental data showing the effect of B_z and p_o on the plasma acceleration time

by ANGERTH et al (1962) and SRNKA (1974), is that the electrode surfaces give off an amount of hydrogen into the discharge, and the critical electric field will then be determined by the hydrogen admixture. If $E = E_{crit}$ (hydrogen) from $r = 0 - 10$ cms, then the voltage drop $V_{(0-10)} = 0.1\ E_{crit} \simeq 1020\,V$ for the peak voltage condition at $B_z = 0.2\,T$, $V_{ER} = 8\,KV$. The voltage drop for the radial distance $\Delta r = 10 - 20$ cms at this condition, calculated from electric field measurements, gives $V_{(10-20)} \simeq 130\,V$ giving a total tube voltage of $V_T = 1150\,V$, compared with the observed tube voltage of $\sim 1475\,V$. It is likely, therefore, that an anode sheath also develops with the flow velocity due to the ion draining mechanism described in section 2.5.

Variations in the tube voltage and acceleration time (i.e. the time to reach the peak voltage plateau) with filling pressure, are shown in Fig. 6.6. The variation of the plasma acceleration time with p_o is attributed to the time taken to accelerate the neutrals and centrifuge them out before high plasma velocities can occur. The discrepancy between peak voltage for $B_z > 0.05\,T$ over the range $p_o = 50 - 200$ mtorr, is only $\sim 10\%$, in agreement with other rotating plasma experiments (ANGERTH et al (1962); FAHLESON (1961)). The small tube voltage for $p_o = 200$ mtorr, $B_z = 0.05\,T$ is interpreted as a small $v_\theta B_z$ polarising field (i.e. v_θ small). Since the velocity scales directly with B_z with $p_o = 50$ mtorr, this pressure was used for the majority of the experimental work

6.3. ELECTRIC FIELD MEASUREMENTS

Electric field measurements, using the coaxial probe and the circuit described in section 4.5, were made during the E_R discharge, primarily to determine the plasma flow velocity and the azimuthal symmetry of the plasma. A typical oscillogram of the radial electric field at $r = 12$ cms in the machine vertical midplane with $B_z = 0.1\,T$ and $V_{ER} = 8\,KV$ is shown in

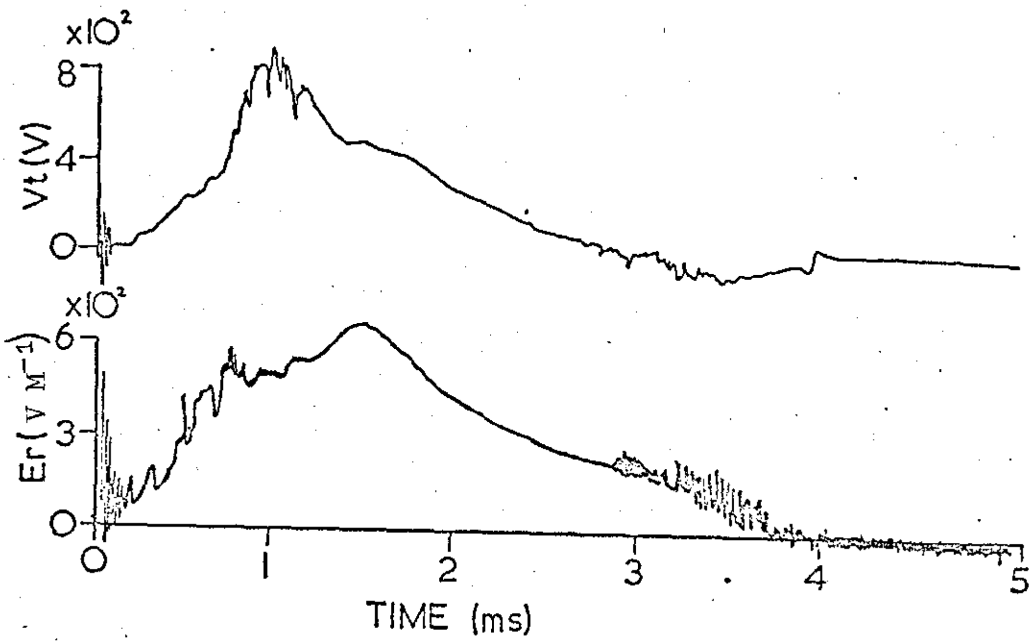

Fig.6.7
Typical oscillograms of electric field and tube voltage showing MHD instabilities during the acceleration and extinguishing phases of the discharge

Fig.6.7. The main features of the oscillogram, common to others taken at $\Delta r = 10 - 20$ cms, are that firstly, two-dimensional effects are evident owing to the fact that the integrated E_R profile (over Δr 10 - 20 cms) is larger than V_T at later times in the discharge; secondly, during the acceleration period, electric field fluctuations are evident indicating the presence of an MHD instability. These E_R fluctuations are followed by a stable flow of approximately 2 ms duration. Finally, high frequency ($\omega \approx 2 \times 10^6$ Hz) fluctuations appear when the tube voltage reverses and the plasma extinguishes.

Electric field and azimuthal current fluctuations have been observed in a number of rotating plasma experiments. These fluctuations are attributed to current spoking in the discharge. Rotating plasma devices usually have large enough currents to form cathode and anode spots, thereby causing non-uniform breakdown at different azimuthal positions. They should therefore have a natural tendency to form spokes, particularly during the early stages of the discharge.

Another mechanism which may be responsible for spoke formation, is the so-called 'netrual drag instability' (SIMON (1963); HOH (1963); LEHNERT (1971)). The basic mechanism for the instability is the frictional force produced by ion-neutral collisions which produces an azimuthal charge separation in rotating plasmas. With the inner electrode as anode, as with the Vortex experiment, the azimuthal electric field produced by the drag will lead to a radial motion toward the machine axis, this is counteracted by the outward centrifugal force.

Due to these two mechanisms, spokes will tend to form in the plasma body during the acceleration phase when the plasma is partially ionized. Spoking has been observed in a number of rotating plasmas during the acceleration period (BARBER et al (1963,1972); RASMUSSEN et al (1969); LEHNERT (1971)). If the input power is sufficient to ionize the neutrals in the plasma body, the neutral drag instability will be expected to be localised at the outer electrode and at the insulator surfaces at the end of the gas burn-out and acceleration period. There will always be neutrals present in these regions. In the Homopolar III experiments (BAKER et al (1961); KUNKEL et al (1963)), it was observed that the radial current was carried for the entire flow period ($\sim 400\ \mu s$) by a group of $10 \sim 13$ rotating current spokes. BERGSTROM et al (1963) also found that if the power input was insufficient to completely ionize the plasma volume (neglecting wall effects), spokes occurred throughout the discharge time. Further increase of input power above the gas 'burn-out' level, limited spoke formation to the acceleration period. It should also be mentioned that any deviation from solid body rotation ($v_\theta \propto r$) will tend to deform and smear out the spokes when the flow develops.

Good agreement is found in the Vortex II plasma with the experimental results from the experiments described above. At low input currents

($I_T \leq 4\,KA$) spoking occurs in Vortex II. A typical oscillogram taken at $r = 12$ cms with $I_{T\,(peak)} = 4\,KA$ and $B_z = 0.1\,T$ is shown in Fig.6.8. Velocity calculations from the radial electric field give ~ 10 spokes at this condition. In view of the fact that the symmetric current feed and the preheat plasma should prevent preferential E_R breakdown in the device, it is thought that the spoking is due to the lowly ionized state of the plasma. Langmuir probe and laser interferometer measurements, indicate that only about 10% of the gas is ionized at this discharge condition.

Spoke formation can be minimised using the maximum discharge energy. Fig.6.9 shows a typical oscillogram taken at $r = 12$ cms, with $I_{T\,(peak)} = 7.8\,KA$, $B_z = 0.2\,T$. In this case electric field inhomogeneities are restricted to the acceleration period, and the extinguishing phase of the discharge, indicating azimuthal uniformity (no spoking) for most of the discharge time. The most favourable conditions for the suppression of current spoking in the region $\Delta r = 10 - 20$ cms were found to be $B_z \geq 0.1\,T$ with the maximum E_R bank voltage of $V_{ER} = 8\,KV$. In view of the importance of having a stable flow for isotope separation, these discharge conditions were chosen for the majority of the separation experiments.

Radial scans of the electric field with $V_{ER} = 8\,KV$ and $B_z = 0.1\,T$, $0.2\,T$ are shown in Fig.6.10. The critical electric field, E_{crit}, calculated from equation (2.25) is also shown. The critical field is not exceeded at distances of $\Delta r = 10 - 20$ cms, although the value is approached at maximum B_z. Probe measurements were not possible at distances of less than 6 cms from the anode, as these measurements invariably resulted in the destruction of the probe. The mechanism responsible for this may be the formation of thin Hartmann layers on the probe surface (analogous to the end insulator damage discussed in section 5.2) with the result that large currents will destroy the probe (see section 2.4). From $\Delta r = 6 - 10$ cms,

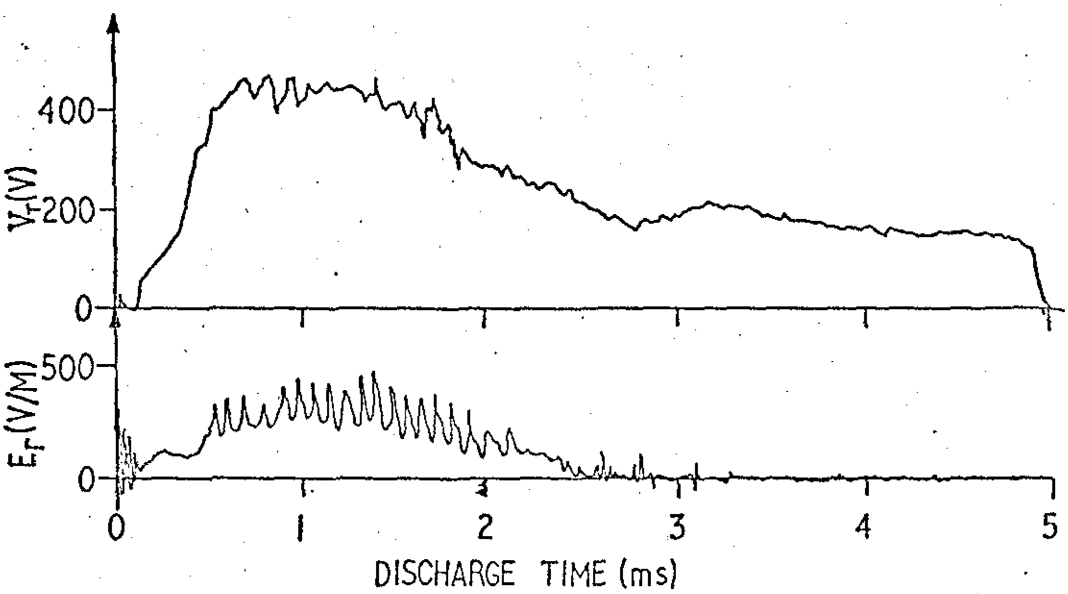

Fig.6.8
Typical oscillograms of electric field and tube voltage showing plasma spoking at low discharge currents

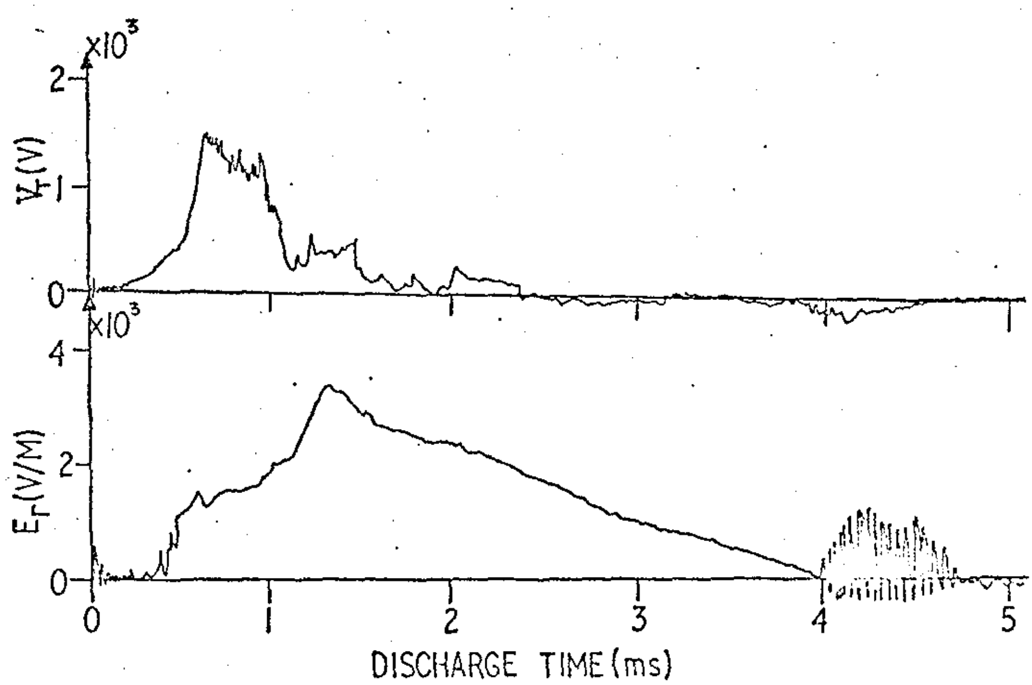

Fig.6.9
Typical oscillograms of electric field and tube voltage showing suppression of spoking at high magnetic field and discharge current

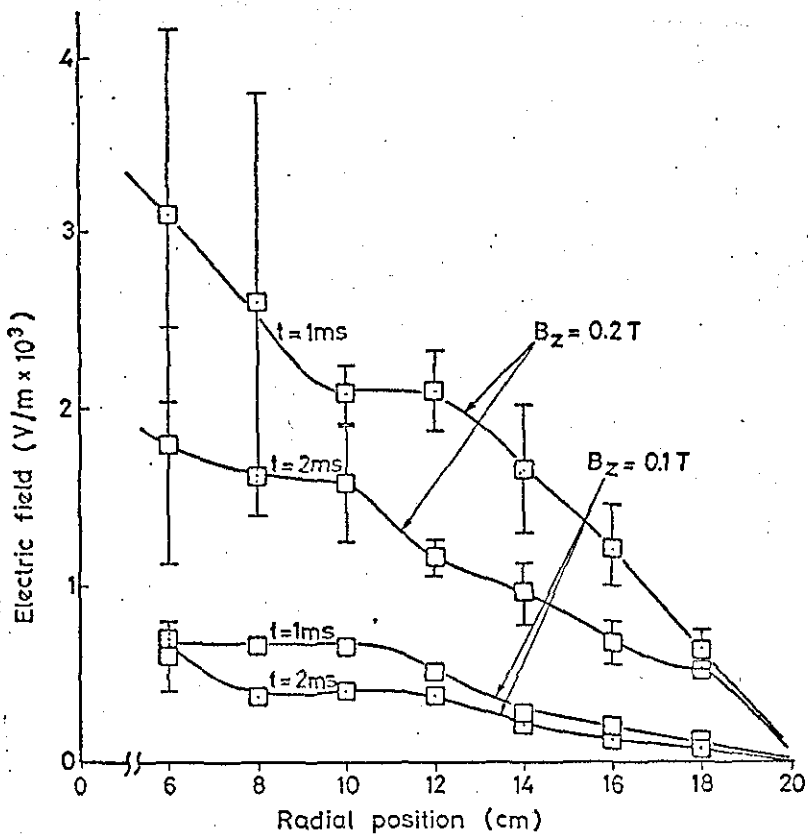

Fig.6.10
Radial electric field profiles for various times and magnetic fields

the region is catagorised with unreproducible large amplitude electric field fluctuations. Reproducible measurements were only obtained from $\Delta r = 10$–20 cms. It is interesting to note that this region corresponds to the position where detectable electron densities ($n_e > 10^{19}\ m^{-3}$) can be measured with the Langmuir probe (section 6.4.2).

6.4 ELECTRON DENSITY AND TEMPERATURE MEASUREMENTS

Density and temperature measurements were initially made using the swept Langmuir probe described in section 5.4. This method gave well-defined ion saturation currents, with zero probe current corresponding to zero probe voltage, as shown in Fig.5.8. The spatial and temporal behaviour of T_e and n_e in the E_R discharge was determined, and an absolute calibration was made of the probe n_e measurements with the CO_2 interferometer described in section 5.7. The $\int n_e\, dr$ profiles calculated from the probe measurements (assuming azimuthal symmetry) agreed with the absolute interferometer to within a factor of two. All n_e measurements shown in this section are the corrected values. An absolute calibration was not made for T_e; however, indirect evidence provided by directed Langmuir probe and plasma stagnation pressure measurements, showed good agreement with the swept measurement of T_e .

6.4.1 Temporal Variations

Time resolved measurements of T_e and n_e in the machine centre mid plane ($z = 0$, $r = 10$ cms) as a function of E_R bank voltage, with $B_z = 0.1\,T$, are given in Fig.6.11. The electron temperature remains reasonably constant throughout the discharge time at $\sim 3\,eV$ and this is independent of the E_R bank voltage for the range considered. Electron density peaks at $\sim 1\,ms$ after the E_R bank is triggered and then decays to zero after a further ~ 2.5 ms for the highest bank voltage. For $V_{ER} = 8\,KV$, the peak density is a factor of $\times 8$ larger than the PH density value, indicating that wall neutrals are recycled in the discharge. For $V_{ER} = 4\,KV$, the peak n_e shows only a marginal increase over the PH density (only $\sim 10\%$ of the initial particles are ionized at this condition).

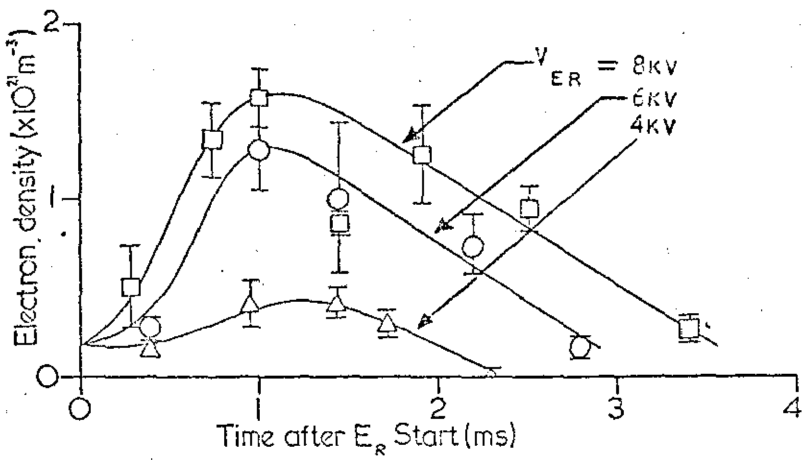

Fig.6.11

Time resolved measurements of T_e and n_e in the centre mid-plane for various bank voltages

Over the characteristic time scales of the discharge (typically 3.5 ms for maximum V_{ER}) both the electrons and ions will have Maxwellian velocity distributions, although the ions will have a displaced Maxwellian due to their azimuthal drift, which is comparable to their mean thermal velocity (see Table 6.1). The time to reach a Maxwellian velocity distribution from an initial arbitrary one, can be estimated from the 'self-collisional' time, t_c, of the interacting particles. This has been calculated by SPITZER (1962) to be,

$$t_c = \frac{11.4 \times 10^6 \, A \, T^{\frac{3}{2}}}{n Z^4 \, \ln \Lambda} \text{ sec.} \qquad \ldots (6.2)$$

where A is the mass number. Taking $T \approx 3.5 \times 10^4 \; {}^{\circ}K$, $n_e = 10^{21} m^{-3}$, $Z = 1$, $A_{neon} = 20.2$, $A_e = 1/1836$ and $\ln \Lambda = 10$ as typical values in the discharge, we obtain a self-collision time of $t_c \approx 2 \times 10^{-10}$ secs for the electrons and $t_c \approx 3 \times 10^{-8}$ secs for the neon ions. Thus both types of particles will rapidly randomised into Maxwellians. Equipartition of energy $(T_i = T_e)$ is also rapidly established in the E_R discharge. Ion-electron collisions are responsible for the production of energy isotropy. The $1/e$ time for energy equipartition is given by (SPITZER (1962)) as

$$t_{eq} = \frac{5.87 \times 10^6 \, A_i \, A_e}{n_e \, Z_i^2 \, \ln \Lambda} \left(\frac{T_i}{A_i} + \frac{T_e}{A_e} \right)^{\frac{3}{2}} \text{ sec} \qquad \ldots (6.3)$$

giving $t_{eq} \approx 3.3 \, \mu s$ for the typical values used above. Thus $T_e = T_i$ over the duration of the discharge.

Laser interferometer measurements of $\int_{r_1}^{r_2} n_e \, dr$ as a function ot time are shown in Fig.6.12. These results were obtained with the maximum bank voltage of $V_{ER} = 8\,KV$. The integrated density profiles obtained with the Langmuir probe (uncorrected values) are also shown. Although good agreement is found with the general shape of the density time dependence (see Fig.6.11), the probe measurements obtained with $B_z = 0.2\,T$ are approximately a factor of $\times 2$ too low. Better agreement is found at the lower magnitic field value of $B_z = 0.1\,T$. With a machine filling pressure, $p_o = 50\,mtorr$, the integrated line of sight neutral density across one radius is given by,

$$\int_{r_1}^{r_2} n_n \, dr = 3.52 \times 10^{20} \, m^{-2} \quad . \qquad \ldots (6.4)$$

Therefore $\sim 45\%$ of the initial gas is ionized with $B_z = 0.1\,T$ and $\sim 76\%$ ionized with $B_z = 0.2\,T$.

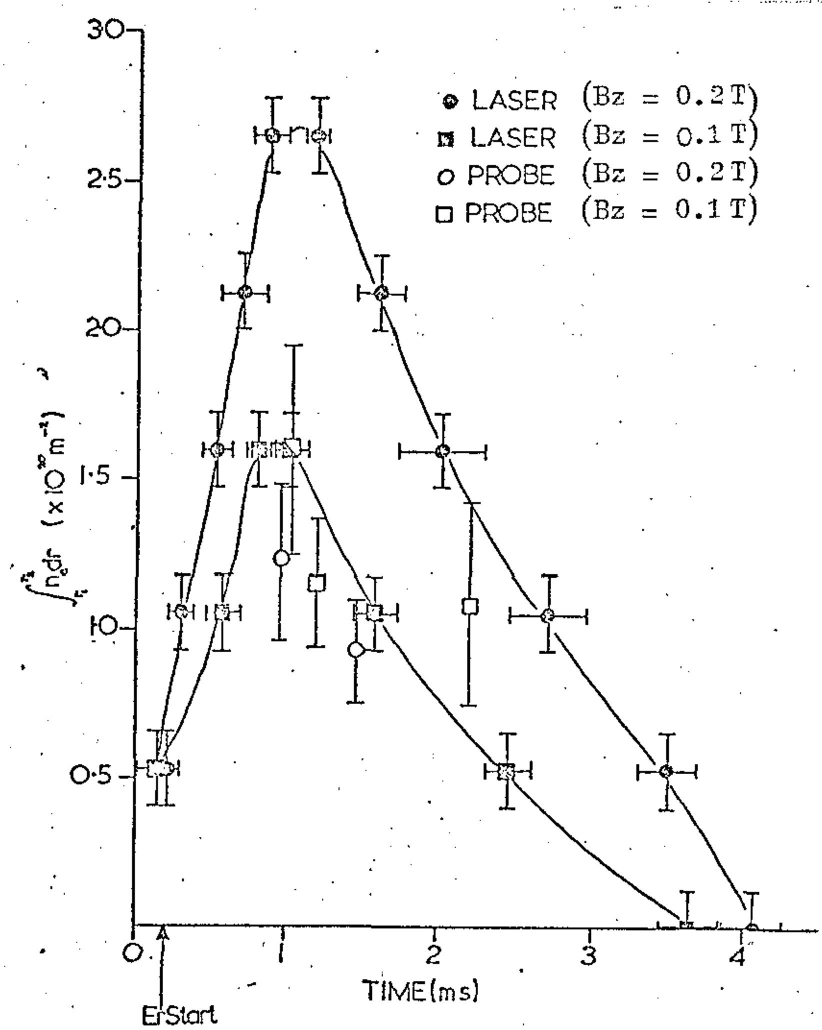

Fig.6.12
Comparison of the integrated density profiles from Langmuir probe and laser interferometer data

TABLE 6.1

SUMMARY OF TYPICAL PLASMA PARAMETERS FOR NEON AT THE CENTRE MID-PLANE POSITION, FOR MAXIMUM DISCHARGE ENERGY (V_{TD} = 8 KV)

Parameter		$\Delta r = 0.1$ m	$\Delta r = 0.14$ m	$\Delta r = 0.18$ m
(a) $B_z = 0.1$ T				
Electron number density, n_e	m^{-3}	1.2×10^{21}	1.4×10^{21}	1.0×10^{21}
Electron temperature, T_e	eV	4	4	3.5
Ion temperature, T_i	eV	4	4	3.5
Electron thermal speed, C_e	ms^{-1}	8.4×10^5	8.4×10^5	7.9×10^5
Ion thermal speed, C_i	m	4.4×10^3	4.4×10^3	4.1×10^3
Electron thermal gyro radius, a_e	m	4.8×10^{-5}	4.8×10^{-5}	4.5×10^{-5}
Ion thermal gyro radius, a_i	m	9.2×10^{-3}	9.2×10^{-3}	8.6×10^{-3}
Ion directed gyro radius, a_{di}	m	1.2×10^{-2}	6.3×10^{-3}	2.1×10^{-3}
Debye length, λ_D	m	4.3×10^{-7}	4.0×10^{-7}	4.7×10^{-7}
Flow velocity, v_f	ms^{-1}	6.5×10^3	3.0×10^3	1.0×10^3
Electron plasma frequency, ω_{pe}	rad s^{-1}	2.0×10^{12}	2.2×10^{12}	1.8×10^{12}
Ion plasma frequency, ω_{pi}	rad s^{-1}	1.0×10^{10}	1.1×10^{10}	9.4×10^9
Electron-ion collision time, τ_{ei}	s	9.1×10^{-10}	7.7×10^{-10}	1.0×10^{-9}
Ion-Ion collision time, τ_{ii}	s	3.0×10^{-7}	2.6×10^{-7}	2.9×10^{-7}
Electron orbits per collision, $\omega_e\tau_{ei}$		16.0	13.6	17.6
Ion orbits per collision, $\omega_i\tau_{ii}$		0.14	0.12	0.14
(b) $B_z = 0.2$ T				
Electron number density, n_e	m^{-3}	$\sim1.0\times10^{20}$	2.0×10^{21}	4.0×10^{21}
Electron temperature, T_e	eV	6	6	4
Ion temperature, T_i	eV	6	6	4
Electron thermal speed, C_e	ms^{-1}	1.0×10^6	1.0×10^6	8.4×10^5
Ion thermal speed, C_i	ms^{-1}	5.4×10^3	5.4×10^3	4.4×10^3
Electron thermal gyro radius, a_e	m	2.8×10^{-5}	2.8×10^{-5}	2.4×10^{-5}
Ion thermal gyro radius, a_i	m	5.4×10^{-3}	5.4×10^{-3}	4.4×10^{-3}
Ion directed gyro radius, a_{di}	m	1.4×10^{-2}	1.0×10^{-2}	5.0×10^{-3}
Debye length, λ_D	m	1.8×10^{-6}	4.0×10^{-7}	4.9×10^{-7}
Flow velocity, v_f	ms^{-1}	1.4×10^4	1.0×10^4	5.0×10^3
Electron plasma frequency, ω_{pe}	rad s^{-1}	5.6×10^{11}	2.5×10^{12}	3.5×10^{12}
Ion plasma frequency, ω_{pi}	rad s^{-1}	2.9×10^9	1.3×10^{10}	1.8×10^{10}
Electron-ion collision time, τ_{ei}	s	2.0×10^{-8}	1.0×10^{-9}	4.0×10^{-10}
Ion-ion collision time, τ_{ii}	s	6.7×10^{-6}	3.4×10^{-7}	1.3×10^{-7}
Electron orbits per collision, $\omega_e\tau_{ei}$		700	35	14
Ion orbits per collision, $\omega_i\tau_{ii}$		6.4	0.33	0.12

6.4.2 Radial Variations

Measurements made of the radial variations of T_e and n_e in the E_R discharge, show a number of features. Due to the centrifugal acceleration acting on the ions during the plasma flow, the ions diffuse preferentially to the outer electrode walls where large density gradients form. Ion drainage from the smaller radial positions leaves a diffuse region ($n_e < 10^{19}\ m^{-3}$) at distances of $r \leqslant 8$ cms from the anode. This low density region grows spatially with time until peak flow velocities occur (typically ~ 1 ms after the E_R start). Thereafter the plasma decelerates and the pressure gradient reduces with a corresponding back diffusion of particles to smaller radii.

Figure 6.13 shows the radial profile of T_e and n_e at different times, for $V_{ER} = 8$ KV and $B_z = 0.1$ T. The maximum density occurs at $\sim 800\ \mu s$ after the start of the E_R current pulse in good agreement with the integrated density interferometric measurements and the time resolved Langmuir probe measurements. Radial profiles taken with $V_{ER} = 8$ KV and $B_z = 0.2$ T, shown in Fig.6.14, clearly show the large density gradient.

Other important features shown are that firstly, very high densities ($\sim 4.5 \times 10^{21} m^{-3}$), occur at the outer radial positions, and secondly, the cooling effect of the electrode surface can be clearly seen.

The plasma balance may be analysed from equation (2.20). rewriting we have:

$$m_n \frac{V_\theta^2}{r} = \frac{\partial}{\partial r}\left(\frac{B^2}{2\mu_0}\right) + 2kT\ \frac{\partial n}{\partial r} + 2nk\ \frac{\partial T}{\partial r}\ . \qquad \ldots (6.5)$$

The first term on the right-hand side represents the magnetic field gradient. The magnetic field term is expected to be small, since $\omega_i \tau_{ii} \sim 0.1$ typically in the discharge (see Table 6.1). Referring to Fig.6.13, the magnitude of the individual terms may be calculated to check the validity of the equation. At $r = 10$ cms $t \approx 800\ \mu s$ after the E_R start, for example, we obtain:

$mn\,\dfrac{v_\theta^2}{r} = 7 \times 10^3\,\mathrm{N\,m^{-3}}$ and $kT\,\dfrac{\partial n}{\partial r} \approx 9.1 \times 10^3\,\mathrm{N\,m^{-3}}$ with $v_\theta \approx 6.5\,\mathrm{m\,s^{-1}}$, $T \approx 3\,\mathrm{eV}$, $\dfrac{\partial n}{\partial r} \approx 2 \times 10^{22}\,\mathrm{m^{-4}}$, $n \approx 1.2 \times 10^{21}\,\mathrm{m^{-3}}$. The agreement is good and justifies the view that magnetic field gradients must be small in the device. The outward centrifugal force is balanced at radial distances of $r < 14$ cms by the plasma pressure gradient in Fig.6.13 and for $r \leqslant 16$ cms in Fig.6.14. For larger radial distances, the radial balance is maintained by a high density neutral gradient which forms on the outer electrode. The magnitude of the neutral density can be estimated by the pressure balance at the outer wall; since v_θ is negligible at $r = 20$ cms, we have,

$$n_w k T_w = 2 n k T_e \qquad \ldots (6.6)$$

where n_w and T_w are the respective neutral density and temperature. Assuming $T_i \approx T_e \approx 2 \times 10^4\ {}^\circ\mathrm{K}$ with $n \approx 4 \times 10^{20}\,\mathrm{m^{-3}}$ near the outer electrode wall with $T_w \doteq 300\ {}^\circ\mathrm{K}$, we get $n_w \approx 5 \times 10^{22}\,\mathrm{m^{-3}}$. For $B_z = 0.1\,\mathrm{T}$ only 45% of the gas is analysed, giving the total number of neutrals present as $n_n \simeq 10^{20}$. If we now assume that the neutrals are confined to a region of $\delta r = 5$ mm from the wall, then the maximum possible n_w is given by

$$n_w \leq \frac{n_n}{2\pi r h\,\delta r} = 3 \times 10^{22}\,\mathrm{m^{-3}}. \qquad \ldots (6.7)$$

In view of the approximations made ($T_n = T_w = 300\ {}^\circ\mathrm{K}$) this is, at best only an order of magnitude estimate. It is obvious for instance, that the neutrals will have a higher temperature at the plasma boundary than at the wall. Also neutrals will also be present at the insulator surfaces.

The extent of the partially ionized boundary layer, L_n, can be estimated from Lehnert's formula (see section 2.5), which is,

$$L_n = \left(\frac{kT_b}{m\,\xi_n\,\xi}\right)^{\frac{1}{2}} \frac{1}{n_b} \qquad \ldots (6.8)$$

where ξ is given by von ENGEL and STEENBECK (1932) as,

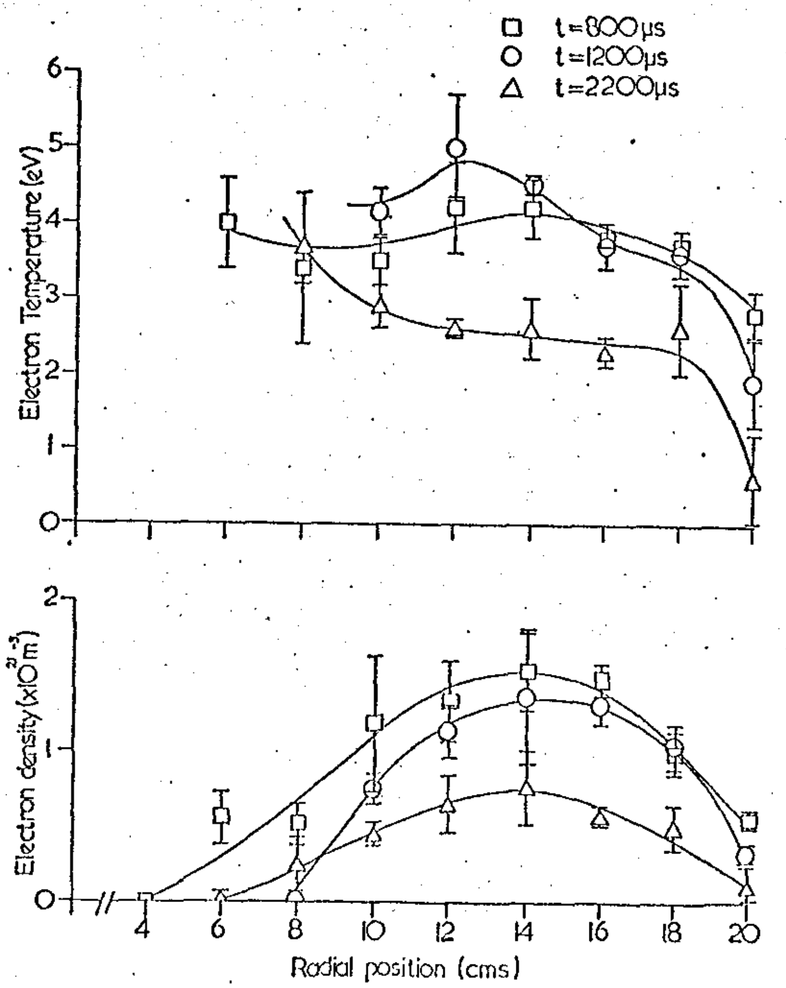

Fig.6.13
Radial profiles of T_e and corrected n_e at different times in the discharge

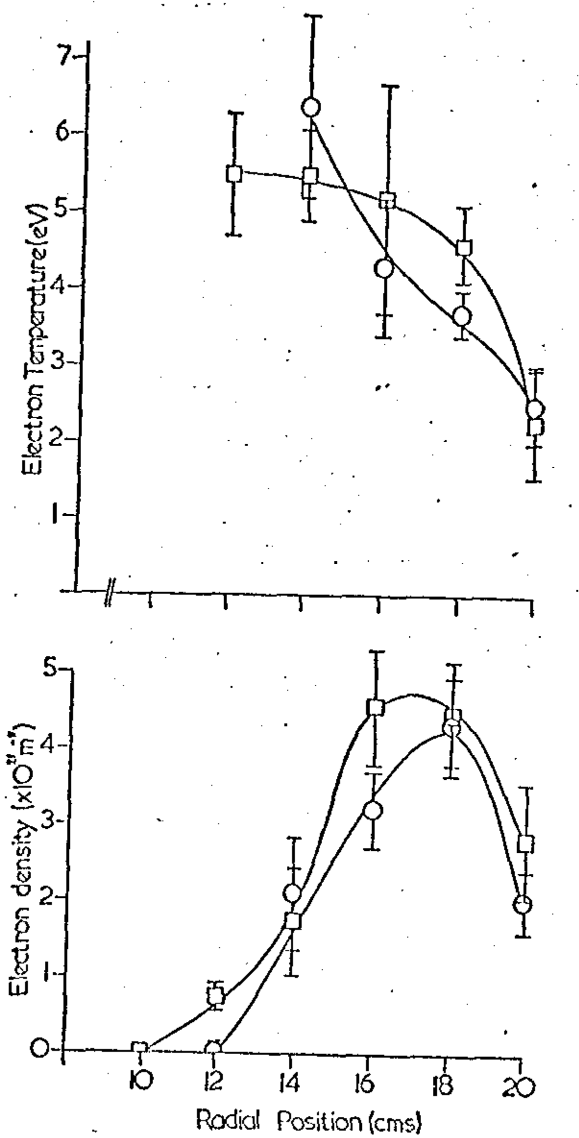

Fig.6.14
Radial profiles of T_e and corrected n_e for maximum bank voltage and magnetic field

$$\xi = 820\, a\, k \left(\frac{2e}{\pi m_e}\right)^{\frac{1}{2}} (\varphi_i \chi)^{\frac{3}{2}} \left(1 + \frac{1}{2\chi}\right) e^{-1/\chi} \qquad \dots (6.9)$$

with $\chi = \left(\frac{kT_e}{e\varphi_i}\right)$. The constant a is dependent upon the type of gas used. For neon, $a = 5.6$. Taking $T \approx 3.5 \times 10^4\ {}^0K$ as a typical temperature near the outer wall, gives $\xi \approx 4 \times 10^{-16}\, m^3 s^{-1}$. The effective momentum transfer frequency from ion-neutral collisions, ξ_n, is defined as,

$$\xi_n = \langle \sigma_{in} \omega_{in} \rangle \qquad \dots (6.10)$$

where σ_{in} is the momentum transfer cross section, and ω_{in} is the relative velocity of the ions and neutrals. The value of σ_{in} for neon has been found experimentally by GILBODY and HASTED (1956) to be $\sigma_{in\,(neon)} = 10^{-19}\, m^2$ at $T_i = 4\,eV$. Since σ_{in} is a slowly varying function with T, this value can be used for $T_i = 3\,eV$, without a large error in the calculation. Taking ω_{in} to be the mean thermal ion velocity (i.e. we assume the neutrals are at rest) we obtain $\xi_n \simeq 5 \times 10^{-16}\, m^3 s^{-1}$ giving $L_n \approx 1\,cm$ for a plasma boundary density of $n_b = 10^{21}\, m^{-3}$. This is probably a lower limit to L_n, since T_e is likely to be $\leq 3\,eV$ in the boundary region.

Since for $B_z \geq 0.1\,T$, $V_{ER} = 8\,KV$ we have $L_n < (r_2 - r_1)$ the plasma produced is impermeable to neutrals (see section 2.4). This may explain why plasma spoking occurs infrequently at these operating conditions.

6.5 DIRECTED LANGMUIR PROBE MEASUREMENTS

Directed Langmuir probe measurements were made in the E_R discharge as a circular check on T_e, n_e and v_θ, obtained with the laser and electric probes. We have seen in section 6.4.1, that the ions have a displaced Maxwellian distribution due to their net azimuthal drift. This is used to advantage by orientating the probe surfaces upstream, transverse and downstream to the plasma flow. As a first approximation, (see section (5.4.2) the difference between the upstream and transverse probe current will be equal to the directed ion current, that is,

$$I_p\,(\mathrm{up}) - I_p\,(\mathrm{trans}) \approx n_i\, e\, V_\theta A_p \qquad \ldots\ (6.11)$$

Results obtained at $r = 10$ cms with $B_z = 0.1$ T, $V_{ER} = 8$ KV are shown in Fig.6.15. The effect of the net azimuthal drift can be clearly seen. The electron density calculated from Bohm's formula with T_e given by the swept probe measurements, is a factor of ~ 2 lower than the swept probe n_e values, giving a peak density of $n_e \approx 5 \times 10^{20}$ m^{-3}. This may be due to differences in the probe construction. If the lower density values are used for consistancy, and substituted into equation (6.11), good agreement is obtained between the flow velocity calculated from E_R/B_z measurements. A comparison of the two methods is shown in section 6.6.

The directed probe also detects spoking in the discharge. Normally these occur in the acceleration period of the plasma (for $V_{ER} = 8$ KV, $B_z \geq 0.1$ T) as indicated by E_R probe measurements. Occasionally (approximately 10% of the time at $B_z = 0.1$ T, $V_{ER} = 8$ KV) spoking is seen throughout the discharge time. Since the spokes have a higher density associated with them than the rest of the plasma, this gives rise to large directed probe signals. A typical oscillogram taken at $\Delta r = 14$ cms from the anode, showing spoke formation in the discharge with $B_z = 0.1$ T, $V_{ER} = 8$ KV is shown in Fig.6.16. Assuming that two spokes are formed, then the flow velocity is approximation 5×10^3 ms^{-1} at $t = 1$ ms after the E_R start, in good agreement with E/B and directed probe results at $r = 14$ cms.

6.6 PLASMA FLOW VELOCITY

As mentioned, three independent methods were used to determine the plasma flow velocity in Vortex II; electric and directed probes and stagnation pressure measurements. Spoke formation measurements also served as a check on v_θ as previously described.

The justification for deriving v_θ from electric field measurements can be seen from equation (2.19). The flow velocity is given by,

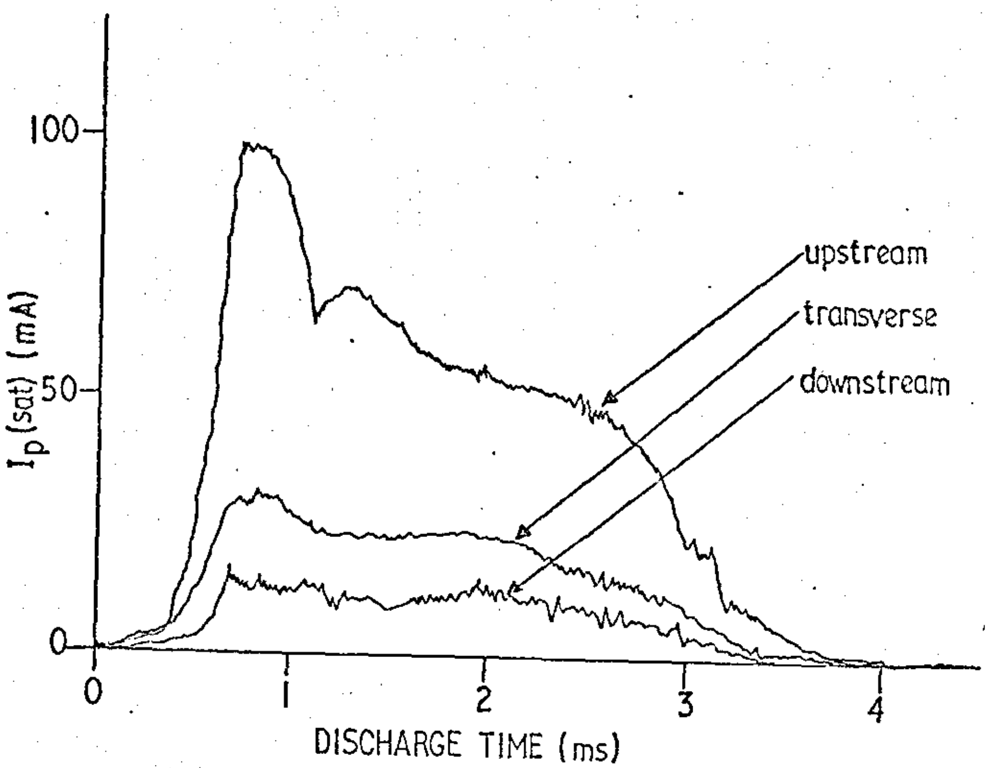

Fig.6.15
Typical oscillogram of directed Langmuir probe signal for various orientations in the plasma flow

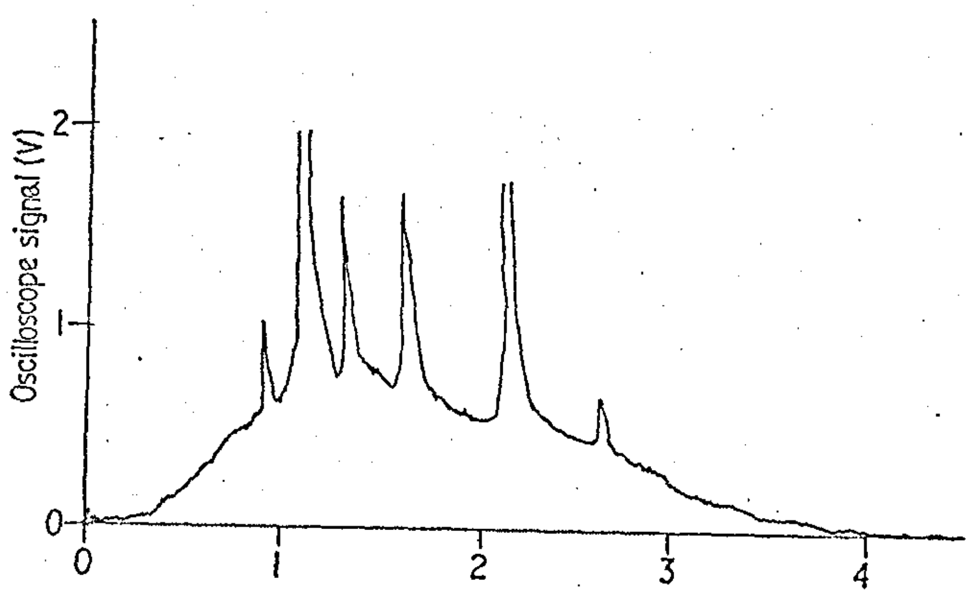

Fig.6.16
Typical oscillogram of directed probe signal when facing upstream in the presence of spoking

$$v_\theta = -\frac{E_R}{B_z} - \frac{m_i}{eB_z}\frac{v_\theta^2}{r} + \frac{kT}{e\,n\,B_z}\frac{\partial n}{\partial r} + \frac{k}{eB_z}\frac{\partial T}{\partial r} + \frac{\eta_\perp j_r}{B_z} \qquad \ldots (6.12)$$

where we have expanded the pressure gradient term. For $B_z = 0.1\,T$, $V_{ER} = 8\,KV$, $r = 10$ cms, $t = 1200\,\mu s$ after the E_R start, we obtain the following values for the constituents, $\frac{E_R}{B_z} \approx 6.5 \times 10^3$, $\frac{m_i}{eB_z}\frac{v_\theta^2}{r} \approx 3.5 \times 10^2$, $\frac{kT}{e\,n\,B_z}\frac{\partial n}{\partial r} \approx 1.6 \times 10^3$, $\frac{k}{eB_z}\frac{\partial T}{\partial r} \approx 0$ (constant T assumed), $\frac{\eta_\perp j_r}{B_z} \approx 35$. This implies that $v_\theta \approx \left|\frac{E_R}{B_z}\right|$ is a good approximation.

The time dependence of the plasma flow velocity with $B_z = 0.1\,T$ at $r = 10$ cms (corresponding to the maximum reproducible velocity measurements) is given in Fig.6.17. Peak flow velocities occur at ~ 1 ms after the E_R start. Velocity measurements calculated from directed Langmuir probe measurements using equation (6.11), show good agreement with the $^E/B$ values. Radial flow velocities can be calculated from Fig.6.10 by dividing by the appropriate B_z value. Velocity measurements obtained with $B_z = 0.1\,T$, $V_{ER} = 8\,KV$ and at $r = 12$ cms are shown in Fig.6.18. Here the velocity again peaks at ~ 1 ms after the E_R start, where it approaches the critical velocity for neon ($v_{\theta\,crit} = 1.4 \times 10^4\,m\,s^{-1}$). The flow velocity in this case is $\sim \times 2$ higher than peak velocity with $B_z = 0.1\,T$, implying that $v_\theta \propto B_z$ over the experimental range. Comparisons of results obtained on separate experimental runs (shown in Fig.6.18 as shaded and unshaded points) show that the discharge behaves reproducibly.

6.7 PLASMA FLOW STAGNATION PRESSURE MEASUREMENTS

As described in section 5.3.2, the fast valve sampling system can be used to determine the amount of gas collected from the discharge, and hence to calculate the equivalent pressure of the plasma flow if a valve calibration against pressured is obtained. Since the rotating plasma stagnation pressure, P_s, is given approximately by (BONNEVIER (1966)),

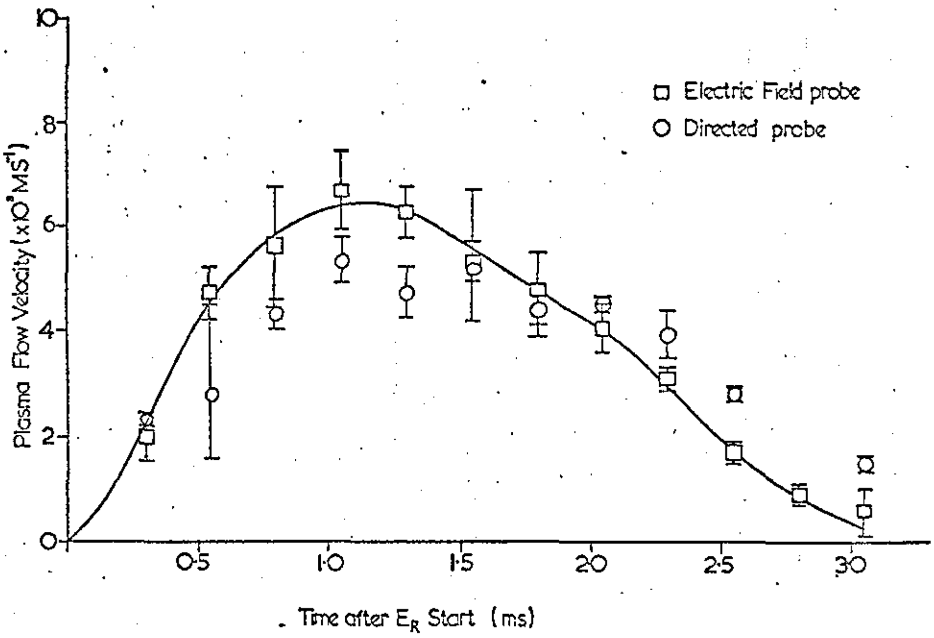

Fig.6.17
Comparison of flow velocities measured with the directed Langmuir probe and the electric field probe

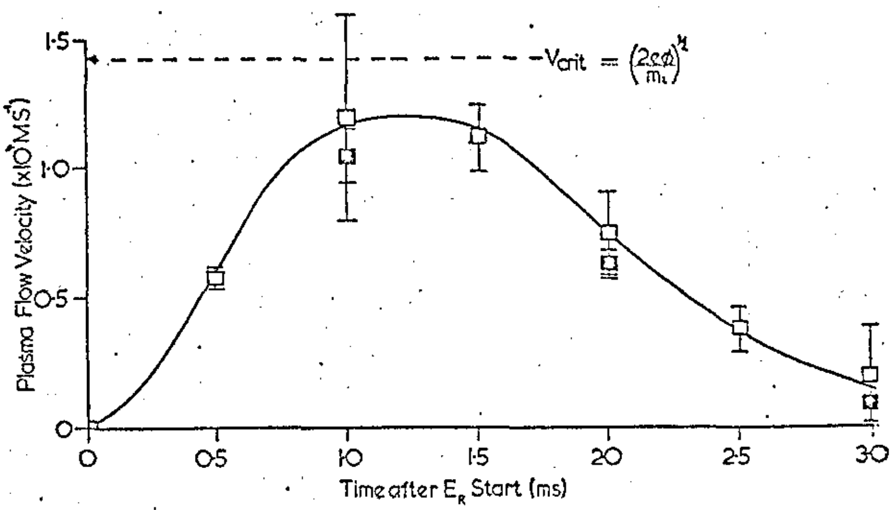

Fig.6.18
Plasma velocity measurements obtained with the electric probe at maximum plasma current and magnetic field, showing that the critical velocity is not exceeded in the VORTEX experiment

$$P_s \approx n_e \left(kT + \frac{m_i v_\theta^2}{2}\right) \qquad \ldots (6.13)$$

these measurements can be used as a circular check in $T = T_i = T_e$, v_θ and $n = n_i = n_e$. In view of the fact that the valve sampling time is $\sim 500\,\mu s$, these measurements will only give approximate values since both n will vary over the sampling time. Taking as typical values (averaged over $500\,\mu s$) at $r = 10$ cms; $n_e \approx 10^{21} m^{-3}$, $T \approx 4.6 \times 10\ {}^oK$, $v_\theta \approx 6.6 \times 10^3 m\, s^{-1}$ for $t = 1.1 \pm 0.25$ ms, after the E_R start with $B_z = 0.1$ T and $V_{ER} = 8$ KV, then using equation (6.13) we obtain an equivalent stagnation pressure of $P_s \approx 1.37 \times 10^3\ N/m^2 = 10.4$ torr. The measured stagnation pressure at this condition is ~ 15 torr. This is reasonable agreement in view of the approximations made. The stagnation pressure measurements have been incorporated with the separation results, since they give an indication of the amount of particles that can be collected from the plasma flow at different radii. This is of great importance in centrifuge performance.

6.8 SEPARATION RESULTS

The ratio of the abundance of ^{22}Ne to ^{20}Ne was measured in the initial (pre-rotation) gas (r_o), and also at the end of the discharge. The fast valve arrangement was also used to measure the abundance ratio both spatially and temporally in the plasma flow (r_p). From those results the percentage enrichment, E, defined by

$$E = \left(\frac{r_p - r_o}{r_o}\right) \times 100\% , \qquad \ldots (6.14)$$

was calculated as a function of time and position in the discharge.

Although the separation of different elements was not the primary aim of the experiment, a 50:50 mixture of argon and molecular nitrogen (i.e. 2 parts nitrogen atoms to 1 part argon atoms) was initially used to study the percentage enrichment obtained with large mass differences ($A_{argon} = 40$, $A_{nitrogen} = 14$) and to assess the feasibility of isotope separation in the device. Results obtained for $E(t)$ are shown in Fig. 6.19. The main features of this preliminary experiment are;

(a) Separations (E) are encouragingly high - the percentage enrichment of Argon rises to $\sim 120\%$ at $r = 18$ cms.

(b) The total number of nitrogen atoms is not conserved over the radius. This can be derived from the stagnation pressure measurement shown. Therefore there are relatively more *Ar* ions than N_2 ions present in the machine mid-plane position during the plasma rotation, than in the initial gas.

After the initial success, all further separation experiments used neon as the working gas.

6.8.1 Neon Isotope Separation

The variation in the measured E as a function of radius in the machine vertical mid-plane, with $B_z = 0.1\,T$, $V_{ER} = 8\,KV$ (corresponding to a peak $v_\theta \approx 6.6 \times 10^3 m\,s^{-1}$ at $r = 10$ cms), is shown in Fig.6.20. The valve mean open time was 1.1 ms after the E_R start. The percentage enrichment of ^{22}Ne is $\sim 15\%$ near the outer wall with a corresponding stagnation pressure of ~ 5 torr, implying that separations occur rapidly in the Vortex plasma. As with the $Ar : N_2$ separation, no corresponding depletion is observed at the inner plasma boundary. If the separation process is purely one-dimensional (i.e. takes place radially) then we must have from section 3.3.3.

$$\frac{\int_{r_1}^{r_2} n\,(22)\,dr}{\int_{r_1}^{r_2} n\,(20)\,dr} = r_o \qquad \ldots (6.14)$$

where $n(22)$ and $n(20)$ refer to the number densities of ^{22}Ne and ^{20}Ne. This is clearly not the case in the present experiment.

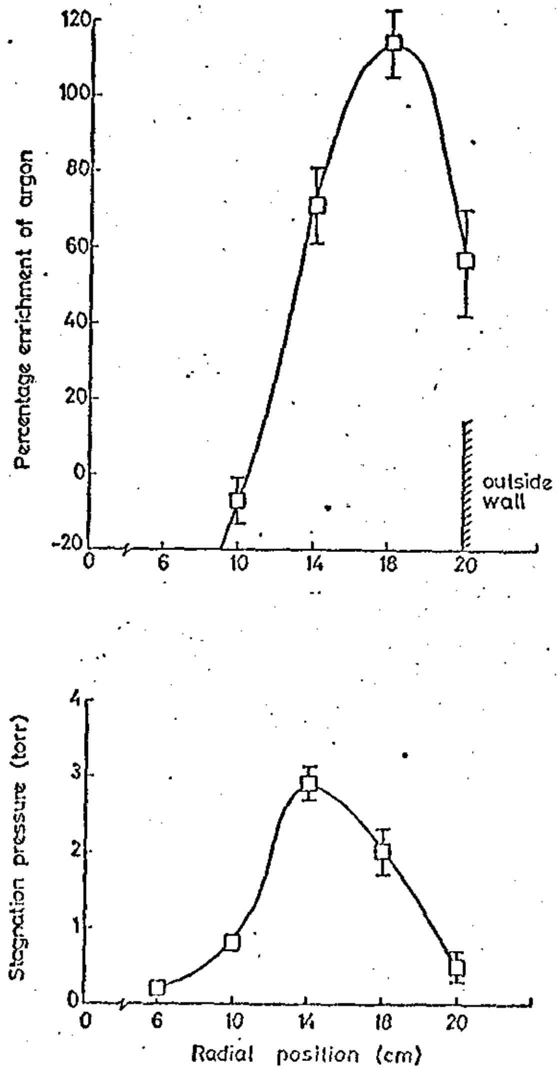

Fig.6.19

Percentage enrichment of argon and total stagnation pressure in a argon-nitrogen mixture with $V_{ER} = 4\,kV$, $B_z = 0.1\,T$

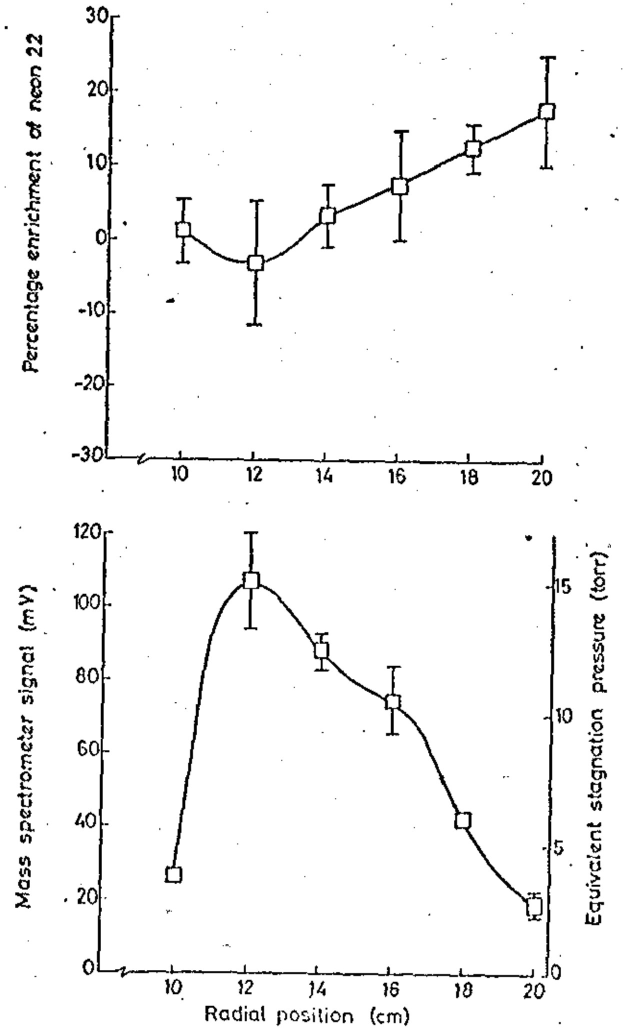

Fig.6.20

Spatial dependence of enrichment and stagnation pressure at 1.1 ms after the start of plasma rotation

Figure 6.21 shows the radial profiles of E at $t = 2 \pm 0.3$ ms after the discharge start. 15% ^{22}Ne enrichments are again evident at the outer wall. Note that the peak stagnation pressure has moved from $r = 12$ ($t = 1.1$ ms) to $r = 16$ cms due to the outward centrifugal expansion of the plasma.

Time resolved measurements of $E(t)$ made near the plasma boundary at $r = 18$ cms are shown in Fig.6.22. These results indicate that E increases as long as there is plasma rotation. The different symbols used in this figure represent separate experimental runs made to check reproducibility. Measurements taken at $t = 6$ ms and 16 ms after the end of the rotation, show that the isotopic abundance ratio of ^{22}Ne returns to its pre-rotation equilibrium value. Stagnation pressure measurements peak at ~ 1 ms after E_R start in good agreement with the density and velocity profiles obtained previously.

Measurements of $E(t)$ at $r = 12$ cms (near the inside boundary of the high density plasma volume) are shown in Fig.6.23. The results are in good agreement with the previous ones, in that no appreciable depletion of ^{22}Ne is observed, implying that the separation process is two-dimensional. Indeed, Fig.6.23 shows an enrichment of ^{22}Ne at this position.

To test the hypothesis that E was a function of r and z in the discharge, radial and time dependent scans were made at an off-axis position of $z + 7.5$ cms from the machine midplane. Measurements of the variation of E with radius are shown in Fig.6.24. Within experimental error, ^{22}Ne enrichments are the same at $r = 18$ cms as the corresponding $z = 0$ position. The stagnation pressure measurement is a factor of $\sim \times 2$ down on the $z = 0$ P_s measurements, suggesting that the plasma is compressed into the machine midplane by the associated $j_\theta B_r$ force (see section 2.2). The lower P_s measurement may also be due to a velocity decrease

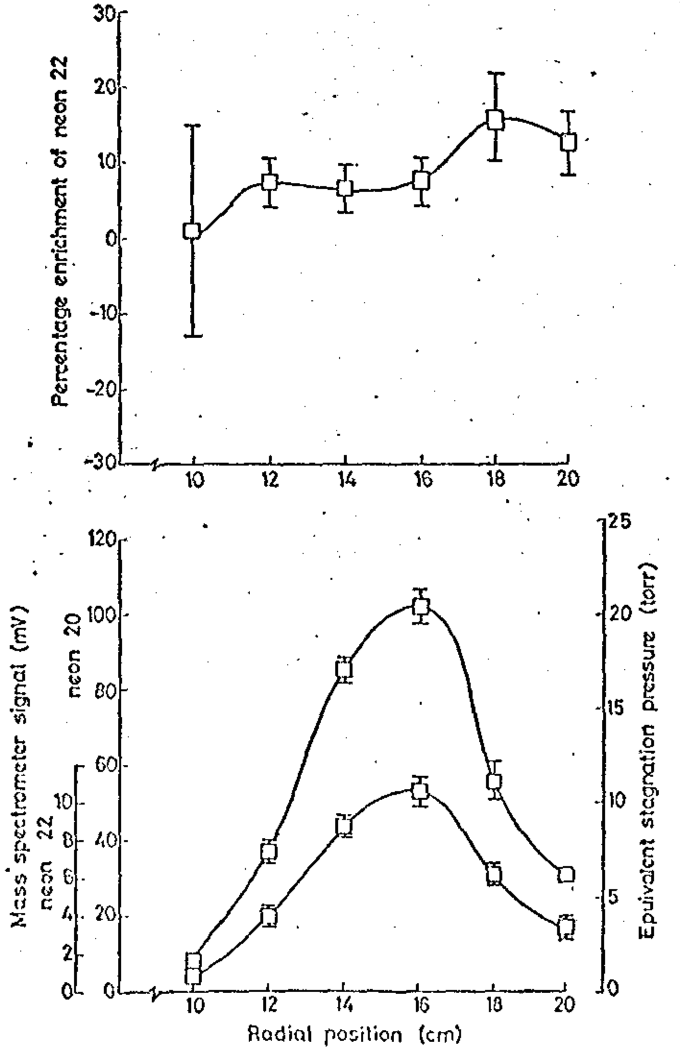

Fig.6.21

Spatial dependence of enrichment and stagnation pressure at 2.0ms after the start of plasma rotation

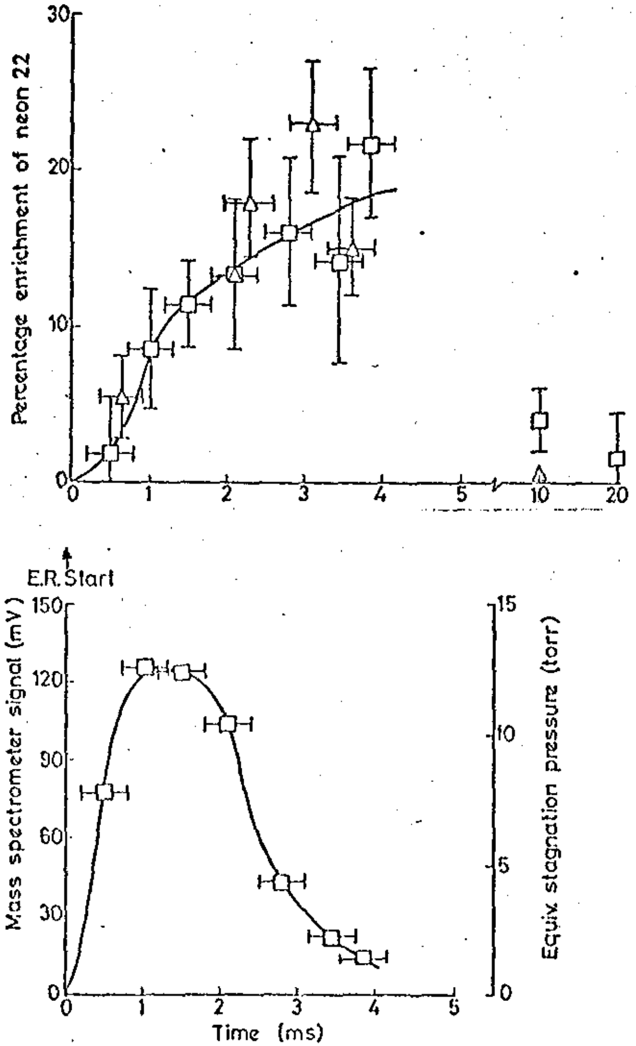

Fig.6.22

Time resolved measurements of enrichment and stagnation pressure near outer wall

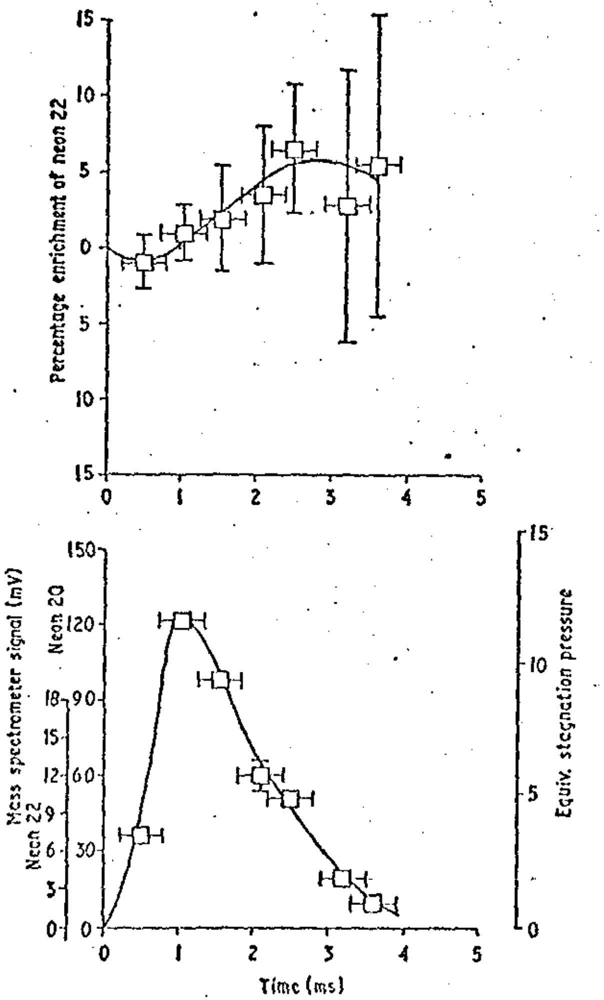

Fig.6.23

Time resolved measurements of separation near the inside boundary of the plasma

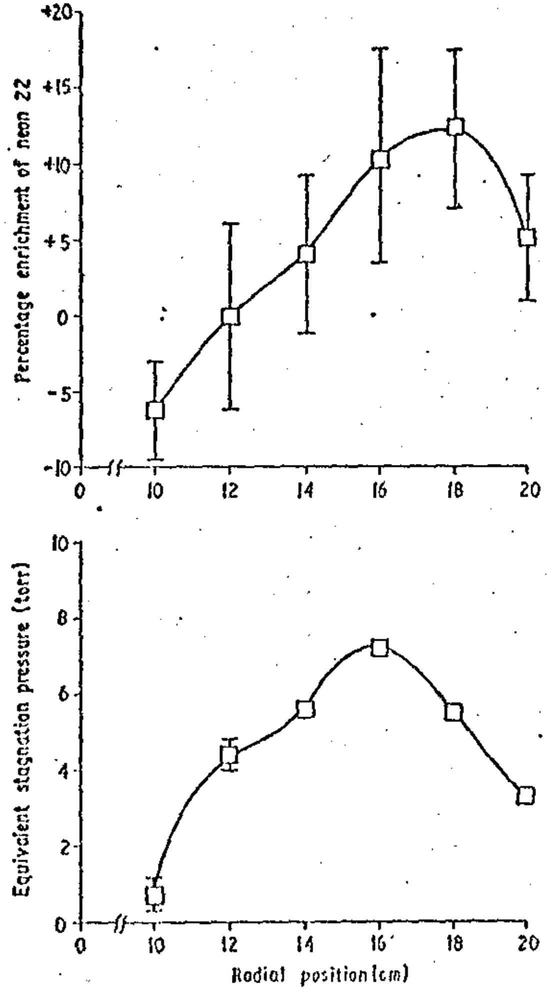

Fig.6.24

Radial profiles of enrichment and stagnation pressure taken at an off-axis position of 7.5 cm from centre mid-plane showing depletion of Ne 22 at the inner plasma boundary

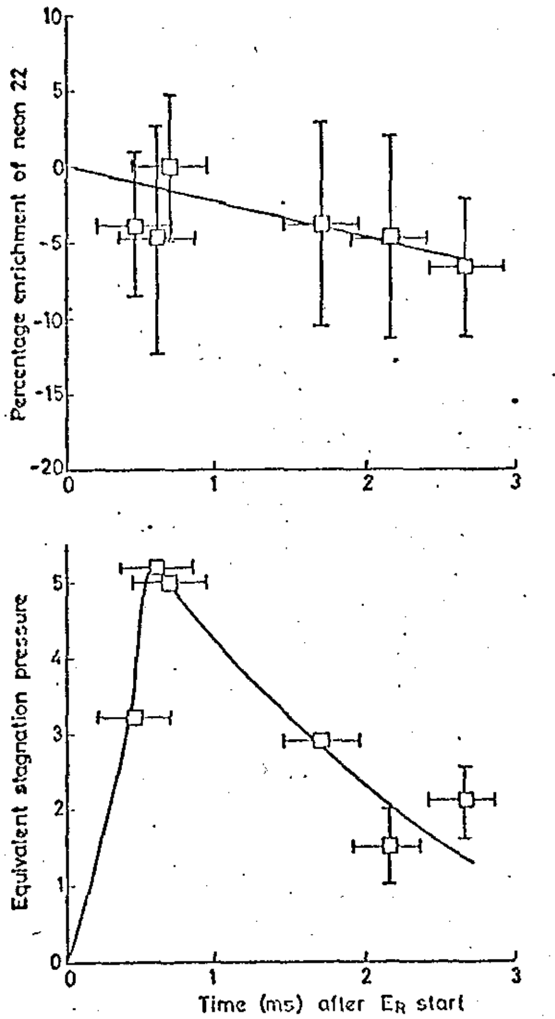

Fig.6.25

Time resolved measurements of separation near the inner plasma boundary at an off-axis position of 7.5 cm from centre mid-plane showing depletion of Ne 22

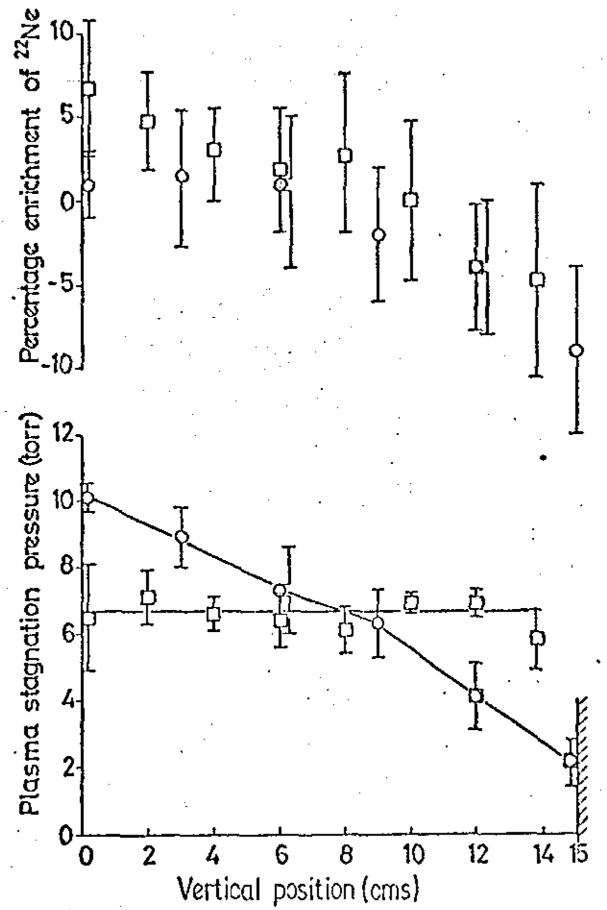

Fig.6.26

Vertical dependence of enrichment and stagnation pressure showing the two-dimensional nature of the separation effect or to plasma loss to the end insulators by ambipolar diffusion. At the inner plasma boundary, more ^{22}Ne depletion occurs than at $z = 0$. Time resolved measurements taken at $z = + 7.5$ cms, $r = 12$ cms, shown in Fig. 6.25, confirm that a depleted ^{22}Ne region does occur at this position. If we compare Fig.6.25 with results obtained at the same radial position but at the machine centre midplane, we see that instead of an enrichment of ^{22}Ne we now have a depleted region, supporting the view that 2-D separation is important in this device.

As a final check of the 2-D behaviour of E in the discharge, verticle scans of $E(z)$ were made at $r = 14$ cms with $B_z = 0.1\,T$, $V_{ER} = 8\,KV$ (same operating conditions as above). The results of two scans at different times are shown in Fig.6.26, Both the 2-D separation effect, with the heavier particles being concentrated preferentially in the machine midplane, and the plasma compression, with plasma losses to the walls, can be clearly seen.. Thus there is an axial as well as a radial separation effect, demonstrating the two-dimensional nature of the separation process.

6.9 OPTIMISATION

The figure of merit of a centrifuge, as mentioned in section 1.1, depends on both the enrichment and the total throughput of enriched material which can be achieved for a given power input. This is difficult to measure in the Vortex device owing to the strong spatial and time dependent nature of the discharge.

It is possible to estimate the efficiency of different operating conditions, however, by considering the mass flow and the associated enrichment at a particular point in the discharge. The isotopic throughput of ^{22}Ne, τ_{22}, is given by LONDON (1960) as,

$$\tau_{22} = \psi(N^{*} - N) \qquad \ldots (6.15)$$

where ψ is the flux of enriched ^{22}Ne isotope out ouf the device, N is the initial mole fraction of ^{22}Ne defined by,

$$N = \frac{^{22}Ne}{^{22}Ne + {}^{20}Ne} \qquad \ldots (6.16)$$

and N^* is the enriched mole fraction given by,

$$N^* = \frac{^{22}Ne^+}{^{22}Ne^+ + {}^{20}Ne^-} \quad .$$

The ratio of τ_{22} to the maximum power unput then gives a measure of the relative separation efficiency of each operating condition.

τ_{22} was found experimentally in the Vortex plasma at a radial distance of 0.18 m from the inner electrode. Since the plasma parameters (v_θ, n_e, T_e and η) did not vary appreciably over a distance of 0.005 m in the discharge, the mass flow was taken as flowing through a surface of $10^{-4}\,m^2$ normal to the flow. The mass flow, $\psi = m n v_\theta$ was obtained by measurements with Langmuir probes (to determine n) and electric field probes (to determine v_o). The results for various values of peak flow velocity are shown in Table 6.2.

TABLE 6.2

OPTIMISATION OF SEPARATION PARAMETER FOR ^{22}Ne AT $\Delta r = 18$ cms

Vertical Magnetic Field (Tesla)	Peak flow velocity $\times 10^4\,m\,s^{-1}$	Electron temperature $\times 10^4\,{}^oK$	η	τ_{22} Ne $\times 10^{-9}$ kgms/s	Peak Power MW	Normalised $\frac{\tau}{\text{peak power}}$
0.05	0.35	3.8	1.08	10.7	3.08	1.0
0.10	0.70	4.8	1.15	40.1	5.47	1.9
0.15	1.03	5.6	1.15	63.7	8.30	2.0
0.20	1.30	6.5	1.16	98.1	10.09	2.5

From the table it can be seen that the percentage enrichment remains virtually independent of the flow velocity at values greater than $v_\theta \approx 6.6 \times 10^3\,m\,s^{-1}$ in the device. This could be attributed to the additional plasma heating which occurs at these high flow velocities. Other mechanisms which may also explain this, although difficult to quantify, include turbulent mixing and the dimensional effects in the plasma. The greatest efficiency occurs at the highest flow velocity, chiefly as a result of the increased mass transport in the device.

CHAPTER VII

CONCLUSIONS

Two main conclusions can be drawn from the experimental work undertaken in this thesis. Firstly, Bonnevier's proposal that rotating plasmas can be used as isotope seperators has been confirmed experimentally; and secondly, two dimensional enrichment can occur in rotating plasmas contained in suitable homopolar geometries.

In this chapter, it will be shown that the simple process factor given from the theories presented in Chapter III is not sufficient to explain the high separation factor obtained experimentally, this is attributed to two-dimensional phenomena which have been shown to occur in the Vortex II plasma. Various physical mechanisms are proposed which may be responsible for this effect. Finally, the basic requirements of an envisaged continuously working uranium plasma centrifuge will be briefly outlined.

7.1 COMPARISON OF EXPERIMENTAL RESULTS WITH THEORY

The strong temporal and spatial dependence of the plasma parameters in the Vortex II device, the experimental errors of typically 10% for T_e, n_e and E_R, and approximately 30% for η, make comparison with the steady state separation theories given in Chapter III, difficult. However, the expressions derived for the simple process factor and density distribution given from equations 3.19 and 3.24 respectively as,

$$\frac{dy}{dr} = \frac{E_R^2 m_k\, y}{kT B_z^2\, r} - \frac{A_e B_z^2\; e}{k\, T\, \alpha\quad r} \qquad \ldots (7.1)$$

$$\frac{d\eta}{dr} = \frac{E_R^2 (m_j - m_k)\,\eta}{kT\, B_z^2\, r} - \frac{A_j\; e\; B_z}{n\; \alpha\quad rkT} \qquad .. (7.2)$$

should give the maximum value of η and n_e for any given E_R and T distribution in the absence of turbulent mixing (note that no E_R profile has been assumed in eqns.7.1 and 7.2). To test the validity of these equations in describing the experimental results, a polynomial fit of the experimental E_R profile was substituted into equations (7.1) and (7.2). In view of the experimental errors involved, a straight line fit was found adequate for E_R. Thus we put,

$$E_R = -mr + C \qquad \ldots (7.3)$$

with the slope, $m = 7.0 \times 10^3 V$ for $B_z = 0.1T$ and $m = 2.3 \times 10^4 V$ for $B_z = 0.2T$. With the boundary conditions of $E_R = 0$ at the outer boundary, $r = r_2$, we thus obtain,

$$E_R = m(r_2 - r). \qquad \ldots (7.4)$$

In the Vortex II plasma, terms due to the outward radial drift are small corrections to the centrifugal terms contained in equation (7.1) and (7.2) (see the discussion in section 3.2.2). Substitution of equation (7.4) into equation (7.1) and (7.2), ignoring the radial drift and using $n_e^2 = y$ we obtain the following for the separation factor and the electron density,

$$n_e = n_{e_{(r_1)}} \left(\frac{r}{r_1}\right)^{\alpha r_2^2} \exp\left[\alpha\left(2r_1r_2 - \frac{r_1^2}{2}\right)\right] \exp\left[\alpha\left(\frac{r^2}{2} - 2r_2r\right)\right] \quad (7.5)$$

with $\alpha = \dfrac{m^2 m_k}{2kT B_z^2}$

$$\eta = \eta_{(r_1)} \left(\frac{r}{r_1}\right)^{\beta r_2^2} \exp\left[\beta\left(2r_1r_2 - \frac{r_1^2}{2}\right)\right] \exp\left[\beta\left(\frac{r^2}{2} - 2r_2r\right)\right] \quad (7.6)$$

with $\beta = \dfrac{m^2(m_j - m_k)}{2kT B_z^2}$; where constant temperature has been assumed.

These expressions are plotted in Fig.7.1 together with the equivalent experimental results obtained 1 ms after the start of the E_R discharge with $V_{ER} = 8\,KV$, $B_z = 0.1T$ and assuming a uniform temperature of $T = 4\,eV$ throughout the plasma.

It is evident that the separation factor given by equation (7.6) is a factor of approximately 4 lower than the experimental results. The continuity of particles is also not conserved across the radius as previously mentioned in section 3.3.3 and section 6.8.

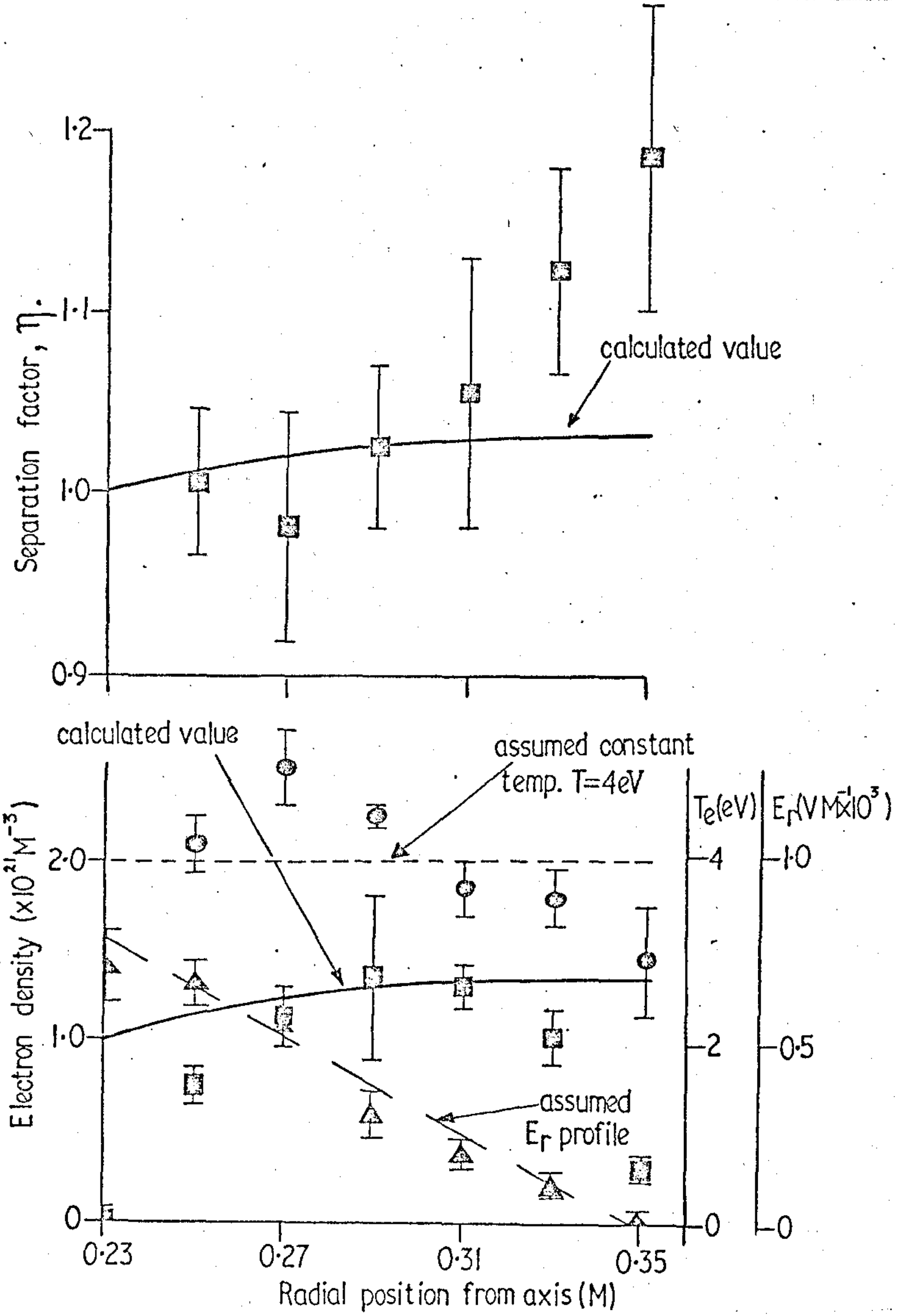

Fig.7.1
Comparison of theoretical and experimental results. The assumed temperature and electric field profiles used in the calculation are also shown

The predicted density profile is a poor fit to the experimental results. This is primarily due to the high density gradients which occur near the outer electrode wall ($r = 0.35\,m$). These are caused by the outward plasma motion and the back diffusion of neutral particles from the wall, an effect which has not been included in our simplified model. The assumed temperature uniformity will also tend to make the theoretical density gradient smaller than the measured values. This is due to the fact that the lower temperatures which occur naturally near the electrode walls will tend to steepen the gradient for a given flow velocity.

The separation results, however, are of primary interest in this thesis. Some of the mechanisms which may be responsible for the high separation factors obtained experimentally will now be discussed.

7.2 TWO-DIMENSIONAL SEPARATION MECHANISMS

Two basic mechanisms may lead to the high separation factors obtained. The first is separation which can occur along magnetic field lines which have a radial component. This was discussed in the case of Bonnevier's theory in section 3.1. The magnitude of this effect can be estimated from equation (3.7), if the relative value of the B_r and B_z components is known. The B_r component is difficult to determine in a quantitative fashion owing to the complex behaviour of the discharge. However, it is known that $B_r \ll B_z$ in Vortex II since the plasma is weakly magnetized (typically $\omega_i \tau_{ii} \sim 0.2$ at the highest B_z fields) and also from the experimental radial plasma balance analyzed in section 6.4.2. This analysis enables an upper estimate to be made of B_r. Taking $\frac{B_r}{B_z} \leq 0.1$ gives a separation of approximately 1% along the field. This is too small to account for the radial separation results shown in Fig.6.26, although the enrichment is in the right sense.

The second basic type of mechanism which could produce large separation factors, is that which sets up a poloidal flow pattern (in the r-z plane) in the device. In a conventional centrifuge, the simple process factor can be increased by a large factor by the introduction of a poloidal, counter-current flow. There are at least two ways in which a counter-current flow can be produced in Vortex II. These are; firstly, circulation induced by a B_θ field, and secondly, thermal convection.

The discussion of these mechanisms is necessarily subjective since even an approximate analysis of the enrichment process in a poloidal/azimuthal flow field requires resource to the two-dimensional plasma fluid equations which are outside the scope of this work.

7.2.1 Circulation Induced by a B_θ Field

A small but finite B_θ field exists in the Vortex II device due to the radial plasma current. At the start of the main discharge, this current will be initially uniform in the axial direction and will have a 1/r radial profile given by,

$$j_r = \frac{I_T}{2\pi r h} \qquad \dots (7.7)$$

B_θ can now be found from equation (2.16d) by integration over Z, with the boundary condition $B_\theta(r,\frac{h}{2}) = 0$. This gives,

$$B_\theta = \frac{\mu I_T}{4\pi r}\left(1-\frac{2z}{h}\right) \qquad \dots (7.8)$$

which is shown in Fig.7.2 for a plasma current of $I_T = 8\,\mathrm{kA}$.

The B_θ profile given in equation (7.8) is an over-simplification to the real case in Vortex II, since, as the plasma accelerates the majority of the radial current will flow in thin boundary layers at the top and bottom insulator surfaces due to the viscous effects described in section 2.3. This modifies the initial B_θ profile since j_r is no longer axially uniform. A better approximation to j_r is to regard the radial current as flowing in thin current sheets around the plasma boundaries. The return current leads

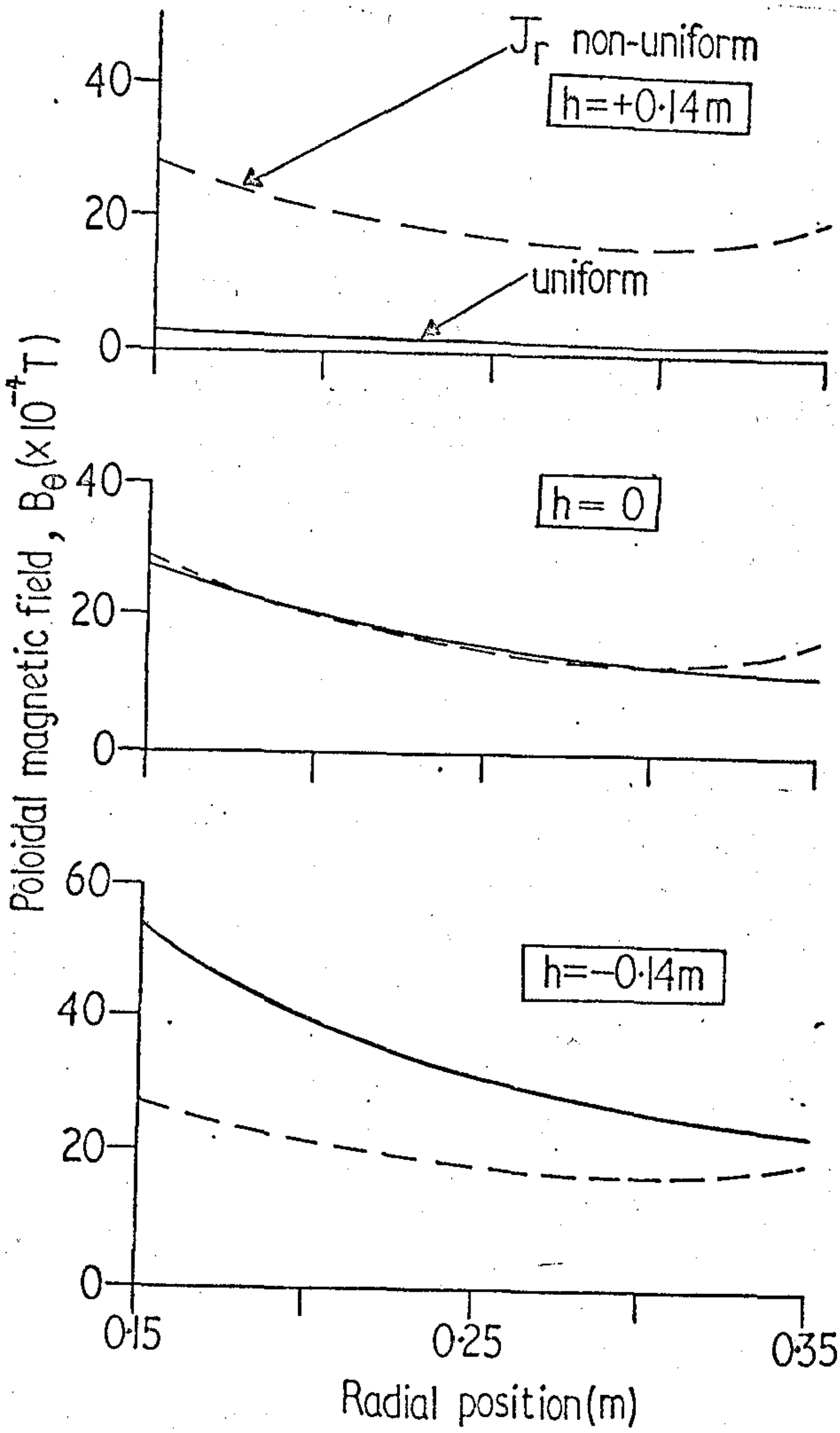

Fig.7.2
The radial and axial dependence of the calculated poloidal field produced in Vortex II for (a) an axially uniform plasma current of $I_T = 8$ kA, and (b) a boundary current of $I_T = 4$ kA (shown in Fig.7.3(b))

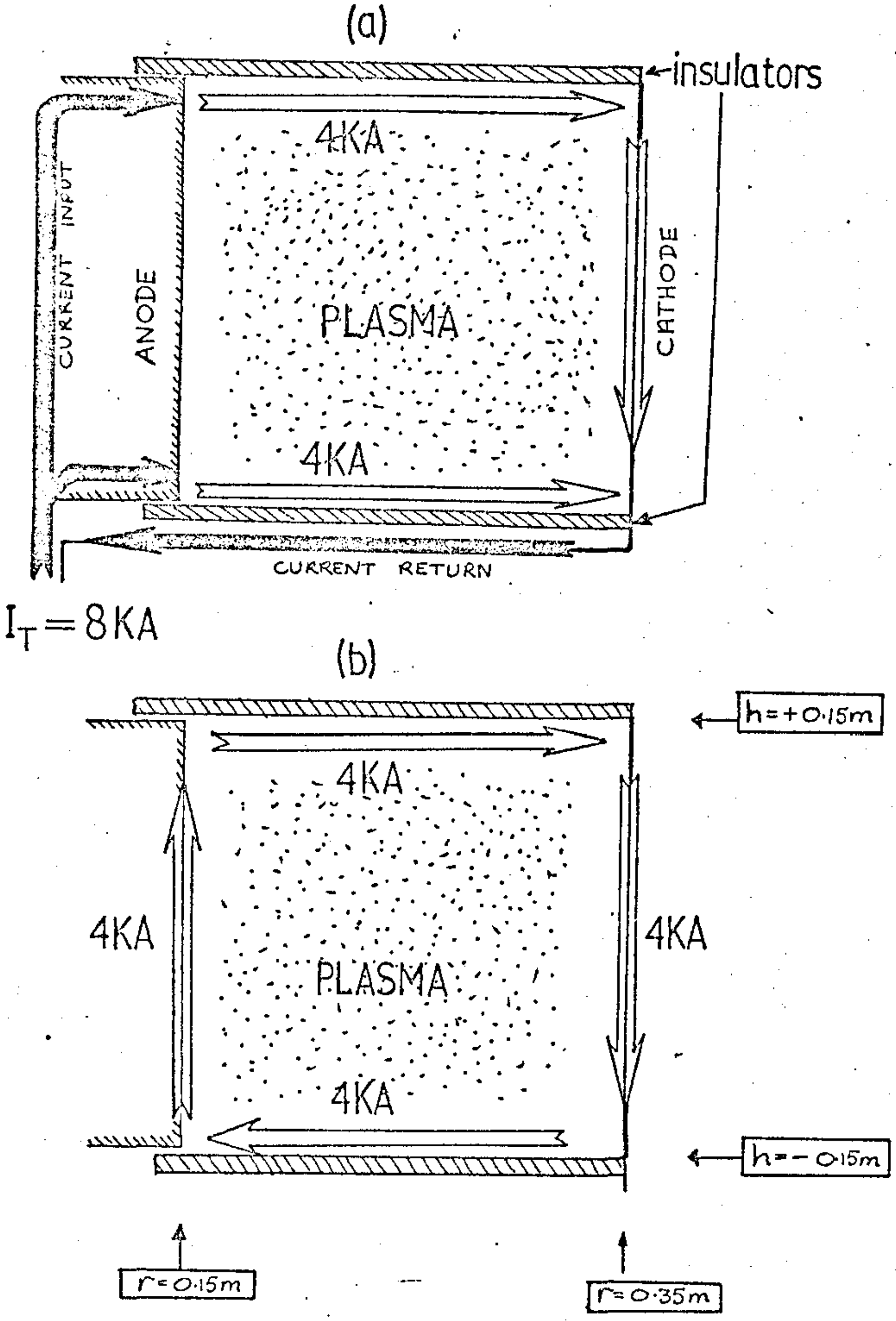

Fig.7.3
(a) The probable current distribution in Vortex II when the plasma is rotating, (b) The equivalent current circuit

below the bottom glass insulator allows the current distribution to be given by the profile shown in Fig.7.3. The B_θ field can be calculated analytically by comparison with the simple ring solenoid calculation. However, it was computed using a standard Culham Laboratory library routine (WILSON, 1975). The magnitude of the B_θ field obtained is shown in Fig.7.2. It is evident that B_θ is largest near the inner electrode, implying that the resulting $j_R \times B_\theta$ force is strongest near the inner electrode. This will produce a net axial plasma motion which will be strongest at the inner plasma boundary, leading to circulation and a counter-current flow.

7.2.2 Thermal Convection

In a mechanical centrifuge, the counter-current flow is produced by heating elements near the axis of the device. This produces a convection flow which is shown in Fig.7.4. Gas moves in the positive axial direction at the smaller radii, is cooled at the top, and returns along the outer radii. A similar heating effect occurs naturally in rotating plasma contained in homopolar geometry as shown by the experimental results presented in Figs.6.13 and 6.14. The resulting convection flow will be similar to that of a counter-current mechanical centrifuge. As previously mentioned, an analysis of this effect necessitates the use of the two dimensional energy equation. However, a general comment which can be made is that higher $\omega_i \tau_{ii}$ values will produce a larger temperature gradient, ∇T, due to the reduced thermal transport across the field. This will enhance the counter-current process in a plasma centrifuge and could well be an important consideration in future plasma centrifuge design.

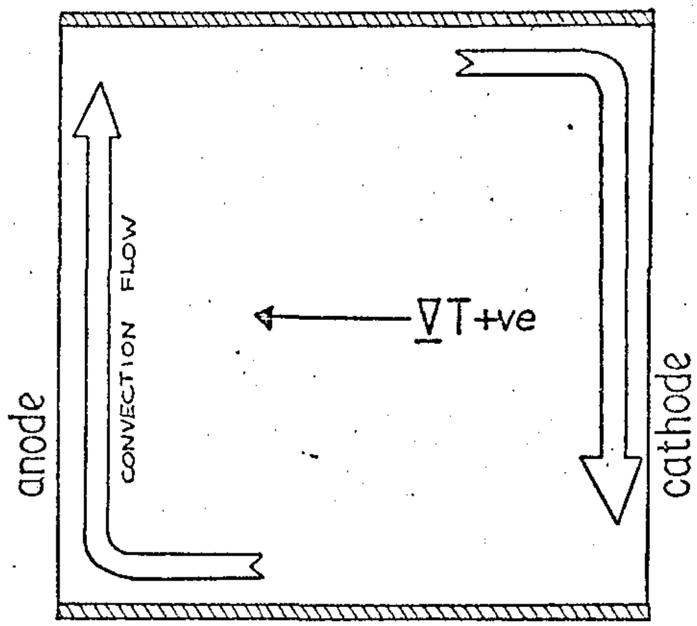

Fig.7.4
Schematic view of the plasma counter-current flow produced by thermal convection

7.3 THE FUTURE OF THE PLASMA CENTRIFUGE

The ultimate aim of any research in isotope separation is the enrichment of uranium in an efficient manner. Experimentation on rotating uranium plasmas with a view to enrichment, is presently being carried out by NATHRATH et al (1975). No separation results have yet been published.

Although the plasma centrifuge is at an early experimental and theoretical stage, it seems likely that the high power requirements of a fully ionized, steady state, rotating plasma (typically $\sim 1\,\mathrm{MW}$ in the Vortex II device) will mean that sufficient enrichment must be obtained in a very few stages for the device to be an economic proposition. With uranium as the working gas, for example, a separation factor of $\eta = 5$ is required to increase the ratio of U^{235} to U^{238} from 0.007 to 0.035 in one stage. This would be adequate for present day atomic reactors. Such a high separation factor will be difficult to achieve in a rotating plasma due to the high temperatures and the limiting velocity effect. This can be seen from the simple model developed in section 3.3. The separation factor is given from equation (3.26) by

$$\eta = \eta_{(r_1)} \exp \left\{ \frac{E^2_{R(r_1)} \; r_1^2}{B_z^2} \left(\frac{1}{r_1^2} - \frac{1}{r^2} \right) \right\} \qquad \ldots (7.9)$$

Taking $r_{max} = r_2 = 2\,r_1$ (since little advantage is gained by taking $r_2 > 2r_1$ as shown in Fig.3.4), setting $\eta_{(r_2)} = 5$ with $\eta_{(r_1)} = 1$ we obtain the following condition,

$$\frac{4}{3} \ln 5 = \frac{E^2_{R(r_1)}}{B_z^2} \; \frac{(m_j - m_k)}{2\,kT} \qquad \ldots (7.10)$$

Taking $T = 5 \times 10^0\mathrm{K}$, $B_z = 1.0\,\mathrm{T}$ as typical values and inserting numerical values in equation (7.10) we finally require

$$E_{R_{(r_1)}} \geq 2.43 \times 10^4\,\mathrm{V\,m^{-1}}$$

for a separation factor, $\eta \geq 5$. The critical electric field,

$$E_{crit} (E_{crit} = V_{crit} B_z)$$

for uranium, is, however,

$$E_{crit_{(U)}} = 2.2 \times 10^3 \, V\,m^{-1}.$$

Thus the plasma must rotate at ten times the critical velocity for a separation factor of 5 to be obtained. Therefore the critical velocity must be exceeded for the plasma centrifuge to challenge the present methods described in Chapter I. A possibility which yet remains to be investigated thoroughly is the gas seeding technique discussed in section 2.2. If hydrogen is used as the seeding gas, for example, then

$$E_{crit_{(H)}} = 5.1 \times 10^4 \, V\,m^{-1}$$

which is sufficient to give $\eta > 5$ in a uranium plasma centrifuge if the uranium ions are limited to the hydrogen critical velocity.

Further theoretical and experimental work is required on this new separation method before the plasma centrifuge could possibly present a viable alternative to present day enrichment technologies. In particular it is suggested that the theoretical aspects of two dimensional separation be investigated together with the energy requirements of rotating plasmas. The gas seeding technique may offer a method of overcoming the critical velocity effect and should be investigated experimentally.

APPENDIX A.1

THEORY OF ISOTOPIC SEPARATION IN ROTATING PLASMAS

A model of a quasi-neutral, azimuthally symmetric rotating plasmas containing singly ionized ions of type k and j with $m_j > m_k$ and $n_k \gg n_j$ is considered. The plasma rotates between two infinitely long coaxial electrodes of radii r_1 and r_2 in an axial magnetic field, B_z. The field is sufficiently strong such that $\omega_i \tau_{ii} \gg 1$ giving $v_\theta \gg v_r$ and $(P_{kq})_\theta \gg (P_{kq})_r$.

The steady state momentum balance is given, in the absence of viscous and gravitational terms, by,

$$n_k m_k \underline{v}_k \cdot \underline{\nabla} \underline{v}_k = e\, n_k \left(\underline{E} + \underline{v}_k \times \underline{B}\right) - \underline{\nabla} p_k - \sum_{k \neq q} \alpha_{kq} n_k n_q \left(\underline{v}_k - \underline{v}_q\right) \quad \ldots \text{(A1.1)}$$

The azimuthal velocity components of each particle species is given from equation (A1.1) by

$$v_{k\theta} = -\frac{E_R}{B_z} + \frac{m_k}{eB_z}\left[\frac{kT}{m_k}\;\frac{1}{n_k}\;\frac{dn_k}{dr} - \frac{v_{k\theta}^2}{r}\right] \quad \ldots \text{(A1.2a)}$$

$$v_{j\theta} = -\frac{E_R}{B_z} + \frac{m_j}{eB_z}\left[\frac{kT}{m_j}\;\frac{1}{n_j}\;\frac{dn_j}{dr} - \frac{v_{j\theta}^2}{r}\right] \quad \ldots \text{(A1.2b)}$$

$$v_{e\theta} = -\frac{E_R}{B_z} - \frac{kT}{eB_z}\;\frac{1}{n_e}\;\frac{dn_e}{dr} \quad \ldots \text{(A1.2c)}$$

where the electron inertial term has been neglected.

Equations (A1.2a) and A1.2b) may be written in terms of the electric field component if,

$$E_R > \frac{kT}{en_k}\;\frac{dn_k}{dr}$$

which is valid in the Vortex plasma and in many other rotating plasmas. We now have for the azimuthal velocity components,

$$v_{k\theta} = -\frac{E_R}{B_z} + \frac{m_k}{eB_z}\left[\frac{kT}{m_k}\ \frac{1}{n_k}\ \frac{dn_k}{dr} - \frac{E_R^2}{B_z^2 r}\right] \qquad \ldots \text{(A1.3a)}$$

$$v_{j\theta} = -\frac{E_R}{B_z} + \frac{m_j}{eB_z}\left[\frac{kT}{m_j}\ \frac{1}{n_j}\ \frac{dr_j}{dr} - \frac{E_R^2}{B_z^2 r}\right] \qquad \ldots \text{(A1.3b)}$$

$$v_{e\theta} = -\frac{E_R}{B_z} - \frac{kT}{eB_z}\frac{1}{n_e}\ \frac{dn_e}{dr} \qquad \ldots \text{(A1.3c)}$$

The radial velocity components are given by,

$$\begin{aligned} v_{kr} = &-\frac{kT}{e^2B_z^2}\ \alpha_{ke}\left(\frac{dn_e}{dr} + \frac{n_e}{n_k}\ \frac{dn_k}{dr} - \frac{m_k n_e}{kT}\ \frac{E_R^2}{B_z^2 r}\right) \\ &- \frac{kT}{e^2B_z^2}\ \alpha_{kj}\left(\frac{n_j}{n_k}\frac{dn_k}{dr} - \frac{dn_j}{dr} - \frac{n_j}{kT_r}\ \frac{E_R^2}{B_z^2}\,(m_k - m_j)\right) \end{aligned} \qquad \ldots \text{(A1.4a)}$$

$$\begin{aligned} v_{jr} = &-\frac{kT}{e^2B_z^2}\ \alpha_{ke}\left(\frac{dn_e}{dr} + \frac{n_e}{n_j}\frac{dn_j}{dr} - \frac{m_j n_e}{kT}\ \frac{E_r^2}{B_z^2 r}\right) \\ &- \frac{kT}{e^2B_z^2}\ \alpha_{kj}\left(\frac{n_k}{n_j}\ \frac{dn_j}{dr} - \frac{dn_k}{dr} - \frac{n_k}{kT_r}\ \frac{E_R^2}{B_z^2}\,(m_j - m_k)\right) \end{aligned} \qquad \ldots \text{(A1.4b)}$$

$$v_{er} = \frac{kT}{e^2B_z^2}\ \alpha_{ke}\left(\left(\frac{n_k}{n_e} + \frac{n_j}{n_e}\right)\frac{dn_e}{dr} + \frac{dn_k}{dr} + \frac{dn_j}{dr} - \frac{E_R^2}{kT\,B_z^2\,r}\left(n_k m_k + n_j m_j\right)\right) \qquad \ldots \text{(A1.4c)}$$

The steady state continuity equations for each species in the absence of ionization and loss terms are written,

$$n_k v_{kr} r = A_k \qquad \ldots \text{(A1.5a)}$$

$$n_j v_{jr} r = A_j \qquad \ldots \text{(A1.5b)}$$

$$n_e v_{er} r = A_e \qquad \ldots \text{(A1.5c)}$$

where the constants, A_k, A_j and A_e are related to the radial plasma current by,

$$J_R = \frac{e}{r}\left(A_k + A_j - A_e\right) \qquad \ldots \text{(A1.6)}$$

Equations (A1.3) to (A1.6) form the basis of our theoretical model. The density distribution is obtained from equation (A1.4c) with equation (A1.5c), this gives,

$$-\frac{A_e e^2 B_z^2}{kT\,\alpha_{ke}\, r} = \frac{dn_e^2}{dr} - \frac{E_R^2}{kT\,B_z^2\, r}\, n_e\, (n_k m_k + n_j m_j) \qquad \ldots \text{(A1.7)}$$

where we have assumed quasi-neutrality ($n_e \approx n_j + n_k$).

Since in our approximation the heavier ion species number density $n_j \ll n_k$ (valid for neon) and since $m_k \sim m_j$, equation (A1.7) may be written to a good approximation,

$$-\frac{A_e e^2 B_z^2}{kT\,\alpha_{ke}\, r} = \frac{dn_e^2}{dr} - \frac{E_R^2}{kT\,B_z^2\, r}\, m_k n_e^2 \qquad \ldots \text{(A1.8)}$$

An expression for the radial dependence of E_R is required before equation (A1.8) can be solved. We choose the zero space charge condition giving,

$$E_R = E_{R(r_1)}\,\frac{r_1}{r} \qquad \ldots \text{(A1.9)}$$

Substitution of equation A1.9) into equation (A1.8) and solving, we obtain the following for the radial dependence of the electron density

$$\boxed{n_e = n_{e(r_1)}\, e^{-t/2}\left(e^{t(r_1)} + \frac{\lambda}{n^2_{e(r_1)}}\left(\int_{-\infty}^{t} \frac{e^t}{t}\,dt - \int_{-\infty}^{t(r_1)} \frac{e^t}{t}\,dt\right)\right)^{\frac{1}{2}}} \qquad \ldots \text{(A1.10)}$$

where

$$t = \frac{E^2_{R(r_1)}\, m_k}{2\,kT\,B_z^2} \quad \text{and} \quad \lambda = \frac{A_e e^2 B_z^2}{2\,kT\,\alpha_{ke}}\,.$$

The separation factor is calculated by considering the radial ion velocities and ion continuity. Substituting equation (A1.4a) into equation (A1.5a) using $n_k \sim n_e$ we obtain,

$$\frac{\alpha_{kj}}{e^2 B_z^2}\left[r\,kT\,n_k^2\,\frac{d}{dr}\left(\frac{n_j}{n_k}\right) - \frac{E_R^2}{B_z^2}\, n_k n_j (m_j - m_k)\right] = -\,(A_e - A_k) \qquad \ldots \text{(A1.11)}$$

The right-hand-side is given from equation (A1.6) by

$$-\,(A_e - A_k) = \left(\frac{r}{e}\right) J_r - A_j \qquad \ldots \text{(A1.12)}$$

We now assume that J_R is small in the body of the rotating plasma. Substituting equation (A1.9) and (A1.12) (with $J_R = 0$) into equation (A1.11) we obtain for the separation factor

$$\boxed{\frac{n_j}{n_k} = \eta = \eta_{(r_1)} \exp\left(- \frac{\gamma}{r_1^2}\right) \left(\exp\left(\frac{\gamma}{r_1^2} - \frac{\beta}{\eta_{(r_1)}} \int_{r_1^2}^{r^2} \frac{1}{r^2 y} \exp\left(\frac{\gamma}{r^2}\right) dr^2\right)\right.} \qquad \ldots \text{(A1.13)}$$

where

$$\beta = \frac{A_j\, e^2 B_z^2}{2\, \alpha_{kj}\, kT} \quad \text{and} \quad \gamma = \left(\frac{E_{R(r_1)}\, r_1}{B_z}\right)^2 \left(\frac{m_j - m_k}{2\, kT}\right)$$

REFERENCES

ALFVEN, H., 'On the Origin of the Solar System', Oxford University Press (1954).

ALFVEN, H., Rev. Mod. Phys., 32, 710 (1960).

ANDERSON, O.A., BAKER, W.R., BRATENAHL, A., FURTH, H.P., ISE, J., KUNKEL, W.B. and STONE, J.M., Proc. 2nd Int. Conf. Peaceful Uses of Atomic Energy, 32, 155 Geneva (1958).

ANGERTH, B., BLOCK, L., FAHLESON, U. and SOOP, K., Nuclear Fusion, Suppl. part 1, 39 (1962).

ALLEN, J.E., BOYD, R.L.F. and REYNOLDS, P., Proc. Phys. Soc. B., 70, 297 (1957).

ALLEN, J.E. and MAGISTRELLI, F., Proc. Int. Conf. Ionised Gases, p.599 Upsala (1959

ALLEN, J.E. and MAGISTRELLI, F., Comitato Nazionale Energia Nucleare,Roma Rep.No.RTI/FI(62),7 (1962).

ASHBY, D.E.T.F. and JEPHCOTT, D.F., Appl. Phys. Letters, 3, 13 (1963).

AXON, K. and REID, G.W., Culham Lab. Internal Report, CLASP Memo No 83 (1968).

BAKER, D.A., HAMMEL, J.E. and RIBE, F.L., Phys. Fluids, 4, 1534 (1961).

BARBER, P.B., PILCHER, M.L., SWIFT, D.A. and TOZER, B.A., Proc. 6th Int. Conf. Ionisation Phenomena in Gases, vol 2, 395 Paris (1963).

BARKER, P.B., SWIFT, D.A. and TOZER, B.A., J. Phys. D.: Appl. Phys., 5, 693 (1972).

BASOV, N.G., BELENOV, E.M., GAVRILINA, L.K., ISAKOV, V.A., MARKIN, E.P., ORAEVSKII, A.N., ROMANENKO, V.I. and FERAPONTOV, N.B., J E T P, Lett. 20, 277 (1974).

BERGSTROM, J., HOLMBERG, S. and LEHNERT, B., Arkiv för Fysik, 25, 49 (1963).

BERNHARDT, A.F., DUERRE, D.E., SIMPSON, J.R. and WOOD, L.L., Appl. Phys. Letts., 25, 617 (1974).

BERNSTEIN, I.B. and RABINOWITZ, I.A., Phys. Fluids, 2, 112 (1959).

BOESCHOTEN, F., Proc. Int. Conf. Uranium Isotope Separation, paper 11, London (1975).

BOHM, D., 'The Characteristics of Electrical Discharges in Magnetic Fields' chapter 3, edited by A. Guthrie and R.K. Wakerling, McGraw-Hill, (1949).

BONNEVIER, B., Arkiv för Fysik, 33, 255 (1966).

BONNEVIER, B., Plasma Phys. 13, 763 (1971).

BOOTH, J., Private communication (1973).

BOYER, K., HAMMEL, J.E., LONGMIRE, C.L., NAGLE, D., RIBE, F.L. and RIESENFELD, W.B., Proc. 2nd Int. Conf. Peaceful Uses of Atomic Energy, 31, 319 Geneva (1958).

BRAGINSKII, S.I., Soviet Phys. J E T P, 6, 358 (1958).

BURCHAM, J., Private communication (1973).

CAIRNS, J.B.S., Inst. of Phys. Conf. Plasma Physics, Bangor, (1974) (Unpublished).

CAIRNS, J.B.S., Proc. Int. Conf. Uranium Isotope Separation, paper 7, London, (1975).

CRAIG, A.D., Private communication (1972).

CHEN, F.F., 'Plasma Diagnostic Techniques', chapter 4, (edited by R.H. Huddlestone and S.L. Leonard), Academic Press, (1965).

DANIELSSON, L., Phys. Fluids, 13, 2288 (1970).

DANIELSSON, L., Astrophys. and Space Sci. 24, 459 (1973).

DEMARIA, A.J., Proc. of the IEEE, 61, 731 (1973).

EDGLEY, P., Private communication (1975).

ENGEL, E. von., STEENBECK, M., 'Elektrioche Gasentladugen 1', Berlin, Springer Verlag (1932).

FAHLESON, U.V., Phys. Fluids, 4 123 (1961).

FORSEN, H.F. and TRIVELPIECE, A.W., Phys. Fluids, 9, 1022 (1966).

GEORGE, D.W. and KANE, E.L., Proc. 2nd Int. Conf. Gas Discharges, 174, London (1972).

GILBODY, H.B. and HASTED, J.B., Proc. Roy. Soc., A238, 334 (1956).

HAAS, F., Private communication (1974).

HALBACH, K. and BAKER, W.R., Phys. Fluids Suppl., 62 (1964).

HARDER, C.R. and FORSEN, H.K.,

HELLER, H. and SIMON, M., Phys. Letters, 50A, 139 (1974).

HELLSTEN, T. and RAGGI, R., Stockholm Report No TRITA-EPP-74-07, Royal Institute of Technology, (1974a).

HELLSTEN, T., Stockholm Report No TRITA-EPP-74-19, Royal Institute of Technology, (1974b).

HILL, M. and MONTAGUE, R.G., Culham Lab. Report No CLM-M62 (1966).

HIMMEL, G. and PIEL, A., J. Phys. D., 6, L108 (1973).

HODGE, C.H. and PRIOR, W.A.J., Culham Lab. Computer Library Information Note No 15/69 (1969).

HOH, F.C., Phys. Fluids, 6, 1184 (1963).

HOLT, E.H. and HASKELL, R.E., 'Foundations of Plasma Dynamics', Macmillan, (1965).

HUDDLESTONE, R.H. and LEONARD, S.L., 'Plasma Diagnostics Techniques', Academic Press, (1965).

IRISAWA, J. and JOHN, P.K., Rev. Sci. Instrum., 44, 1021 (1973).

JAMES, B.W. and SIMPSON, S.W., Phys. Letters, 46A, 347 (1974).

JAMES, B.W., MILLAR, D.D. and SIMPSON, S.W., Proc. Int. Conf. Uranium Isotope Separation, paper 10, London (1975).

JANCEL, R. and KEHAN, Th., 'Electrodynamics of Plasmas', New York, Wiley (1966).

JEFFERIES, D.K., Culham Lab. Report No. CLM-M37 (1964).

JETTER, H., GÜRS, K. and DIBBERT, H.J., Proc. Int. Conf. Uranium Isotope Separation, paper 4, London (1975).

JONES, L.A., J. Appl. Phys., 45, 5206 (1974).

KOGELNIK, H. and LI, T., Appl. Optics, 5, 1550 (1966).

KOLSKY, H., 'Stress Waves in Solids', Oxford, Clarendon Press (1953).

KUNKEL, W.B., BAKER, W.R., BRATENAHL, A. and HALBACH, K., Phys. Fluids, 6, 699 (1963).

LANGMUIR, I. and MOTT-SMITH, H.M., Gen. Electric Rev., 27, 449 (1924).

LEHNERT, B., Nuclear Fusion, 8, 173 (1968).

LEHNERT, B., BERGSTRÖM, J., HOLMBERG, S. and WILNER, B., Physica Scripta, 1, 39 (1970a).

LEHNERT, B., Physica Scripta, 2, 106 (1970b).

LEHNERT, B., Nuclear Fusion, 11, 485 (1971).

LEHNERT, B., Stockholm Report No. TRITA-EPP-72-28, Royal Institute of Technology, (1972).

LEHNERT, B., Physica Scripta, 7, 102 (1973a).

LEHNERT, B., Stockholm Report No. TRITA-EPP-73-01, Royal Institute of Technology, (1973b).

LEHNERT, B., Stockholm Report No. TRITA-EPP-75-13, Royal Institute of Technology, (1975).

LIU, Y.S., Appl. Optics, 13, 2505 (1974).

LONDON, H., 'Separation of Isotopes', chapter 6, Newnes Press (1961).

LONGMIRE, C.L. and ROSENBLUTH, M.N., Phys. Rev., 103, 507 (1956).

MAY, R.M., CRAWFORD, J.D., JAMES, B.W. and WATSON-MUNRO, C.N., Nuclear Fusion, 5, 121 (1965).

McCLURE, J.J., NATHRATH, N., SCHWENN, R., Proc. 10th Int. Conf. Phenomena on Ionised Gases, p.209, Oxford (1971).

McCLURE, J.J. and NATHRATH, N., Proc. 27th Conf. Gaseous Electronics, Houston (1974).

NATHRATH, N., Proc. 11th Int. Conf. Phys. of Ionised Gases, p.245, Prague (1973).

NATHRATH, N., KRESS, H., McCLURE, J., MÜCK, G. and SIMON, M., Proc. Int. Conf. Uranium Isotope Separation, paper 8, London (1975).

NEBENZAHL, I., Proc. Int. Conf. Uranium Isotope Separation, paper 5, London (1975).

NOESKE, H.O., Aerospace Research Labs. Report No. ARL 71-0139 (1971).

NOVAK, B. and PEKOVEK, S., Rev. Sci. Instr., 41 369 (1970).

PAUL, J.W.M., DAUGHNEY, C.C. and HOLMES, L.S., Proc. IX Int. Conf. Phenomenon in Ionized Gases, 650, Bucharest (1969)

POST, R.F., Ann. Rev. Nuc. Sci., 9, 367 (1959).

RASMUSSEN, C.E., BARBIAN, E.P. and KISTERMAKER, J., Plasma Phys., 11, 183 (1969).

RUMSBY, P., Private communication (1973).

SAGALYN, R.C. and SMIDDY, M., J. Geophysical Research, 68, 199 (1963).

SANMARTIN, J.R., Phys. Fluids, 13, 103 (1970).

SCHOTT, L., 'Plasma Diagnostics', chapter 11, edited by W. Lochle-Holtgreven, North-Holland Pub. Co. (1968).

SCHWENN, R., Z. Naturforschg., 25a, 1301 (1970).

SEGAL, S.B. and KOOPMAN, D.W., Phys. Fluids, 16, 1149 (1973).

SHERMAN, J.C., Astrophys. and Space Sci., 24, 487 (1973).

SHKAROFSKY, I.P., BERNSTEIN, I.B. and ROBINSON, B.B., Phys. Fluids, 6, 40 (1963a).

SHKAROFSKY, I.P., Can. J. Phys., 41, 1787 (1963b).

SIMON, A., Phys. Fluids, 6, 382 (1963).

SLEPIAN, J., J. Appl. Aphys., 26, 1283 (1955).

SMITH, L.P., PARKINS, W.E. and FORRESTER, A.T., Phys. Rev., 72, 989 (1947).

SMITH, D., ADAMS, N.G., DEAN, A.G. and CHURCH, M.J., J. Phys. D.: Appl. Phys., 8, 141 (1975).

SNAVELY, B.B., Lawrence Livermore Laboratory Report No. UCRL-76042 (1974).

SPITZER, L., Astrophys. J., 116, 299 (1952).

SPITZER, L., 'Physics of Fully Ionised Gases', 2nd ed., Interscience (1962).

SRNKA, L.J., Ph.D. Thesis, University of Newcastle-upon-Tyne (1973).

SRNKA, L.J., Plasma Phys., 16, 1129 (1974).

STEINHAUS, J.F., BARR, W.L. and OLESON, N.L., Phys. Fluids, 10, 641 (1967).

SWIFT, J.D. and SHWARTZ, M.J.R., 'Electrical Probes for Plasma Diagnostics', Iliffe (1970).

TAIT, J.H. and ALLEN, T.K., Proc. Int. Conf. Uranium Isotope Separation, paper 6, London (1975).

TAYLOR, J.B., Phys. Fluids, 4, 1142 (1961).

THOMPSON, W.B., 'An Introduction to Plasma Physics', Pergamon Press, (1962).

VAREY, R.H., J. Phys. D.: Appl. Phys., 3, 1107 (1970).

WILSON, C., Private communication (1975).